

**Synthesis, Design and Characterization of a Distributed Feedback
Grating Based Non-linear Optical Chemosensor**

by

Aetna W. Wun

B.S. Chemistry

University of California, San Diego, 2000

SUBMITTED TO THE DEPARTMENT OF CHEMISTRY IN PARTIAL
FULFILLMENT OF THE REQUIREMENTS FOR THE DEGREE OF

DOCTOR OF PHILOSOPHY IN CHEMISTRY

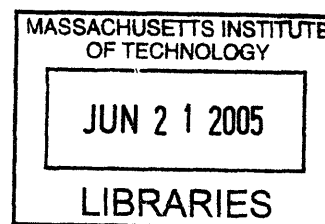
AT THE

MASSACHUSETTS INSTITUTE OF TECHNOLOGY

June 2005

© Massachusetts Institute of Technology, 2005

All Rights Reserved



Signature of Author: _____
Department of Chemistry
May 24, 2005

Certified by: _____
Daniel G. Nocera
W. M. Keck Professor of Energy and Professor of Chemistry
Thesis Supervisor

Accepted by: _____
Robert W. Field
Haslam and Dewey Professor of Chemistry
Chairman, Departmental Committee on Graduate Studies

ARCHIVES

This doctoral thesis has been examined by a Committee of the Department of Chemistry as follows:

1

Stephen J. Lippard
Arthur Amos Noyes Professor of Chemistry and Department of Chemistry Head
Committee Chairman

Daniel G. Nocera
W. M. Keck Professor of Energy and Professor of Chemistry
Thesis Supervisor

Timothy M. Swager
Professor of Chemistry

Synthesis, Design and Characterization of a Distributed Feedback Grating Based Non-linear Optical Chemosensor

by

Aetna W. Wun

*Submitted to the Department of Chemistry on
May 24, 2005*

*in partial fulfillment of the requirements for the
Degree of Doctor of Philosophy in Chemistry.*

ABSTRACT

Current optical chemosensors that operate by a 3R sensing approach – recognize, relay and report – generate a measurable luminescent signal in the presence of targeted analyte. However, the advancement of chemical sensing into the micro- and nanoscale regimes necessitates the development of new signaling transduction strategies. There are just too few sensing active sites on the micro- and nano-patterned structures to permit species detection, resulting in the compromise of device sensitivity and performance.

This thesis work addresses these challenges by adopting a *multidisciplinary* approach in combining chemistry, materials and optical sciences in the development of a chemical and biological sensor. The platform with which we have focused our efforts is the Distributed Feedback (DFB) laser cavity. The waveguide materials synthesized are Si and Ti inorganic matrices that were optimized for optical waveguiding by determining the appropriate film thickness, refractive index and film smoothness. Amplified stimulated emission was achieved for a Rhodamine 6G doped SiO₂/TiO₂ slab waveguide. Imprinting of the DFB architecture onto these thin films was successfully achieved using soft lithography techniques and lasing was observed for these devices (Q-factor ~ 245). We have explored analyte detection capabilities of these DFB structures by attempting to spoil the gain of the cavity, and by using them as simple diffraction gratings for chemical sensing.

Optical sensors are not limited to chemical and biological sensing, and we have applied the 3R approach to understanding the flow and transport properties in microdomains. In the final Chapter, new optical probes for measuring slow flows in microchannels are discussed. This thesis includes a detailed synthetic and photophysical study of *reversible* caged dye tracers with a [Cp*Ru]⁺ metal head group for the Molecular Tagging Velocimetry technique.

Thesis Supervisor: Daniel G. Nocera

Title: W. M. Keck Professor of Energy and Professor of Chemistry

*In loving memory of my Dad,
who always inspired, motivated and challenged me.
And to my Mom for her strength, love and never ending support.*

Acknowledgments.

The five years I have spent at MIT as a graduate student have truly been a growth and learning experience for me. Undoubtedly, this thesis does not fully represent all of my experiences and education, but it can be said that I could not have completed this phase of my life without the love and support of my family and friends. So many thanks...

To my parents • You have always impacted the decisions I made, and I thank you for your support, encouragement to face challenges, and for instilling in me a sense of responsibility and dedication. And I would also like to thank you Cary, for your assistance and advice whenever I needed it most.

To Josh • A best friend is hard to come by – especially someone who, on occasion, knows you better than yourself, and is there for both good times and bad. In fact, there are those rare moments when I am either at my worst or happiest, and I wish that person were there to help or celebrate, and share that time with me. Josh, thank you for your unwavering support and love – I appreciate your creative spirit, curiosity, and I admire your ability to achieve the unthinkable. I do not doubt that our bond will continue to mature and strengthen even as we move miles apart.

To my friends • Erika, Eranthie and Debbie – you have been my support network, stress outlet and the best girlfriends that I could ever ask for. Great memories, great times. I also want to acknowledge those friends, Shana and Sara, who even from afar are always there for me and know exactly what I mean and how I feel during my phone calls of desperation. And Fawn – 14 years and counting – I look forward to our future years together back home.

To the Nocera Group • I have seen and endured many phases of our “large and aggressive” group, but I have been fortunate enough to learn from (and drink with) a great cast of lab mates and scientists. To Alan, Christina, Brad and Niels—thank you for all your help, friendship and advice. Thanks to Al Barney and Scott² for getting me started (synthesis and lasers,

Acknowledgments

respectively) on my first research project. To Bart and Dave (Manke) of the Ultimate Driving Machine – you guys have been great classmates and friends. You both have been instrumental in keeping it real and me sane ... and you will always be remembered as the guys who turned me to baseball. Bart, I wish you all the best with your endeavors into academics and I will see you in California. Dave, I anticipate your not keeping in touch and not responding to e-mails, but I hope that one day you will get a cell phone so we can meet up and grab a beer. J.Crew, Steve and Arthur – continue the “legacy”. Thank you Arthur for your assistance with DFT calculations, and to both Preston and Yinthai for being awesome collaborators.

To Gretchen • Nothing could have been completed without you – you keep this group running smoothly, and I am glad that I will not be here to witness the disaster it will be when you leave.

To Mike • You are a great mentor, and have been a much needed source of advice, support and guidance for the past nine years. I am also thankful for your sabbatical visit here this spring, and will always be inspired by your vision in science and generosity to help others.

And to Dan • You taught me how to be a better scientist and to approach and tackle problems with the tenacity believing that no challenge is insurmountable. Most importantly, you never gave up on me and I will always appreciate your invaluable insights, guidance and giving me the opportunity to figure things out independently. Your remarkable intuition and dynamic presence will be missed...we can have Ladies Lunch anytime.

Table of Contents.

Abstract	3
Acknowledgments	5
Table of Contents	7
List of Figures	11
List of Schemes	14
List of Tables	15

Chapter 1

1.1 Introduction	17
1.1.1 Excited States and Photophysics of Optical Chemosensors	19
1.1.2 Cyclodextrins as Receptors for Optical Chemosensors	23
1.1.3 A Microfluidic Optical Chemosensor	26
1.2 Single Molecule Spectroscopy	28
1.2.1 Single Molecule Spectroscopy Sensing Based on Fluorescence	28
1.2.2 Single Molecule Spectroscopy Sensing Based on Conductance	30
1.3 Scope and Motivation for Thesis Work	33
1.4 References	35

Chapter 2

2.1 Introduction	43
2.1.1 Introduction to Laser Cavities	43
2.1.2 Asymmetric Slab Waveguides	45
2.1.3 Distributed Feedback Structures as Laser Cavities	47
2.1.4 Thin Film Distributed Feedback (DFB) Lasers	49
2.1.5 High Gain Sensing Strategies	51
2.1.6 Parallels to Cavity Ring-down Spectroscopy	53
2.2 Results and Discussion	56
2.2.1 Synthesis of Thin Films	56

Table of Contents

2.2.2	Composition Effects on Film Properties	57
2.2.3	Mesoporous Silica Cladding Layer	62
2.2.4	Optical Waveguiding of the Thin Films	63
2.2.5	Distributed Feedback Grating Fabrication	65
2.2.6	Optical Characterization of DFBs	72
2.2.7	Vita Blue Dye Inclusion	75
2.2.8	Covalent Attachment of Receptor Sites	78
2.3	Conclusions	82
2.4	Experimental	83
2.4.1	General Methods	83
2.4.2	Materials	84
2.4.3	Synthesis of SiO ₂ / TiO ₂ Matrix	84
2.4.4	Preparation of PDMS Stamps	85
2.4.5	Preparation of DFB Samples	85
2.4.6	Characterization Techniques	85
2.4.6.1	Surface Profilometry	85
2.4.6.2	Single Wavelength Ellipsometry	86
2.4.6.3	Spectroscopic Ellipsometry	86
2.4.6.4	Atomic Force Microscopy	86
2.4.6.5	Atomic Force Profilometry	87
2.4.6.6	Scanning Electron Microscopy	87
2.4.7	Synthesis of Mesoporous Silica Layer	87
2.4.8	Optical Measurements	88
2.4.9	Synthesis of Vita Blue Dye	89
2.4.10	Synthesis of Propoxy Coumarin Linkage	90
2.4.11	Synthesis of Urethane Coumarin Linkage	91
2.5	References	92

Table of Contents

Chapter 3

3.1	Diffraction Grating Response	97
3.1.1	Introduction to Diffraction Theory	97
3.1.2	Chemoresponsive Diffraction Measurements	98
3.2	Results and Discussion	102
3.3	Future Directions	106
3.4	Concluding Remarks	108
3.5	Experimental	109
3.5.1	Materials	109
3.5.2	Preparation of PDMS Stamps	109
3.5.3	Preparation of Diffraction Gratings	109
3.5.4	Diffraction Grating Measurements	110
3.6	References	111

Chapter 4

4.1	Introduction	113
4.1.1	Sensing Physical Phenomena	113
4.1.2	Molecular Tagging Velocimetry	116
4.1.3	Limitations of MTV in the Microdomain	117
4.1.4	Reversible Caged Dyes as Tracers for MTV	119
4.2	Results and Discussion	123
4.2.1	Synthesis of Ruthenium Arene Complexes	123
4.2.1.1	[Cp*Ru(NCMe) ₃] ₂ PF ₆ (5)	124
4.2.1.2	[Cp*Ru] ⁺ Laser Dye Complexes	125
4.2.2	Electronic Absorption Spectra of Compounds 6 and 7	130
4.2.3	De-caging Photochemistry of [Cp*Ru(C460)]PF ₆ (6)	132
4.2.4	De-caging Photochemistry of [(Cp*Ru) ₂ (PSA)]PF ₆ (7)	134
4.2.5	Reactivity of the [Cp*Ru ^{III}] ²⁺ Fragment	134

Table of Contents

4.2.6	Electronic Structure Calculations	139
4.2.7	Time Resolved Spectroscopy	142
4.3	Conclusions	144
4.4	Experimental	145
4.4.1	General Synthetic Procedures	145
4.4.2	Physical Methods	145
4.4.3	Photochemical Procedures	145
4.4.4	Spectroscopic Methods	146
4.4.5	Crystallographic Procedures	148
4.4.6	Computational Details	148
4.4.7	Preparation of Propylsulfonated Acridone (PSA)	148
4.4.8	Preparation of [Cp*Ru(NCMe) ₃] ₃ PF ₆ (5)	149
4.4.9	Preparation of [Cp*Ru(C ₆ H ₆)]PF ₆	150
4.4.10	Preparation of [Cp*Ru(C460)]PF ₆ (6)	150
4.4.11	Preparation of [(Cp*Ru) ₂ (PSA)]PF ₆ (7)	151
4.4.12	Preparation of Solutions of [Cp*Ru(OH ₂) ₃](PF ₆) ₂	151
4.5	References	152
Appendix		155
Curriculum Vitae		173

List of Figures

Chapter 1

Figure 1.1. Lock and key in 3R sensing	17
Figure 1.2. Excited state diagram for both intramolecular and intermolecular processes for a molecule M in its excited state M*	20
Figure 1.3. (a) Emission from a singlet excited state	22
(b) Emission in the presence of a heavy atom	22
Figure 1.4. Chemosensing strategy: “turn-off” vs. “turn-on” sensing	23
Figure 1.5. A series of cyclodextrin chemosensors	25
Figure 1.6. A microfluidic optical chemosensor	27
Figure 1.7. Schematic of the PET mechanism for single molecule detection	29
Figure 1.8. Single molecule detection on two nanowire FETs	31
Figure 1.9. Non-linear chemosensing strategy	34

Chapter 2

Figure 2.1. Increasing the number of mirrors in a laser cavity	44
Figure 2.2. Schematic of an asymmetric waveguide	45
Figure 2.3. Schematic of the counter propagating waves along a DFB cavity	47
Figure 2.4. Diagram of a laterally coupled ridge waveguide DFB laser	48
Figure 2.5. Configurations of simple planar waveguides	50
Figure 2.6. High gain sensing strategy with DFBs	52
Figure 2.7. Simplified diagram of a CRDS detection setup	54
Figure 2.8. AFM images of thin films	58
Figure 2.9. Plot of the calculated refractive index as function of wavelength	60
Figure 2.10. Surface profilometry trace of Figure 2.9 sample	60
Figure 2.11. (left) Solution UV-vis and steady state fluorescence spectrum of Rhodamine 6G; (right) ASE of a 2:1 Si / Ti film	64
Figure 2.12. SEM images of photoresist and master gratings	66
Figure 2.13. SEM images of room temperature stamped films	67

List of Figures

Figure 2.14. Atomic force profilometry scan of a room temperature stamped film	68
Figure 2.15. Atomic force profilometry trace (top: contact mode; bottom: tapping mode) of room temperature stamped films	70
Figure 2.16. SEM image of a [Ti] film	71
Figure 2.17. Emission from 2:1 Si(OEt) ₄ / Ti(OEt) ₄ stamped film	72
Figure 2.18. Power dependent lasing emission from a 2:1 Si(OEt) ₄ / Ti(OEt) ₄ stamped film	73
Figure 2.19. Lasing emission observed from a Ti(OBu) ₄ stamped film	74
Figure 2.20. Titration of VB dye monitored by (top) UV-vis and (bottom) emission spectroscopies	77
Figure 2.21. Optical detection setup for a slab waveguide and DFB	89
Chapter 3	
Figure 3.1. Using a DFB to obtain a diffraction grating pattern	98
Figure 3.2. Diagram of detection setup for diffraction gratings	99
Figure 3.3. Monitoring diffracted spot of a DCM - DFB film: control	103
Figure 3.4. Monitoring diffracted spot of a DCM - DFB film (acetonitrile and methanol exposure)	104
Figure 3.5. Monitoring diffracted spot of a DCM - DFB film (chloroform exposure)	105
Figure 3.6. Use of double gratings where one serves as a control channel	106
Figure 3.7. Reichardt's dye absorbance spectra with different solvents	107
Chapter 4	
Figure 4.1. 3R chemosensing and physical sensing	115
Figure 4.2. Photophysics required for design of reversible caged laser dye tracers	119
Figure 4.3. Various metal head groups and laser dye systems that can be implemented for MTV	121
Figure 4.4. Thermal ellipsoid plot of [Cp*Ru(C460)] ⁺ (6-PF ₆)	127

List of Figures

Figure 4.5. Thermal ellipsoid plot of $[(\text{Cp}^*\text{Ru})_2(\text{PSA})]^+$ (7-PF₆)	129
Figure 4.6. (a) UV-vis spectra of free C460 dye and 6	131
(b) UV-vis spectra of free PSA dye and 7	131
Figure 4.7. (a) UV-vis spectra, and (b) emission spectra monitoring the photolysis of 6	133
Figure 4.8. (a) UV-vis spectra, and (b) emission spectra monitoring the photolysis of 7	135
Figure 4.9. (a) UV-vis spectra of $[\text{Cp}^*\text{Ru}(\text{OH}_2)_3]^{2+}$ + PSA (initial and upon heating); (b) UV-vis spectra monitoring photolysis of sample	137
Figure 4.10. (a) Difference absorption spectra for photolysis of $[\text{Cp}^*\text{Ru}(\text{OH}_2)_3]^{2+}$ + PSA with $\lambda_{\text{exc}} = 395$ nm; (b) $\lambda_{\text{exc}} = 435$ nm	138
Figure 4.11. Electronic structure calculation of simplified 6-PF₆	140
Figure 4.12. Electronic structure calculation of simplified 7-PF₆	141
Figure 4.13. (a) Time resolved data for single / double pulse experiments on 7 ; (b) Single pulse measurement of $[\text{Cp}^*\text{Ru}(\text{OH}_2)_3]^{2+}$ + PSA	143
Appendix	
Figure A.1. Negative ion ESI-MS of Vita Blue dye	156
Figure A.2. FTIR spectrum of urethane coumarin linkage	157
Figure A.3. Fully labeled thermal ellipsoid plots for $[\text{Cp}^*\text{Ru}(\text{C460})]^+$ (6-PF₆) and $[(\text{Cp}^*\text{Ru})_2(\text{PSA})]^+$ (7-PF₆)	158

List of Schemes

Chapter 2

Scheme 2.1.	General sol-gel synthesis of SiO ₂ / TiO ₂ matrix	56
Scheme 2.2.	Schematic of ASE for a molecule	63
Scheme 2.3.	Vita Blue dye synthesis	75
Scheme 2.4.	Deprotonated states of Vita Blue	76
Scheme 2.5.	Coupling agents for silylation	79
Scheme 2.6.	Silanization reaction for surface modification	79
Scheme 2.7.	Three methods for dye linkage	80
Scheme 2.8.	Method for biomolecule attachment	81

Chapter 4

Scheme 4.1.	General reaction of the reversible caged dye system	123
Scheme 4.2.	General synthetic scheme for Cp* <i>Ru</i> caged dye complexes	125

List of Tables

Chapter 2

Table 2.1. Profilometry and Single Wavelength Ellipsometry Data for C152 samples	61
Table 2.2. DFB gratings specific for different waveguide media	65
Table 2.3. Profilometry and spectroscopic ellipsometry data for Si(OEt) ₄ / Ti(OBu) ₄ films	69

Chapter 4

Table 4.1. Selected bond lengths for [Cp*Ru(C460)] ⁺ (6-PF₆)	127
Table 4.2. Selected bond lengths for [(Cp*Ru) ₂ (PSA)] ⁺ (7-PF₆)	129

Appendix

Table A.1. Crystal data and structure refinement parameters for [Cp*Ru(C460)] ⁺ (6-PF₆) and [(Cp*Ru) ₂ (PSA)] ⁺ (7-PF₆)	158
Table A.2. Atomic coordinates and equivalent isotropic displacement parameters for [Cp*Ru(C460)] ⁺ (6-PF₆)	159
Table A.3. Bond lengths and angles for [Cp*Ru(C460)] ⁺ (6-PF₆)	160
Table A.4. Anisotropic displacement parameters for [Cp*Ru(C460)] ⁺ (6-PF₆)	162
Table A.5. Hydrogen coordinates and isotropic displacement parameters for [Cp*Ru(C460)] ⁺ (6-PF₆)	163
Table A.6. Atomic coordinates and equivalent isotropic displacement parameters for [(Cp*Ru) ₂ (PSA)] ⁺ (7-PF₆)	164
Table A.7. Bond lengths and angles for [(Cp*Ru) ₂ (PSA)] ⁺ (7-PF₆)	166
Table A.8. Anisotropic displacement parameters for [(Cp*Ru) ₂ (PSA)] ⁺ (7-PF₆)	168
Table A.9. Hydrogen coordinates and isotropic displacement parameters for [(Cp*Ru) ₂ (PSA)] ⁺ (7-PF₆)	170

Chapter 1. 3R Sensing Strategy: Approach, Advantages and Limitations

1.1 Introduction

Chemosensors are molecular-scale structures that recognize and signal the presence of analytes.¹⁻¹⁰ Analyte detection is registered as a change in the structure's physical, optical or magnetic properties. Many chemosensors operate by a "3R" sensing mechanism of recognize, relay and report. The 3R method is depicted in Figure 1.1. A non-covalent molecular recognition event is communicated by physical or chemical means to the reporter site, and produces a measurable signal to indicate the presence of analyte. A rapid equilibrium between the analyte and the reporter site affords the chemosensor a real time response, which is dependent on the concentration of analyte. For any chemosensing application, the sensitivity and selectivity are crucial and evaluated for its effectiveness. Selectivity is derived from the "lock and key" association of the analyte to the reporter site, whereas the strength of this interaction (K_a) determines the overall sensitivity and selectivity. Sensitivity is further enhanced by the efficiency of the relay mechanism to communicate the binding event, and also by the competence of the reporter site in conveying that event.

Owing to their diverse shapes and topologies, supramolecules have been extensively surveyed as receptor constructs in chemosensor design. Functional requirements in the "lock and

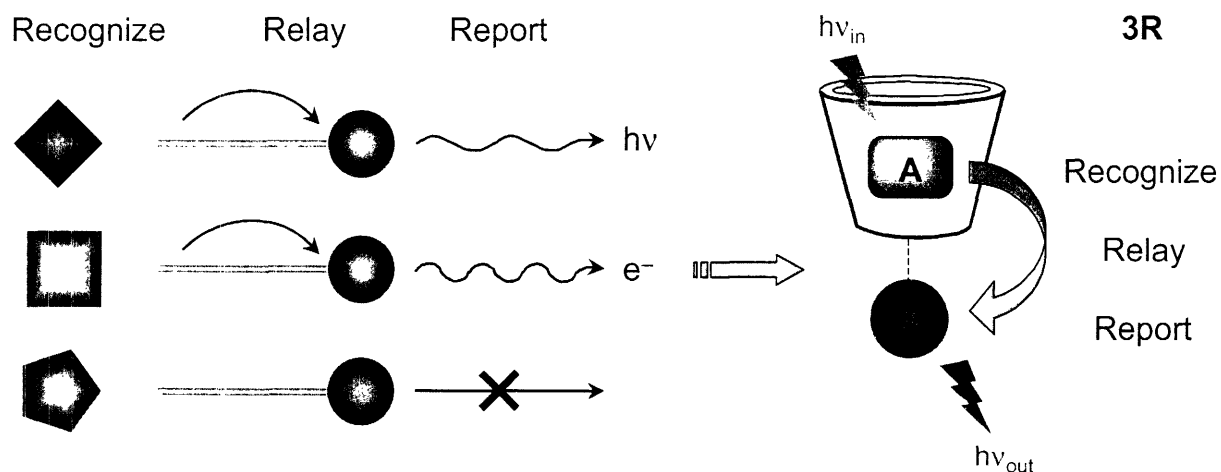


Figure 1.1. (left) Lock and key in 3R sensing. The presence of docked analyte is reported via a relay mechanism to produce an optical or electrical signal from the reporter site. (right) Our design of a supramolecular optical chemosensor that operates under the 3R scheme. (A = analyte)

Chapter 1

key” mechanism described above can be fulfilled by supramolecules that form balls, bowls, boxes, bracelets, buckets, chains, clamps, cubes, ladders, lariats, pagodas, saddles, starbursts and tweezers.¹¹⁻¹³ They can be 10–100 nm in dimension and afford chemists with the non-covalent receptor site for analyte to bind, and a scaffold upon which a reporter can be attached.^{1,3,4,11,14,15} Signaling may be accomplished by either electrical or optical methods, however the latter has come to the forefront owing to its sensitivity and ease of implementation.^{16,17} Optical signaling from luminescence is preferred, which is usually initiated by a conformational change, energy transfer, electron transfer, or a combination of these processes. This relay mechanism provides the means by which the chemosensor communicates the non-covalent recognition of analyte, under dynamic equilibrium with the supramolecular receptor site, to the reporter.

Previous work in our group has exploited the functional shape of the supramolecular bucket in chemosensor design.⁷ The buckets maintain a cylindrical cavity with structurally and chemically well-defined upper and lower rims. One can imagine the size and shape of a bucket being ideal as a docking site for many an analyte. However, without further adornment, the supramolecular bucket is not a capable chemosensor since it cannot signal on its own. In the simplest of designs, the analyte generates a signal upon association to the bucket, whereas in more intricate designs, functionality at the rim of the bucket offers sites to attach a discrete reporter site. In this Chapter, the concept of 3R sensing will be developed with supramolecular buckets (depicted in Figure 1.1), highlighting the progression of molecular chemosensors to microfluidic devices. It will conclude with the current limitations and challenges as we attempt to advance chemical and biological sensing into even smaller length scales.

1.1.1 Excited States and Photophysics of Optical Chemosensors

Chemosensors that operate by the emission or quenching of light have increasingly been exploited in chemical and biological sensing applications. The light-emitting signal is superior for chemosensor design because it can:

- report on nanometer length-scales with nanosecond time responses.¹⁸⁻²⁰
- permit analytes and their influences to be monitored continuously in real time and *in situ*.²¹⁻²⁴
- possess an inherently large bandwidth (and hence information capacity).
- feature intrinsic selectivity owing to flexible choices of wavelength and polarization.
- achieve sensitivity down to the single molecule limit.²⁵⁻³⁷
- be married to a variety of imaging technologies, including optical fibers and waveguides.

These latter two issues have been especially prominent driving forces behind the emergence of optical sensing schemes over the last two decades.^{18,38-42} This section will elaborate on the significant advantages (and challenges) of luminescence-based sensing, and the manipulation of excited state chemistry involved in the field of chemosensing. To incorporate “3R” into sensing schemes effectively, especially the relay mechanism, one must be well versed in the understanding of how molecular photophysical properties govern luminescence events. In this manner, novel and *improved* signaling transduction mechanisms can be incorporated with chemosensor active sites and their detection schemes.

Photophysics of excited states involve numerous pathways for a molecule once it is brought from its ground state to one of higher energy. As shown in Figure 1.2, a molecule residing in an electronic excited state (M^*) can decay back to the ground level (M) via numerous intramolecular processes. Competing thermal relaxation and photon emission pathways are described by their nonradiative (k_{nr}) and radiative (k_r) rate constants, respectively.

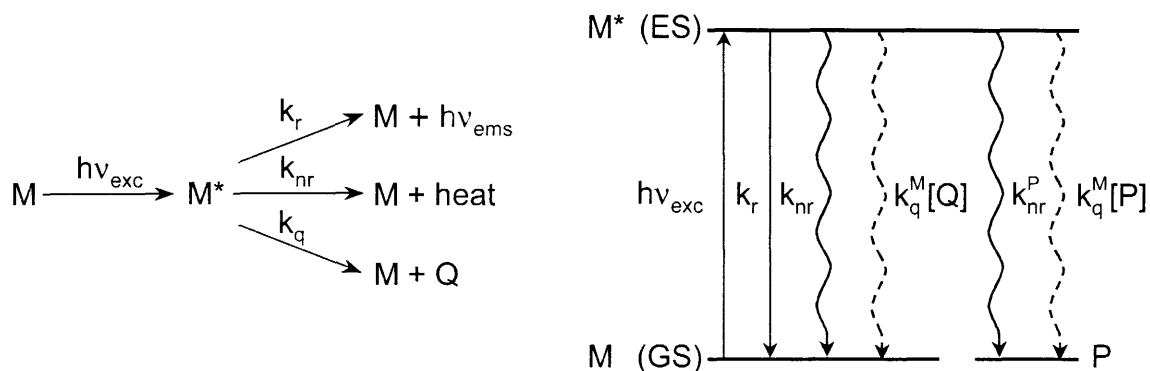


Figure 1.2. Excited state (ES) diagram for both intramolecular (black lines) and intermolecular (black + dashed lines) processes for a molecule M in its excited state M^* , where k_r and k_{nr} are the radiative and nonradiative rate constants, respectively. Superscript M delineates those molecules that return to the ground state (GS) without chemical change, whereas P indicates the formation of a distinct product. Intermolecular rate constants depend on the concentration of quencher molecule (Q).

The radiative rate constant, k_r , is an intrinsic property of the molecule and represents the probability that the molecule will emit a photon at a certain frequency (ν).^{43–45} As seen in eq. (1.1), k_r depends on the emission energy (E_{em}) and the transition dipole moment (μ) of the molecule.

$$k_r = \frac{4E_{em}^3}{3\hbar^2} \left| \langle \Psi_{gs} | \mu | \Psi_{es} \rangle \right|^2 \quad (1.1)$$

In this equation, the square of the transition dipole moment represents the transition probability between the electronic ground state (Ψ_{gs}) and excited state (Ψ_{es}), and can be experimentally measured as the absorption cross-section or extinction coefficient (ϵ) of a molecule. Thus, k_r increases with larger E_{em} and ϵ .

The nonradiative rate, k_{nr} , describes all intramolecular deactivation pathways that do not lead to the emission of a photon of light. The electronic energy of the excited state decays to the high-energy vibrations of the ground state molecule.^{46–48} These vibrational pathways to the equilibrated ground state molecule (M), or in the case of a photochemical process that forms product (P), result in the nonradiative release of heat. The competitive interplay of k_r and k_{nr} directly affect the fundamental *intramolecular* photophysics of M – the photoefficiency of the

Chapter 1

molecule once it is excited by an incident photon.^{49,50} The resulting luminescence intensity (I_o) can be described by the following equation,^{44,45,49}

$$I_o \approx \phi_{em} = \frac{k_r}{k_r + k_{nr}} = k_r \tau_o \quad (1.2)$$

where the intensity is proportional to the quantum yield of emission (ϕ_{em}) and is directly related to the emission lifetime (τ_o). The natural lifetime of an electronic excited state can be equated as,

$$\tau_o = \frac{1}{k_r + k_{nr}} \quad (1.3)$$

In examining eq. (1.2), when $k_{nr} \gg k_r$, the nonradiative relaxation processes dominate and the molecule remains dark upon excitation. While this represents a large percentage of what molecules experience, the molecule can luminesce when the thermal decay is inefficient enough so that $k_r \gg k_{nr}$. This represents one of the inherent challenges in the design of efficient optical chemosensors – manipulating the excited state properties of the molecule so that the radiative processes overtake the competing nonradiative vibrational relaxation channels.

Another crucial element that cannot be overlooked is the presence of quencher molecule (Q) that can effectively modify the photophysical pathways of molecule M in Figure 1.2. The luminescence intensity (I) and lifetime (τ) are related to each other in bimolecular processes as given by,⁵¹

$$I \approx \phi_{em} = \frac{k_r}{k_r + k_{nr} + k_q[Q]} = k_r \tau \quad (1.4)$$

where k_q is the quenching rate constant and $[Q]$ is the concentration of quencher. The addition of $k_q[Q]$ in the denominator is accompanied by the modified lifetime,

$$\tau = \frac{1}{k_r + k_{nr} + k_q[Q]} \quad (1.5)$$

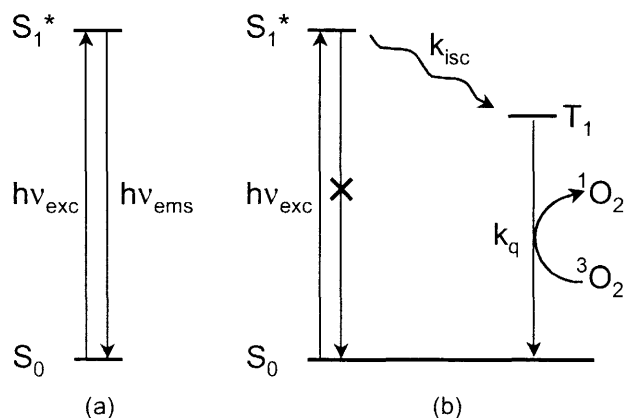


Figure 1.3. (a) Emission from singlet excited state when relaxing to the ground state. (b) With the presence of a heavy atom, like O_2 , the forbidden 3T state is accessible now by intersystem crossing (k_{isc}).

and it is apparent that a weak luminescence and shortened lifetime results from the bimolecular reaction with Q. Both the luminescence intensity and lifetime, under quenching conditions, is quantified by the Stern-Volmer relation,⁵¹

$$\frac{I_0}{I} = \frac{\tau_0}{\tau} = 1 + \tau_0 k_q [Q] \quad (1.6)$$

where I and τ are the luminescence intensity and lifetime in the presence of Q and the subscript indicates those values in the absence of Q.

Equations (1.2–1.6) indicate the ability of the molecule emission to be turned off and on by changes in the rate constants k_r , k_{nr} and k_q . The perturbation of these molecules by the presence of quencher molecule Q can result in the shift in the intensity or energy of the luminescence, thus signaling the presence of an intervening entity. One can conceivably design a simple chemosensing scheme where the analyte (A) targeted for detection is the quencher. Since excited states are highly reactive, the presence of $A = Q$ will ultimately lead to deactivation along the nonradiative pathway described by $k_{nr/q}^{M/P}[Q/P]$ in Figure 1.2. However, the quenching-based chemosensing systems are not very discriminating because of the electronic excited states' high reactivity, and therefore the presence of any interferent will be disabling. A

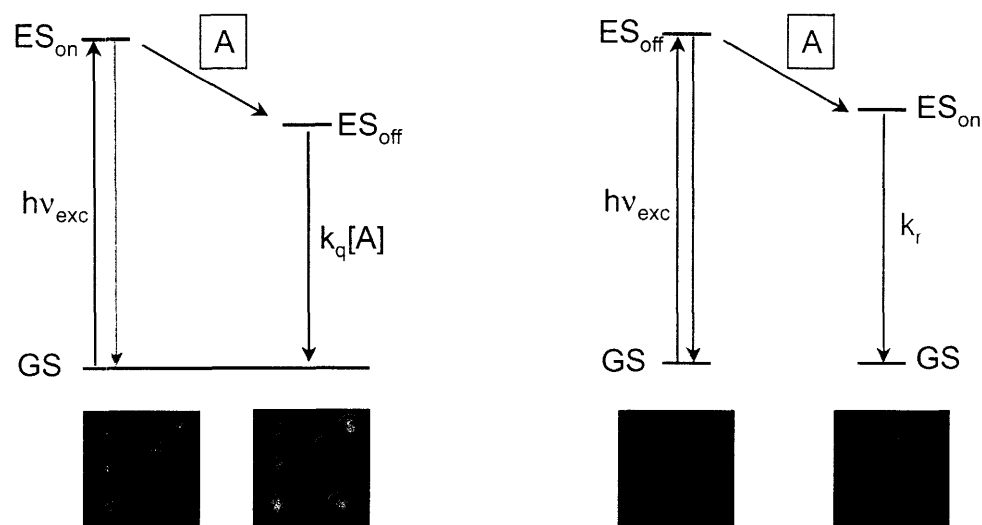


Figure 1.4. (left) Chemosensing strategy where the analyte acts as a quencher, turning off the reporter emission. This is difficult to detect against a bright background. (right) “3R” strategy where the presence of analyte triggers the fluorescence of the dark molecule.

prominent quencher for long-lived excited states is molecular oxygen, with its energetically accessible singlet excited state and its ubiquitous presence in the environment.^{49,52} This heavy atom effect is depicted in Figure 1.3, where the fluorescent molecule, in its singlet excited state and in the presence of the O₂, can access its triplet state and the luminescence is subsequently quenched. Detection by quenching will be difficult because the decrease in luminescence must be measured against a bright background. This quenching strategy is shown on the left side of Figure 1.4. The reverse design can be achieved when the presence and recognition of analyte causes an effective increase in k_r , a decrease in k_{nr} , or a decrease in k_q . In all of these cases, the value of ϕ_{em} will be approaching unity, and the increase in luminescence can be detected against a dark background, as shown on the right side of Figure 1.4.

1.1.2 Cyclodextrins as Receptors for Optical Chemosensors

Previous work in the group involved using a cyclodextrin (CD) as the receptor site in the 3R chemosensor design.⁷ Both calixarenes and cyclodextrins are viable options due to their funnel shaped cavity that can be readily functionalized to attach reporter sites. The host-guest system can be optimized by simply fitting the size of the receptor opening to the targeted analyte.

Chapter 1

Furthermore, the entrance and exit of the analyte can be manipulated by modifying the physical properties rims of the buckets.

Cyclodextrins are chiral, cyclic oligosaccharides composed of six, seven or eight D-glucose molecules (termed α , β , γ -CD, respectively), which catenate via α -(1,4) linkages to produce the bucket-shaped cylindrical cavity of increasing diameters.^{53–55} At both the primary (bottom) and secondary (top) rims are the sugar hydroxyl functional groups that impart solubility in aqueous solutions. Additionally, the hydrocarbon rings of the D-glucose subunits define a hydrophobic interior suitable for binding guests. With these contrasting characteristics, the cyclodextrin buckets have the ability to dissolve in water and to also take-up aliphatic and aromatic compounds including various polar compounds such as functionalized aromatics, amines and alcohols. These inclusion complexes have been reviewed extensively.^{56–58} Binding selectivity (and therefore selectivity in chemosensor function) at the first level of discrimination can be achieved with the CD cavity size. Specifically, β -CD will bind BTEXs (benzene, toluene, ethylbenzene, xylene) but not large polyaromatics such as anthracenes or pyrene, which show an affinity for γ -CD. Cyclodextrins were then exploited for the detection of polyaromatic hydrocarbons (PAHs).

The hydroxyl functional groups at the rims not only provide water solubility, but they also allow chemical modification of the bucket to add attachment sites. Since the buckets themselves cannot signal the detection of analyte, a reporter must be appended to these receptors in order to assemble an optical chemosensor. The primary rim's hydroxyl group provides an accessible one-point modification position at the bottom of the CD cup. Rigid spacer groups were used to connect opposing locations on the bottom rim and a series of members of this CD design strategy were created, as shown in Figure 1.5. The reporter site, a $\text{Ln}^{3+} = \text{Eu}^{3+}$ or Tb^{3+} ion, was encrypted into these straps (reasons for picking these metal ions will be discussed below). Initially an aza crown macrocycle (1,4,10,13-tetraoxa-7,16-diazacyclooctadecane) strap was attached to the CD. In construct **1**, the aza ligand is only attached at one site, causing the strap

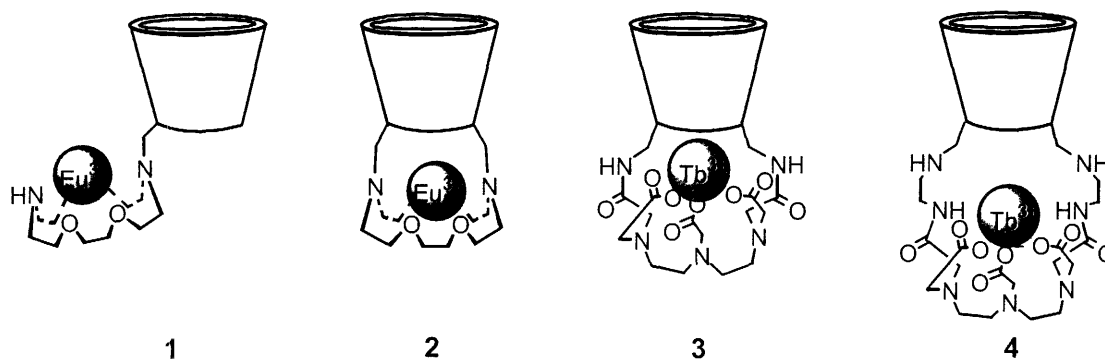


Figure 1.5. A series of chemosensors where the cyclodextrin (CD) is the receptor site and the metal ions Eu^{3+} and Tb^{3+} are the reporter sites. The neutral strap used in **1** and **2** was upgraded to a trianionic ligand in **3** and **4**.

with the Eu^{3+} ion to swing away from the bottom of the cup. The long distance from the reporter site to the bucket was then shortened in **2** where both ends of the aza crown are attached to the CD rim. However, efficient signaling is obviated by the presence of the $3+$ cationic charge at the bottom of the CD. The hydrophilicity attendant to the $3+$ charge undermines association of PAHs to the CD bucket thereby limiting the overall optical response from the chemosensor.⁵⁹ The problem is resolved by construct **3**. With the $3+$ charge of the ion reporter site neutralized by the $3-$ charge of the diethylenetriaminepentaacetic acid (DTPA) strap, aromatics enter the CD bucket of **3** with high association constants. Detailed mechanistic studies establish the signal transduction in **3** to proceed via an absorption-energy transfer-emission (AETE) mechanism. Lanthanide ions are weakly emitting upon direct excitation, due to the spin-forbidden $4f \rightarrow 5d$ transition. However, when aromatic hydrocarbons are present and in close proximity to the Tb^{3+} ion of **3**, absorption of excitation energy by the analyte to its $^1\pi\pi^*$ state is followed by the intersystem crossing to the triplet state of the aromatic. Subsequent energy transfer to the nearby emissive $^5\text{D}_4$ state of Tb^{3+} results in the bright green luminescence of the metal ion.⁶⁰ Förster energy transfer was ruled out as the relay mechanism because of negligible spectral overlap between the absorption and emission profiles of the aromatic and the Tb^{3+} ion respectively. The construction of **4** provided a means to systematically study the distance dependence of the metal ion from the CD bucket (and the analyte), and Dexter energy transfer was confirmed as the relay

mechanism. Analysis of time-resolved energy transfer kinetics data predicts the donor-acceptor distance in **4** to increase by ~ 2 Å as compared to **3**, which is in agreement with results from energy minimized molecular modeling calculations.⁶¹

The above work presents the application of 3R to the design of an optical chemosensor for the detection of environmental contaminants such as PAHs. Our interest in PAH detection was motivated by a problem confronting the U. S. Air Force. Monocyclic BTEXs and bicyclic (naphthalene and biphenyl) aromatic hydrocarbons compose jet fuels such as JP4. Leakage of such fuels into the ground water supplies near Air Force bases and storage facilities can therefore be assessed by monitoring PAH content. Before the development of these chemosensors, detection of these aromatics was accomplished by direct excitation and measurement of the blue fluorescence. This was problematic, however, because the laser induced fluorescence of the aromatics must be deconvoluted from similar blue emission observed from other organic interferences. The 3R scheme outlined above allows for us to choose the proper constituents that meet the sensor design criteria for achieving a unique optical signal distinguishable from aromatic fluorescence. In achieving these goals, the performance capabilities of these sensors must be improved in order to maximize their sensitivity and selectivity.

1.1.3 A Microfluidic Optical Chemosensor

With the development of a successful “turn on” optical chemosensor such as **3**, the performance of the system can be immensely improved upon by integrating it with new technologies. Such progressive sensors are needed for applications including monitoring chemical levels in biological systems and environmental testing for the early detection of hazardous chemicals. The challenge of forthcoming research will be to design portable, cost-effective and reliable miniature chemical sensing devices capable of the same detection specificity and sensitivity accomplished at the molecular level. Microfluidic platforms have emerged as a valuable technology for chemical and biological sensing.⁶² The miniaturization offered by microfluidic devices allows for the analysis of fluid samples to be performed on a

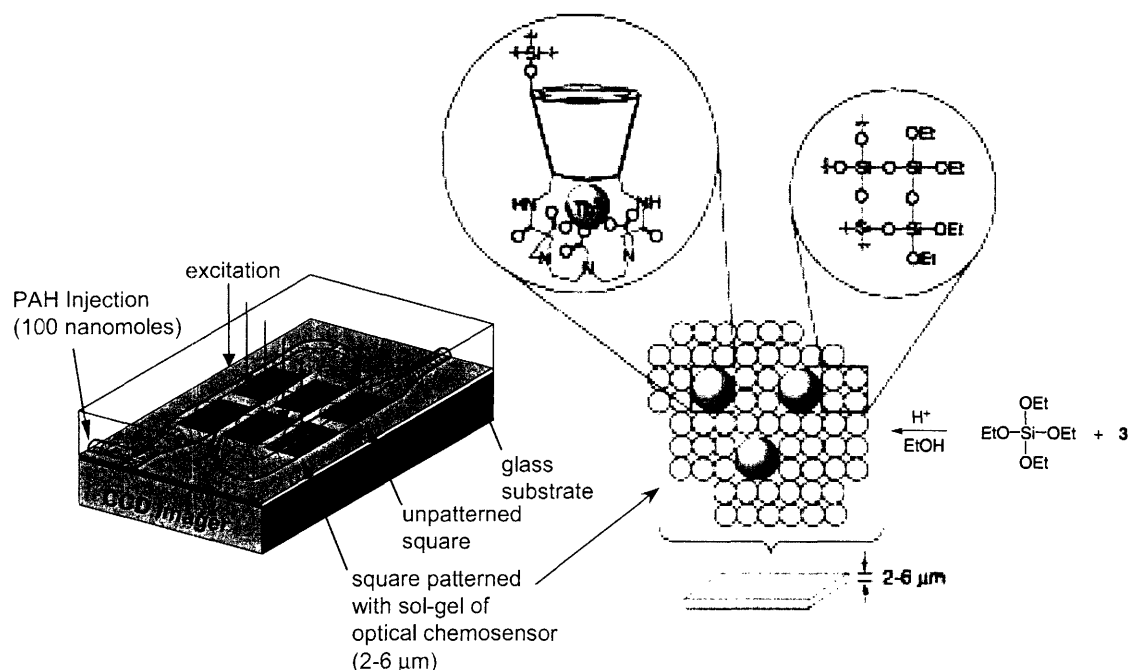


Figure 1.6. A μF optical chemosensor where the active sites are composed of **3** embedded in sol-gel films and patterned onto the serpentine channels. Blue squares are unpatterned and green squares contain the supramolecular chemosensor.

chip, leading to advantages such as reduced sample volume, increased reaction speed, and the possibility of massive parallelism.⁶²⁻⁶⁴ The added advantages compelled the integration of the 3R optical chemosensor **3** into one of these microfluidic devices.

As shown in Figure 1.6, chemosensor **3** was incorporated into the serpentine channels of a microfluidic device by photo-lithographically patterning sensor-encapsulated thin films onto the substrate surface.⁶⁵ The device exhibits excellent optical response to PAHs; importantly, time-resolved kinetics measurements on the sol-gel thin films established that the same 3R mechanism observed in solution prevails in the film. A 45-fold enhancement of the Tb^{3+} luminescence intensity was triggered when a $50 \mu\text{M}$ solution of biphenyl contacts the patterned microstructure. The Tb^{3+} luminescence enhancement proved to be concentration-dependent, increasing monotonically with the concentration of biphenyl. A slow response time (\sim minutes), owing to the micron thickness of the films, was a drawback of the device. Response times may be increased by decreasing the thickness of the pads, but signal was eventually lost for PAH concentrations $< 100 \text{ nM}$.

1.2 Single Molecule Spectroscopy

Paralleling the development of chemosensors, the detection of molecules in the nanodomain has become routine owing to advances in optical spectroscopy and microscopy.⁶⁶⁻⁷² In the past decade, a variety of optical experiments has been designed for single molecule detection in all types of environments, including solids, surfaces and liquids. Moerner and co-workers used a doubly modulated absorption method to obtain the first optical detection of a single molecule in a solid at low temperature.⁷³ Betzig and Chichester obtained the first room-temperature images of single molecules immobilized on a surface with a scanning near-field optical microscope;⁷⁴ this research opened new potential avenues for single molecule spectroscopy. A large scope of applications in biological imaging and analyte detection has subsequently been developed from the advent of confocal microscopy and SMS.⁷⁵⁻⁸¹ Not only is it possible to detect and identify freely diffusing and immobilized molecules, but recent advances include spectroscopic measurements and the ability to monitor dynamic processes of single molecules as well.

1.2.1 Single Molecule Spectroscopy Sensing Based on Fluorescence

Of the potential SMS sensing methods, fluorescence-based SMS has shown the greatest promise for detection of analytes under ambient conditions. Single molecule spectroscopy (SMS) has the ability to detect and monitor systems down to the sensitivity level of $\sim 1.66 \times 10^{-24}$ moles. Notwithstanding, the development of single molecule detection for routine sensing in the condensed phase has lagged because the surrounding matrix or solvent causes a large background emission, which can overshadow the single molecule signal unless the illuminated area is severely reduced. The number of photons that are emitted from a single molecule can be increased by integrating signal for repetitive excitation and emission. However, the overall response is limited by the photostability of the (organic) chromophore (e.g., anthracene or coumarin) at room temperature or by spectral jumps at low temperature.⁸² Along with the photostability, the fundamental photophysics of the fluorophores (absorption cross-section,

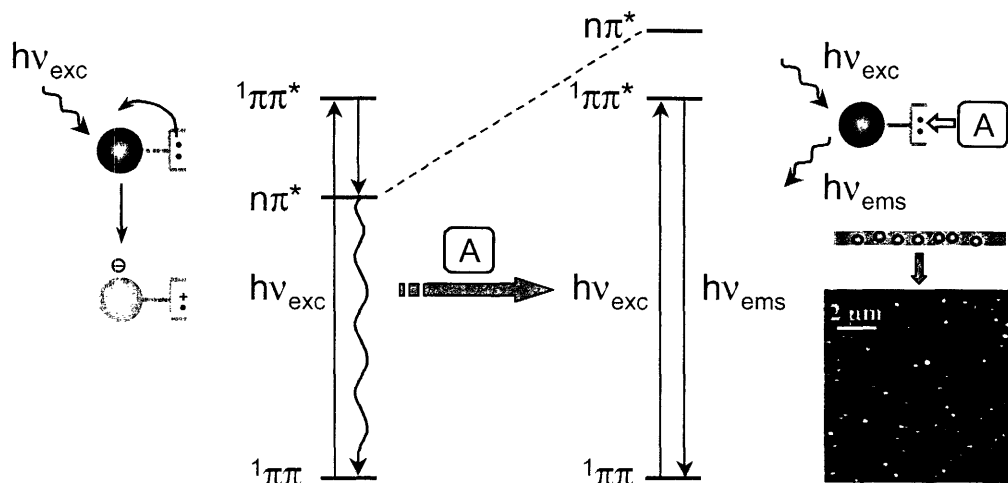


Figure 1.7. Schematic of the PET mechanism where the lone pair at the receptor renders the chromophore non-emissive. Upon binding of analyte, the orbital of the electron pair moves to higher energy, allowing access to the emissive excited state. Such molecules are spincoated onto a glass substrate, and a fluorescence scanning confocal image is shown (from Ref. 83).

fluorescence, triplet quantum yield) presents challenges to SMS sensing. The high excitation intensities can result in population of non-emissive states, which are accessed by the absorption of a second photon. This is especially prevalent with excitation in the UV region, where additional photobleaching pathways exist by the formation of dye radicals and solvated electrons.⁸²

Other methods for using single molecule probes as sensors have been examined.^{70,83} Prevalent among these new approaches is the use of photoinduced intramolecular electron transfer (PET) as a signal transduction strategy.⁸⁴ In PET, a nonbonding electron pair efficiently quenches the excited state of the chromophore, as shown in Figure 1.7. Reactions of this electron pair with protons, metals, organic electrophiles, or surfaces lower its orbital energy below the highest occupied molecular orbital (HOMO) of the chromophore, turning off PET and rendering the chromophore emissive. Fluorescence scanning confocal images of these fluorescent PET probes on various substrates, such as the one in Figure 1.7, demonstrate detection of single binding events. This classical method of transducing a metal-binding event into an optical signal relies on metal-binding-induced alterations of the redox potential of a receptor molecule

covalently attached to a fluorophore. Further improvement of this system and other biosensors will involve combining selectivity with new single molecule sensitive techniques such as polarization or spectrally resolved fluorescence lifetime spectroscopy. This will facilitate the specific detection of analyte in sub-picomolar concentrations with concurrent temporal resolution of the molecular binding dynamics.

1.2.2 Single Molecule Spectroscopy Sensing Based on Conductance

Optical information on nanometer length scales may be obtained by combining information from single molecule optical probes with physical characterization techniques based on mechanical or electrical measurements. Most popular of these methods rely on conductivity or piezoelectric properties of a nanodevice,⁸⁵⁻⁹⁰ which is sensitive to the nature and concentration of adsorbed species at the surface of the semiconductor oxide. Sensing at the single molecule limit has primarily been attempted by using single-walled carbon nanotubes (SWNTs)^{91,92} and semiconductor oxide “quasi-one dimensional” nanostructures, like nanowires and nanobelts for signal transduction.⁹³⁻⁹⁶ One-dimensional nanowires avoid the reduction in conductance charges caused by lateral current shunting, which exists for two-dimensional field effect transistors (FETs), so that single molecule detection is possible.

Biomolecule adsorption onto nanowire FETs can lead to considerable changes in the electrical conductance of such devices, as depicted in Figure 1.8. This phenomenon can be exploited for the development of miniaturized, label-free nanoprobess. Initial work with SWNTs indicated a large conductance change in the presence of ammonia and NO₂,^{97,98} and the demonstration of the nanotubes’ gas-phase sensitivity fueled current research with small biomolecule and protein detection.^{89,92} Lieber and co-workers reported electrical detection of single viruses, where they attempt to reach selective, single particle (stochastic) level sensing.⁸⁶ Stochastic sensing^{99,100} offers fundamental advantages in that the selective detection is not limited by the binding affinity as in other equilibrium measurements, and the single particle sensitivity allows simple charge-based detection mechanisms.

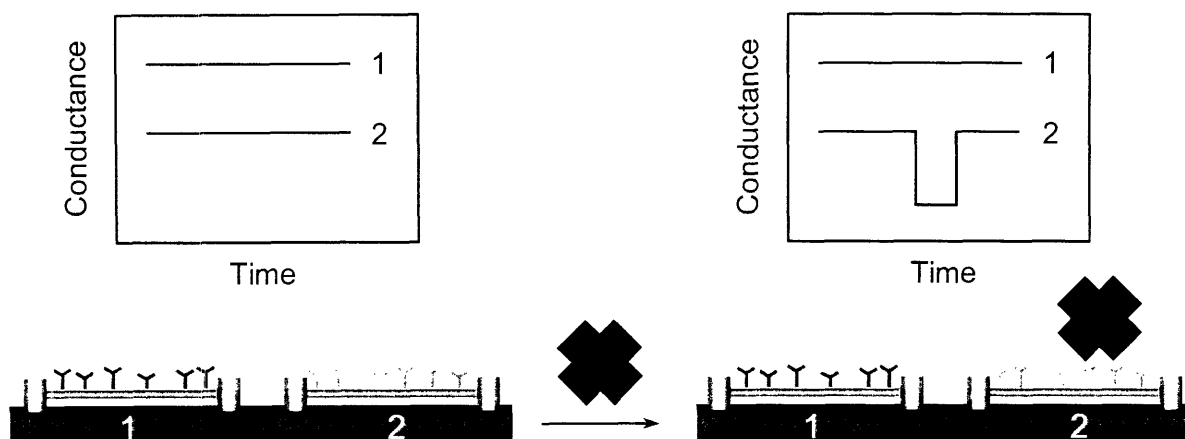


Figure 1.8. Schematic of single molecule detection on two nanowire FETs, where 1 and 2 are modified with different receptors. Specific binding of the biomolecule to the receptors on nanowire 2 induces a conductance change (top). Nanowire 1 serves as a control channel.

The future of nanotube biosensors will require highly miniaturized arrays of SWNTs that can be functionalized and monitored in multiplex. However, some fundamental challenges remain, and a clear understanding of the effects of protein adsorption on the electrical conductance of the FETs is necessary. Two possible proposals had been suggested: (1) surface protein charges exert gating effects or charge transfer to SWNTs,⁹⁰ and (2) protein adsorption affects the dielectric constant of the electrical double layer in aqueous solution thereby changing the gate efficiency of the electrolyte.^{92,101}

Despite these tremendous advances in SMS, Dai and co-workers' recent measurements of SWNT arrays connected in parallel with Pd electrodes have been troubling. They show that much of the conductance changes upon protein binding to the FET devices instead originate from the Pd–nanotube contact region.¹⁰² It was concluded that the major contribution was not the charge injection or field effects of protein adsorption; rather, the modulation of the metal work function at the contact region dominates the conductance change. In order to quantify these contact effects, new devices consisting of an individual SWNT, instead of an ensemble mixture of nanotubes, must be fabricated. Next generation carbon nanotube FETs for biosensing will

Chapter 1

require the elucidation and separation of the complex relationship between SWNTs and metal contacts and their respective interaction with biomolecules.

While these FET devices demonstrated the power of nanoengineering materials into biosensors, the arduous fabrication of these arrays is limited by low throughput and limited controllability. Manipulating individual nanotubes or wires onto pre-patterned electrodes by an AFM,¹⁰³ random dispersion of suspended SWNTs onto electrodes,^{104,105} and lithographically patterning nucleation sites onto electrodes are examples of techniques that generate potential individual devices and not reproducible arrays.^{106,107} More importantly, the biomodification of the surfaces of SWNTs and nanowires are performed post-assembly, precluding the ability to individually address each nanostructured sensing element with the desired receptor. Polypyrrole polymers have recently been implemented into FETs and require only a one-step protocol for synthesis, modification and contact positioning.¹⁰⁸ Although the nanomolar sensitivity of these polymer-based wires is below that of the SWNT and semiconductor devices, the issues with the “bottom-up” fabrication techniques are addressed.

In order to increase the selectivity, number of sensing elements, and detection limits (to single molecule sensitivity) of the sensor, the actual sensitivity and specificity of the sensing element must be amplified with the decrease in the active area and increase in proximity of neighboring components. Most sensing studies with the nanostructures described above are carried out in idealized environments, whereas in ambient conditions, the surfaces or its junctions can adsorb reactive species capable of altering its device performance. The performance of the metal oxide nanowires is extremely dependent on the fabrication, storage and operation of the FETs. Even the most pristine sensing elements have memory or hysteresis effects in the current measurements, and the origin of the current instabilities observed with oxide nanowires are: (1) the aforementioned contacts effects, (2) adsorbed contaminants, and (3) impurities in or on the support layer (often SiO₂) in the proximity of the nanostructure.⁸⁸ For carbon nanotubes, Schottky barriers formed at the contact–tube interface dominated the

conductance changes. Research of oxide nanowires and carbon nanotubes as biosensors is relatively new, and the goal of replacing large, macroscopic sensors with miniaturized nanoscale devices requires overcoming the inherent challenges described above.

1.3 Scope and Motivation for Thesis Work

The conductance instabilities arising from contacts effects, adsorbed contaminants and the presence of support oxides and its impurities^{88,109–111} present significant challenges to implementing nanodevices of the foregoing section for routine sensing applications. Therefore, we have sought to develop methods to enable sensing on small length scales by combining the 3R chemosensing strategy of Section 1.1 with optical nanoscience. The payoff of such an approach is the realization of widely distributed sensing networks that are inexpensive, easy to implement and not encumbered by the intricacies and complications posed by single molecule detection schemes.

The incorporation of optical chemosensor **3** into the microfluidic device of Figure 1.6 made apparent the tradeoff between signal intensity and response time. As the number of receptor sites diminishes with decreasing thickness, device sensitivity and performance is compromised because *single molecule detection – single photon generation* yields signals that are too weak to be detected. The implementation of 3R sensing with nanoscience will require new signaling transduction strategies because there are simply too few sensing active sites on the micro- and nano-patterned structures to permit detection of species.

This thesis work addresses these challenges by exploring strategies to increase chemosensor response by replacing the linear, single photon response of present chemosensors with extremely nonlinear optical responses. To achieve this objective, a multi-pronged approach is devised that combines photochemistry, materials synthesis and optical science. This strategy is presented in Figure 1.9 in which the light emitting molecular centers of conventional optical chemosensors are substituted with a mesoscopic optical laser cavity of a Distributed Feedback

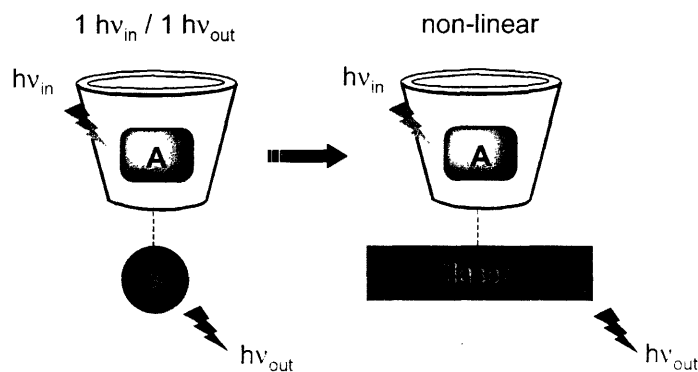


Figure 1.9. The single photon-emitting center of the linear “3R” chemosensing strategy is now replaced with a laser cavity. The emission intensity should increase by 10^N .

(DFB) grating or a spherical cavity resonator. The successful integration of a DFB laser cavity with the 3R sensing strategy is dependent on the development and optimization of the slab waveguide upon which the DFB is built. Chapter 2 will be devoted to the fabrication and characterization of these waveguide films, and their fundamental optical properties will be discussed. In addition, the fabrication of the DFB device, its optical and physical characterization, and investigation of resonance based sensing will be presented. We will then explore the use of DFBs as sensors based on a simple diffraction grating in Chapter 3.

Implementation of 3R is not limited to chemical and biological sensing, and we have applied the “turn on” approach to sensing physical phenomena such as turbulence and fluid vorticity. In collaboration with the Koochesfahani Lab at Michigan State University, our group has developed a diagnostic technique, Molecular Tagging Velocimetry (MTV), for measuring the rate of fluid flow. However, as we attempt to measure very slow flows and in microchannels at near surface boundaries, the fluorescent molecules used do not meet the proper photophysical requirements. Therefore, Chapter 4 will discuss the synthesis and fundamental photophysics of metal-caged dye complexes as new tracers for MTV measurements.

1.4 References

1. de Silva, A. P.; Gunaratne, H. Q. N.; Gunnlaugsson, T.; Huxley, A. J. M.; McCoy, C. P.; Rademacher, J. T.; Rice, T. E. *Chem. Rev.* **1997**, *97*, 1515.
2. *Chemosensors of Ion and Molecular Recognition*, NATO ASI Series C, Vol. 492, Desvergne, J.-P.; Czarnik, A. W., Eds.; Kluwer Academic Publishers: Dordrecht, The Netherlands, 1997.
3. *Fluorescent Chemosensors for Ion and Molecule Recognition*, ACS Symposium Series 538, Czarnik, A. W., Ed.; American Chemical Society: Washington, D.C., 1993.
4. Rudzinski, C. M.; Hartmann, W. H.; Nocera, D. G. *Coord. Chem. Rev.* **1998**, *171*, 115.
5. Czarnik, A. W. *Acc. Chem. Res.* **1994**, *27*, 302.
6. Swager, T. M. *Acc. Chem. Res.* **1998**, *31*, 201.
7. Rudzinski, C. M.; Nocera, D. G. in *Optical Sensors and Switches*, Ramamurthy, V.; Schanze, K. S., Eds.; Marcel Dekker: New York, 2001, p.1.
8. Bell, T. W.; Hext, N. M. *Chem. Soc. Rev.* **2004**, *33*, 589.
9. Mohr, G. J. *Chem. Eur. J.* **2004**, *10*, 1082.
10. de Silva, A. P.; Fox, D. B.; Moody, T. S.; Weir, S. M. in *Optical Sensors and Switches*, Ramamurthy, V.; Schanze, K. S., Eds.; Marcel Dekker: New York, 2001, p. 93.
11. Lehn, J.-M. *Supramolecular Chemistry*; VCH: Weinheim, 1995.
12. Lehn, J.-M.; Ball, P. in *New Chemistry*, Hall, N. Ed.; Cambridge University Press: Cambridge, 2000, p. 300.
13. Pederson, C. J.; Lehn, J.-M.; Cram, D. J. *Resonance* **2001**, *6*, 71.
14. Matthews, S. E.; Beer, P. D. in *Calixarenes*, Asfari, Z., Ed.; Kluwer Academic Publishers: Dordrecht, 2001, p. 421.
15. Beer, P. D.; Gale, P. A. *Angew. Chem. Int. Ed.* **2001**, *40*, 486.
16. Orellana, G. *Anal. Bioanal. Chem.* **2004**, *379*, 344.
17. Sevilla, F.; Narayanaswamy, R. *Comp. Anal. Chem.* **2003**, *39*, 413.

Chapter 1

18. Murphy, C. J. *Anal. Chem.* **2002**, *74*, 520A.
19. Shi, J.; Zhu, Y.; Zhang, X.; Baeyens, W. R.G.; Campana, A. M. G. *Trends Anal. Chem.* **2004**, *23*, 351.
20. Sharp, S. L.; Warmack, R. J.; Goudonnet, J. P.; Lee, I.; Ferrell, T. L. *Acc. Chem. Res.* **1993**, *26*, 377.
21. Ghodrati, M. *Soil Sci. Soc. Am. J.* **1999**, *63*, 471.
22. O'Connell, K. P.; Valdes, J. J.; Azer, N. L.; Schwartz, R. P.; Wright, J.; Eldefrawi, M. E. *J. Immunol. Meth.* **1999**, *225*, 157.
23. Guay, C. K.; Klinkhammer, G. P.; Falkner, K. K.; Benner, R.; Coble, P. G.; Whitley, T. E.; Black, B.; Bussell, F. J.; Wagner, T. A. *Geophys. Res. Lett.* **1999**, *26*, 1007.
24. Eastwood, D.; Lidberg, R. L.; Simon, S. J.; Vo-Dinh, T. in *Chemistry for the Protection of the Environment*, Pawlowski, L., Ed.; Plenum Press: New York, 1991.
25. Xie, X. S. *Springer Ser. Chem. Phys.* **2001**, *67*, 227.
26. Moerner, W. E.; Fromm, D. P. *Rev. Sci. Inst.* **2003**, *74*, 3597.
27. Orrit, M. *Single Molecules*, **2002**, *3*, 255.
28. Hubner, C. G.; Krylov, V.; Renn, A.; Nyffeler, P.; Wild, U. P. *Springer Ser. Chem. Phys.* **2001**, *67*, 161.
29. Frey, H. G.; Witt, S.; Felderer, K.; Guckenberger, R. *Phys. Rev. Lett.* **2004**, *93*, 200801/1.
30. van Hulst, N. F.; Veerman, J.-A.; Garcia-Parajo, M. F.; Kuipers, L. *J. Chem. Phys.* **2000**, *112*, 7799.
31. Nagano, T.; Okamoto, N. *Bio Industry* **2004**, *21*, 5.
32. Lu, P. H. *Curr. Pharm. Biotech.* **2004**, *5*, 261.
33. Blom, H.; Goesch, M. *Curr. Pharm. Biotech.* **2004**, *5*, 231.
34. Boehmer, M.; Enderlein, J. *ChemPhysChem* **2003**, *4*, 792.
35. Klimov, V. I.; Mikhailovsky, A. A.; McBranch, D. W.; Leatherdale, C. A.; Bawendi, M. *G. Science* **2000**, *287*, 1011.

Chapter 1

36. Alivisatos, A. P. *Science* **1996**, *271*, 933.
37. Empedocles, S. A.; Bawendi, M. G. *Acc. Chem. Res.* **1999**, *32*, 389.
38. Keller, R. A.; Ambrose, W. P.; Arias, A. A.; Cai, H.; Emory, S. R.; Goodwin, P. M.; Jett, J. H. *Anal. Chem.* **2002**, *74*, 316A.
39. Michalet, X.; Pinaud, F. F.; Bentolila, L. A.; Tsay, J. M.; Doose, S.; Li, J. J.; Sundaresan, G.; Wu, A. M.; Gambhir, S. S.; Weiss, S. *Science* **2005**, *307*, 538.
40. Wolfbeis, O. S. *Springer Ser. Chem. Sens. Biosens.* **2004**, *1*, 1.
41. Nickel, A-M. L.; Yeh, J.-Y.; Shaw, G. A.; Mawst, L. J.; Kuech, T. F.; Ellis, A. B. *Mol. Supramol. Photochem.* **2003**, *10*, 345.
42. Righini, G. C. *International Trends in Applied Optics*, Guenther, A. H., Ed.; SPIE-The International Society for Optical Engineering: Bellingham, WA, 2002, p. 445.
43. Balzani, V.; Carassiti, V. *Photochemistry of Coordination Compounds*; Academic Press: London, 1970.
44. Forster, L. S. in *Concepts of Inorganic Photochemistry*, Adamson, A. W.; Fleischauer, P. D., Eds.; Wiley-Interscience: New York, 1975.
45. Wayne, R. P. *Principles and Applications of Photochemistry*; Oxford University Press: Oxford, 1980.
46. Jortner, J.; Rice, S. A.; Hochstrasser, R. M. *Adv. Photochem.* **1969**, *7*, 149.
47. Freed, K. F. *Acc. Chem. Res.* **1978**, *11*, 74.
48. Lin, S. H. *Radiationless Transitions*; Academic Press: New York, 1980.
49. Turro, N. J. *Modern Molecular Photochemistry*; Benjamin/Cummings: Menlo Park, 1978.
50. Ferraudi, G. J. *Elements of Inorganic Photochemistry*; Wiley-Interscience: New York, 1988; Chapter 1.
51. Balzani, V.; Moggi, L.; Manfrin, M. F.; Bolletta, F. *Coord. Chem. Rev.* **1975**, *15*, 321.
52. Jackson, J. A.; Turro, C.; Newsham, M. D.; Nocera, D. G. *J. Phys. Chem.* **1990**, *94*, 4500.

Chapter 1

53. Szejtli, J. *Encyclopedia of Nanoscience and Nanotechnology*, Nalwa, H. S., Ed.; American Scientific Publishers: Stevenson Ranch, CA, 2004.
54. Bender, M. L. *Cyclodextrin Chemistry*; Springer-Verlag: New York, 1978; Vol. 6.
55. Szejtli, J. *Chem. Rev.* **1998**, *98*, 1743.
56. Szejtli, J. *Pure Appl. Chem.* **2004**, *76*, 1825.
57. Sliwa, W.; Dondela, B. *Heterocycles* **2000**, *53*, 1595.
58. Hamai, S.; Nakamura, A. in *Handbook of Photochemistry and Photobiology*, Nalwa, H. S., Ed.; American Scientific Publishers: Stevenson Ranch, CA, 2003; p.59-119.
59. Pikramenou, Z. ; Nocera, D. G. *Proc. Sixth Int. Symp. Cyclodextrins* ; Editions de Santé : Paris, 1993 ; p. 259.
60. Rudzinski, C. M. ; Engebretson, D. S.; Hartmann, W. K.; Nocera, D. G. *J. Phys. Chem. A* **1998**, *102*, 7442.
61. Rudzinski, C. M.; Nocera, D. G. *unpublished results*.
62. Zhang, C. X.; Manz, A. in *Biochips*, Xing W.-L.; Cheng, J. Eds.; Springer-Verlag: Berlin, 2003, p. 101.
63. Jakeway, S. C.; de Mello, A. J.; Russel, E. L. *Fresenius' J. Anal. Chem.* **2000**, *366*, 525.
64. Fair, R. B.; Khlystov, A.; Srinivasan, V.; Pamula, V. K.; Weaver, K. N. *Proc. SPIE-Int. Soc. Opt. Eng.* **2004**, *5591*, 113.
65. Rudzinski, C. M.; Young, A. M.; Nocera, D. G. *J. Am. Chem. Soc.* **2002**, *124*, 1723.
66. Arai, T.; Gritschneider, S.; Troeger, L.; Reichling, M. *Nanotech.* **2004**, *15*, 1302.
67. Wang, L.; Fine, D.; Dodabalapur, A. *Appl. Phys. Lett.* **2004**, *85*, 6386.
68. Li, Y. Y.; Cunin, F.; Link, J. R.; Gao, T.; Betts, R. E.; Reiver, S. H.; Chin, V.; Bhatia, S. N.; Sailor, M. J. *Science* **2003**, *299*, 2045.
69. Arnold, M. S.; Avouris, P.; Pan, Z. W.; Wang, Z. L. *J. Phys. Chem. B.* **2003**, *107*, 659.
70. Sauer, M. *Angew. Chem. Int. Ed.* **2003**, *42*, 1790.

Chapter 1

71. Wark, M.; Altindag, Y.; Grubert, G.; Jaeger, N. I.; Schulz-Ekloff, G. in *Host-Guest-Systems based on Nanoporous Crystals*, Laeri, F., Ed.; Wiley-VCH: Weinheim, 2003, p.145.
72. Langlet, R.; Arab, M.; Picaud, F.; Devel, M.; Girardet, C. *J. Chem. Phys.* **2004**, *121*, 9655.
73. Moerner, W. E.; Kador, L. *Phys. Rev. Lett.* **1989**, *62*, 2535.
74. Betzig, E.; Chichester, R. J. *Science* **1993**, *262*, 1422.
75. Weiss, S. *Science* **1999**, *283*, 1676.
76. Bayley, H.; Cremer, P. S. *Nature* **2001**, *413*, 226.
77. Lu, H. P.; Xun, L.; Xie, X. S. *Science* **1998**, *282*, 1877.
78. Neuweiler, H.; Schulz, A.; Bohmer, M.; Enderlein, J.; Sauer, M. *J. Am. Chem. Soc.* **2003**, *125*, 5324.
79. Ha, T.; Enderle, T.; Ogletree, D. F.; Chemla, D. S.; Selvin, P. R.; Weiss, S. *Proc. Natl. Acad. Sci. U. S. A.* **1996**, *93*, 6264.
80. Keren, K.; Krueger, M.; Gilad, R.; Ben-Yoseph, G.; Sivan, U.; Braun, E. *Science* **2002**, *297*, 72.
81. Böhmer, M.; Enderlein, J. *ChemPhysChem* **2003**, *4*, 792.
82. Eggeling, C.; Brand, L.; Seidel, C. A. M. *Bioimaging* **1997**, *5*, 105.
83. Zang, L.; Ruchuan, L.; Holman, M. W.; Nguyen, K. T.; Adams, D. M. *J. Am. Chem. Soc.* **2002**, *124*, 10640.
84. de Silva, A. P.; Fox, D. B.; Huxley, A. J. M.; Moody, T. S. *Coord. Chem. Rev.* **2000**, *205*, 41.
85. Barrelet, C. J.; Greytak, A. B.; Lieber, C. M. *Nano Lett.* **2004**, *4*, 1981.
86. Patolsky, F.; Zheng, G.; Hayden, O.; Lakadamyali, M.; Zhuang, X.; Lieber, C. M. *Proc. Nat. Acad. Sci. USA* **2004**, *101*, 14017.
87. Michalski, P. J.; Sai, N.; Mele, E. J. *Cond. Mat.* **2005**, 0501265.

Chapter 1

88. Kolmakov, A.; Moskovits, M. *Annu. Rev. Mater. Res.* **2004**, *34*, 151.
89. Star, A.; Gabriel, J.-C. P.; Bradley, K.; Gruner, G. *Nano Lett.* **2003**, *3*, 459.
90. Cui, Y.; Wei, Q. Q.; Park, H. K.; Lieber, C. M. *Science* **2001**, *293*, 1289.
91. Dai, H. *Acc. Chem. Res.* **2002**, *35*, 1035.
92. Chen, R. J.; Choi, H. C.; Bangsaruntip, S.; Yenilmez, E.; Tang, X.; Wang, Q.; Chang, Y.-L.; Dai, H. *J. Am. Chem. Soc.* **2004**, *126*, 1563.
93. Zheng, G.; Lu, W.; Jin, S.; Lieber, C. M. *Adv. Mater.* **2004**, *16*, 1890.
94. Cui, Y.; Duan, X.; Huang, Y.; Lieber, C. M. in *Nanowires and Nanobelts*, Wang, Z. L., Ed., Kluwer Academic Publishers; Norwell, MA, 2003, p. 3.
95. Wu, Y.; Xiang, J.; Yang, C.; Lu, W.; Lieber, C. M. *Nature* **2004**, *430*, 61.
96. Zhang, Y.; Kolmakov, A.; Lilach, Y.; Moskovits, M. *J. Phys. Chem. B* **2005**, *109*, 1923.
97. Qi, P.; Vermesh, O.; Grecu, M.; Javey, A.; Wang, O.; Dai, H.; Peng, S.; Cho, K. J. *Nano Lett.* **2003**, *3*, 347.
98. Kong, J.; Franklin, N. R.; Zhou, C. W.; Chapline, M. W.; Peng, S.; Cho, K. J.; Dai, H. *Science* **2000**, *287*, 622.
99. Bayley, H.; Cremer, P. S. *Nature* **2001**, *413*, 226.
100. Bayley, H.; Braha, O.; Gu, L.-Q. *Adv. Mater.* **2000**, *12*, 139.
101. Bard, A. J.; Faulkner, L. R. *Electrochemical Methods: Fundamentals and Applications*; John Wiley & Sons: New York, 1980; Chapter 1.
102. Chen, R. J.; Choi, H. C.; Bangsaruntip, S.; Yenilmez, E.; Tang, X.; Wang, Q.; Chang, Y.-L.; Dai, H. *J. Am. Chem. Soc.* **2004**, *126*, 1563.
103. Roschier, L.; Pentilla, J.; Martin, M.; Hakonen, P.; Paalanen, M.; Tapper, U.; Kauppinen, E. J.; Journet, C.; Bernier, P. *Appl. Phys. Lett.* **1999**, *75*, 728.
104. Tans, S. J.; Verschueren, A. R. M.; Dekker, C. *Nature* **1998**, *393*, 49.
105. Bezryadin, A.; Verschueren, A. R. M.; Tans, S. J.; Dekker, C. *Phys. Rev. Lett.* **1998**, *80*, 4036.

Chapter 1

106. Franklin, N. R.; Wang, Q.; Tomblor, T. W.; Javey, A.; Shim, M.; Dai, H. *Appl. Phys. Lett.* **2002**, *81*, 913.
107. Guillorn, M. A.; Haile, M. D.; Merkulov, V. I.; Simpson, M. L.; Eres, G. Y.; Cui, H.; Puretzsky, A. A.; Geohegan, D. B. *Appl. Phys. Lett.* **2002**, *81*, 2860.
108. Ramanathan, K.; Bangar, M. A.; Yun, M.; Chen, W.; Myung, N. V.; Mulchandani, A. *J. Am. Chem. Soc.* **2005**, *127*, 496.
109. Kim, W.; Javey, A.; Vermesh, O.; Wang, O.; Li, Y. M.; Dai, H. *Nano Lett.* **2003**, *3*, 193.
110. Zhang, Y.; Kolmakov, A.; Lilach, Y.; Moskovits, M. *J. Phys. Chem. B* **2005**, *109*, 1923.
111. Fan, Z.; Wang, D.; Chang, P.-C.; Tseng, W.-Y.; Lu, J. G. *Appl. Phys. Lett.* **2004**, *85*, 5923.

**Chapter 2. Distributed Feedback Grating Architectures
for High Gain Sensing**

2.1 Introduction

2.1.1 Laser Cavities

The motivation for using a laser cavity in 3R sensing schemes is driven by the nonlinear signaling properties of such a device. The intensity of light can build exponentially as light propagates in a cavity with an inverted excited state population. This exponential increase in intensity is given by,¹

$$I = I_0 e^{g(\nu)z} \quad (2.1)$$

where I_0 is the impinging intensity, I is the intensity at some distance z into the cavity, and $g(\nu)$ is the gain coefficient given by,

$$g(\nu) = \frac{h\nu [N_u B_u(\nu) - N_l B_l(\nu)]}{c} \quad (2.2)$$

$N_{u(l)}$ is the upper (lower) level population and $B_{u(l)}(\nu)$ is the emission (absorption) probability at frequency ν . By separating the Einstein $B_{u(l)}$ coefficients from population inversion, eq. (2.2) can be recast,

$$I = I_0 e^{\sigma(\nu)\Delta N_{ul}z} \quad (2.3)$$

where $\sigma(\nu)$ is the stimulated emission cross-section. The term ΔN_{ul} is related to the population inversion by $\Delta N_{ul} = [N_u - (d_u/d_l)N_l]$, including a statistical weight factor, $d_{u/l}$, which accounts for degeneracy.

The conditions associated with amplification that are necessary (but not sufficient) for producing a laser are a population inversion, and sufficient gain to reach saturation intensity (I_{sat}). In examining eq. (2.3), if the value of the exponent is positive, then the light output will increase in intensity and amplification will occur. Since the values of $\sigma(\nu)$ and z are always positive, amplification will only occur if $N_u > (g_u/g_l) \cdot N_l$. In tuning parameters of eq. (2.3), a relatively large ΔN_{ul} is a necessity.² The stimulated emission cross-section is an intrinsic

property of the specific transition in a particular gain medium and therefore offers little control. The medium length, on the other hand, may be perturbed considerably by controlling the architecture of the lasing cavity. High intensities, and thus the maximal response from the laser cavity can most easily be achieved by confining light within the cavity of a laser resonator. Confinement in conventional Fabry-Perot resonators is achieved by reflection of light off a front and back mirror to increase the effective length (L_{eff}) of the laser cavity as shown in Figure 2.1. The addition of N mirrors to the cavity can result in an even greater increase of L_{eff} as long as the cavities are appropriately coupled.

In a Distributed Feedback (DFB) cavity, the “mirrors” are formed by a ruled grating. In this architecture, the wavelength of light is on the same length scale as the individual cavities and hence the conventional picture of Figure 2.1 does not hold. Rather, the effect of the “mirrors” introduces a periodic modulation of the local refractive index along the path of light propagation. This resonant increase of pathlength, or feedback, for both DFB and spherical cavities can result in a sharp and intense amplification of light via stimulated emission processes. If an analyte can affect ΔN_{ul} by removing (“turn off”) or adding (“turn on”) energy into the cavity, then the gain coefficient will be perturbed, thus leading to an exponential change in the laser output. Of the

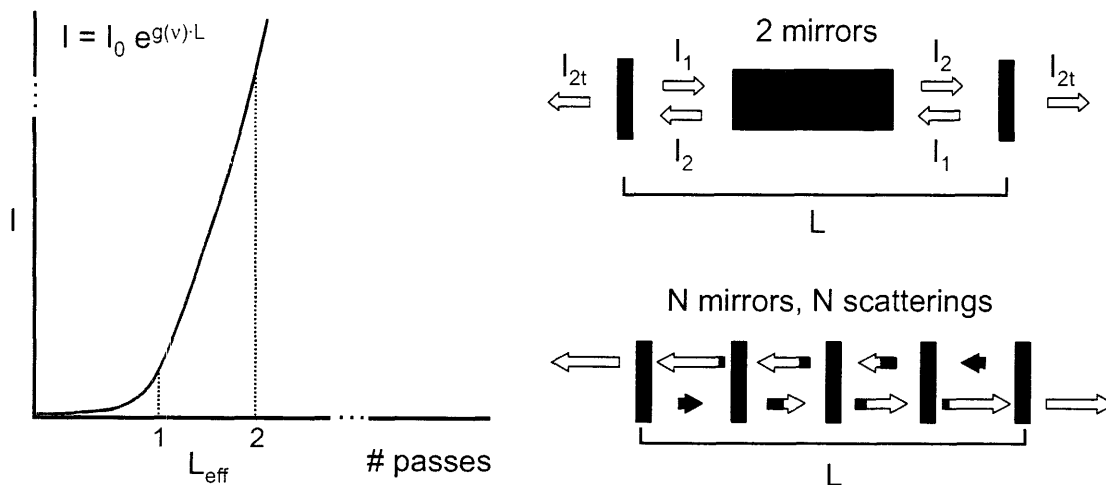


Figure 2.1. Increasing the number of mirrors in a laser cavity results in an exponential increase in the intensity, due to the significant lengthening of L_{eff} .

two, a loss mechanism is the easiest to implement. The gain coefficient can be altered by chemically functionalizing the DFB laser structure with molecular recognition sites, where absorption of the propagating light by a specific analyte docked at the receptor site will turn the laser off when the net gain drops below threshold.

2.1.2 Asymmetric Slab Waveguides

The DFB grating architecture is built upon an asymmetric slab structure, whose physical and optical properties must be optimized to achieve the desired waveguiding abilities. As shown in Figure 2.2, the slab waveguide consists of a dielectric film sandwiched between two cladding layers of lower refractive indices:¹ air ($n_1 = 1.0$) and substrate ($n_{3=\text{glass}} = 1.5$). The synthesis of the films was focused on the attainment of the following three parameters: (1) a smooth surface morphology to minimize scattering at the surface of the waveguide, (2) a sufficient refractive index mismatch between the waveguiding medium and substrate ($n_2 > 1.5$), and (3) an appropriate film thickness (d) to confine the waveguided light.

With the limiting conditions of a refractive index mismatch, light will propagate along the long axes as a result of total internal reflection (TIR) occurring at the interfaces provided that the angle of incidence (θ) relative to the interface normal is greater than the critical angle, θ_c .

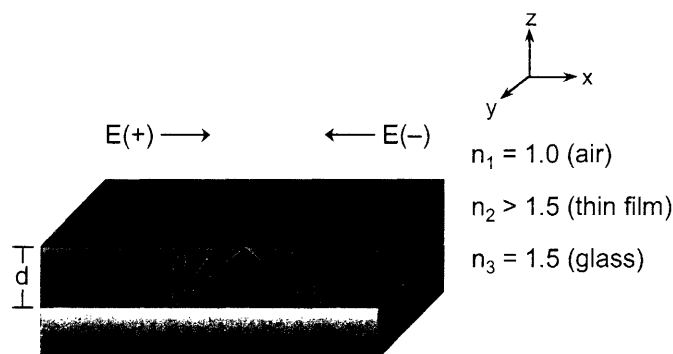


Figure 2.2. Schematic of an asymmetric slab waveguide: the thin film (n_2) has an index mismatch with n_1 and n_3 . Total internal reflection (TIR) occurs at this interface. $E(+)$ constructively interferes with $E(-)$ at allowed angles θ_m ($m = \text{mode}$).

Chapter 2

From Figure 2.2, the critical angle is defined by,¹

$$\cos \theta_c = \frac{n_3}{n_2} \quad (2.4)$$

This describes the mode confinement, where the positive electric field (E+) constructively interferes with the negative field (E-) only at discrete angles, θ_m , provided the coherent waves are traveling in the same direction with the same phase. The finite number of modes of an asymmetric waveguide can be classified as transverse electric (TE) and transverse magnetic (TM) modes. We are simply interested in the TE modes, which do not have a component of the electric field in the direction of wave propagation. The eigenvalue equation, describing the guided TE modes for the asymmetric waveguide, stem from the solutions of Maxwell's equations and is given by,¹

$$\tan \beta d = \beta \frac{(\gamma + \delta)}{(\beta^2 - \gamma\delta)} \quad (2.5)$$

where $\beta = n_2 k \sin \theta$, $\gamma = [(n_2^2 - n_3^2)k^2 - \beta^2]^{1/2}$, $\delta = [(n_2^2 - n_1^2)k^2 - \beta^2]^{1/2}$, and $k = 2\pi/\lambda = \omega/c$. For a guided mode in the film, there is a propagation constant, β , which is the x-component of the wave vector. For a film with thickness d , there is an evanescent field phase shift φ_i at each of the film's boundaries ($i = 1, 3$) and for self-consistency, the sum of all these phase shifts must be a multiple of 2π . Therefore, the transverse resonance condition is given as,^{1,3}

$$2kn_2d \cos \theta = 2m\pi + 2\varphi_1 + 2\varphi_3 \quad (2.6)$$

For the transverse electric (TE) modes, the phase shifts φ_1 and φ_3 are given by,¹

$$\varphi_i = \tan^{-1} \left[\frac{(n_{eff}^2 - n_i^2)}{(n_2^2 - n_{eff}^2)} \right]^{\frac{1}{2}} \quad (2.7)$$

where each allowed mode propagates with a particular phase velocity characterized by an effective mode index, $n_{eff} = n_2 \sin \theta_c$. The above eq. (2.6) is basically the dispersion relation of the

waveguide, yielding the propagation constant β as a function of the frequency ω and film thickness d .

From the dispersion relation, one can obtain the minimum thickness (d) that will support specific mode(s) of waveguided light. The cut-off condition occurs at the boundary when $\beta = n_2 k$ and $\gamma = 0$. Therefore, the cut-off value of the film thickness for each mode ($m = 0, 1, 2, \dots$) can be obtained when the following equation is solved,¹

$$\tan^{-1} \left[\frac{(n_3^2 - n_1^2)^{1/2}}{(n_2^2 - n_3^2)} \right] + m\pi = kd(n_2^2 - n_3^2)^{1/2} \quad (2.8)$$

The cut-off condition for asymmetric slab waveguides is identical to the loss of TIR for these structures. Ideal waveguides demonstrate single mode emission, and therefore we limit the thickness of our films to within the ($m = 0$) and ($m = 1$) cut-off thickness minima.

2.1.3 Distributed Feedback Structures as Laser Cavities

The DFB lasing architecture is produced by imposing on the slab waveguide a grating^{4,5} of period (Λ) that satisfies the Bragg condition,

$$\Lambda = \frac{\lambda_B m}{2n_{\text{eff}}} \quad (2.9)$$

where λ_B is the Bragg wavelength that is supported by period Λ , m is the order of the grating reflection, and n_{eff} is the effective refractive index. The lasing medium must have a gain profile

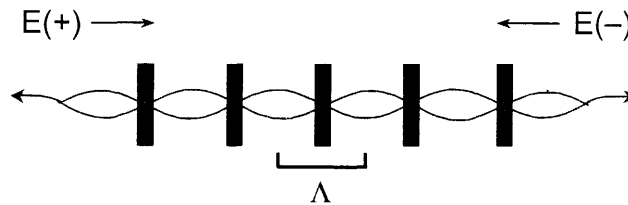


Figure 2.3. Schematic of the counter propagating waves $E(+)$ and $E(-)$ along a DFB cavity with period Λ . Oscillation occurs at the Bragg wavelength λ_B .

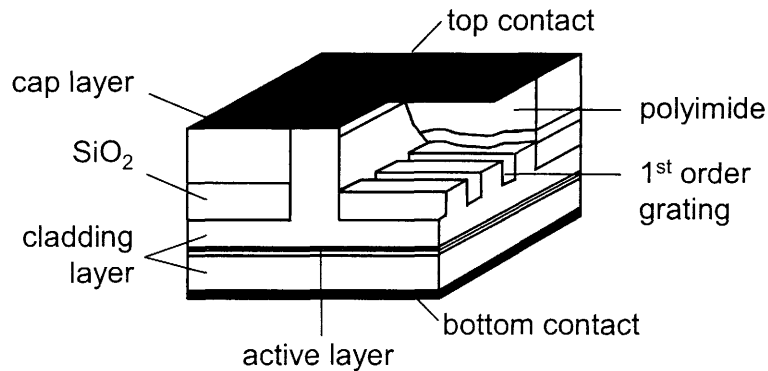


Figure 2.4. Diagram of an example of a laterally coupled ridge waveguide DFB laser using InGaAs/AlGaAs, InGaAsP/InP and other similar materials. [Ref. 10]

that is coincident with λ_B . As each wave travels in the periodic structure shown in Figure 2.3, it receives light at each point by Bragg scattering from the oppositely traveling wave. This distributes the feedback mechanism throughout the length of the periodic structure; the structure should have gain so that with sufficient feedback, oscillation will occur. As the propagating wave traverses the DFB grating, lasing can result when there is constructive oscillating feedback of the stimulated emitted light. Referencing to Figure 2.1, we can imagine the distribution of reflection (feedback) as the periodic modulation of the refractive index or gain of the medium, which is effectively implementing N mirrors over the length of a DFB cavity device. Thus, the N scatterings provide oscillation.

The ability to make optically robust thin film lasers has been a significant challenge, although layered semiconductor DFB lasers have already been fabricated.⁶⁻⁹ As shown in Figure 2.4, laterally coupled waveguide DFB laser consists of a substrate, cladding layer, active layer, first order grating, silicon oxide, and upper cladding layers.¹⁰ Various methods for conventional semiconductor DFBs have been demonstrated, including etching the gratings directly above the waveguide and injecting the current from the side,¹¹ or by etching the gratings through the upper cladding layers to provide index guiding for selective feedback.¹² These fabrication methods are demanding, with complicated etching processes and focused ion beam lithography. More simplified processes have since been introduced, especially for the construction of optical DFB

laser diodes that do not require wavelength modulation by the tuning of the laser injection current.¹³⁻¹⁶ First or second order Bragg surface emitting architectures can be constructed, depending on whether the grating should or should not provide a means of out-coupling the radiation. Laser action can be obtained by the interference of two pumping beams in the active medium, and the technique of dynamic grating formation onto dye-doped polymer waveguides was achieved with a frequency-doubled or tripled Nd:YAG laser.¹⁷ Two methods were applied to demonstrate DFB lasing action on poly(methyl methacrylate) (PMMA) films, both of which involved photolithographically patterning the grating with interfering UV lasers. Lo and co-workers demonstrated DFB laser action in sol-gel films, where the optical arrangement was in the Bor configuration and required crossing beams of a frequency-doubled Nd:YAG laser at an intersection angle of 2θ .¹⁸⁻²⁰

Distinct from traditional lasers based on bulk optics, waveguide lasers offer the option of using distributed feedback (DFB) or distributed reflectivity (DBR). These configurations are preferential to those resonators that are built strictly with localized reflectors.²¹⁻²³ The use of reflecting facets results in high power concentration at those points and limits the output power due to the danger of damaging the emitting surfaces. In addition, the wide gain band of a semiconductor laser medium and the weak frequency selectivity of a Fabry-Perot resonator result in the excitation of multiple modes whose spectral envelope ranges from several nanometers. With DFB structures, these problems are avoided by providing high wavelength selectivity and the opportunity of distributed surface extraction of radiation through the grating. If using dye-doped structures, the wavelength control advantages are further exemplified because of the larger gain bandwidth of dye media.

2.1.4 Thin Film Distributed Feedback (DFB) Lasers

Planar waveguides are well adapted for evanescent wave sensing using grating couplers and sensitive polymeric films. The basic planar devices shown in Figure 2.5 involve the analyte/sample with refractive index (n_A) deposited onto a prism or a plane surface (n_2). There

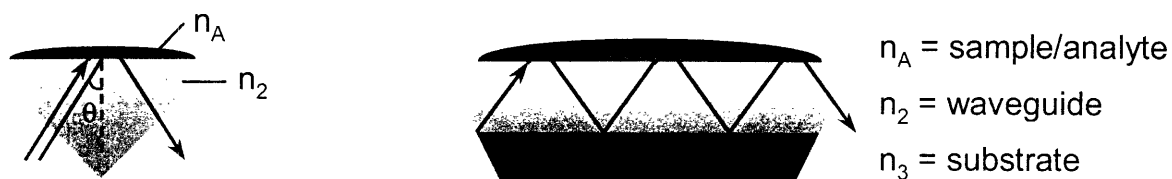


Figure 2.5. Configurations of practical planar waveguides for chemical sensing: (a) prism or plane surface with refractive index n_2 and analyte with n_A , and (b) planar waveguide n_2 that can adsorb analyte in sample (n_A) deposited onto a support substrate of n_3 .

are different configurations for planar devices with an embedded slab waveguide commonly found in chemical sensors using spectroscopic techniques: a simple planar waveguide where the light is totally reflected at the substrate interface (n_2 / n_3) and partially reflected at the sample interface (n_A / n_2). If the waveguide consists of a thin film that adsorbs the targeted analyte, the resulting change in film thickness or refractive index is monitored by shifts in the waveguide propagation modes. Typical immobilization supports in these heterogeneous systems are polymeric or silicate-based, where the reporter and/or recognition sites are either entrapped or covalently attached to the matrix of choice. A large majority of the polymers (i.e., polystyrenes and polyethylenes) and glass supports absorb UV wavelengths and their fluorescence upon excitation produces a background that is disadvantageous for optical sensor applications.

Our application of a DFB cavity requires that it be sensitive to target analytes. In this regard, conventional semiconducting DFB matrices are not attractive owing to the difficulty with their modification. In our design, the DFB cavity must host molecular chemosensors, allow for the penetration of analyte, and possess a surface that can easily be modified with a receptor site. The material must also be “soft” enough to allow for lithographic imprinting of the grating architecture, but stable enough to bear high energy excitation and its surrounding environment. For these reasons, we turned our attention to the use of silicate glasses as a DFB medium. Polysilicate gels, commonly known as sol-gels, are advantageous as the waveguide material because their tunable porosity allows them to act as a host matrix for analyte and chromophores. In addition, the surfaces of these materials are hydroxide and alkyl-terminated, allowing for

facile chemical modification. They also exhibit appropriate spectroscopic properties to support stimulated emission.²⁴⁻²⁸ Subsequent sections detail the development of the sol-gel derived thin film waveguides as the foundation upon which a DFB cavity can be built.

A major challenge for the sol-gel thin films is the successful, *facile* incorporation of a DFB grating to achieve narrow linewidth stimulated emission from these architectures. Recently, nanocrystals (NCs) incorporated into thin films have been shown to achieve stimulated emission.²⁹ The NCs were stabilized within titania sol-gel matrices and ASE was achieved both at 80K and at room temperature.³⁰ Nanocrystals are advantageous to organic laser dyes because of their high photostability, broad absorbance, narrow emission linewidths, and color tunability. However, with the variability and unpredictability of NC synthesis, where highly fluorescent and low dispersion in the quantum dots are crucial, the facile incorporation of organic and other chromophores into the waveguide films is one of the major advantages of the matrices. Embossing strategies derived from literature methods can be implemented with the SiO₂ / TiO₂ films, where an elastomeric mold is used to transfer the DFB pattern onto the films. Using soft lithography should simplify the preparation of thin film DFBs.

2.1.5 High Gain Sensing Strategies

The exponential dependence of the laser intensity on the gain coefficient, expressed in eq. (2.3), emphasizes emphasizes two ways to generate an exponential response from a mesoscopic laser cavity in the presence of chemical analytes:

- (1) The excited state population may be reduced through resonance energy transfer loss channels. We can fabricate non-linear photonic devices of a size similar to the sub-micron length scale at which Förster energy transfer occurs.^{31,32} Consequently, the loss of the excited state concentration (decrease in ΔN) will represent a significant portion of the total population inversion resulting in a large change in the amplified laser intensity. Alternatively, we may also use an energy transfer mechanism to

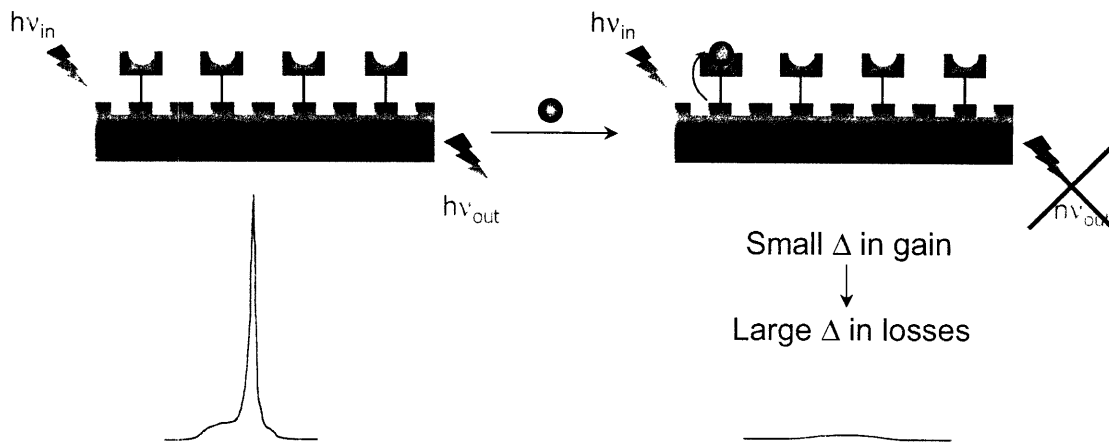


Figure 2.6. High gain sensing strategy involving a surface modified DFB laser cavity. Upon binding of analyte to the receptor sites, absorption of the analyte at the lasing wavelength perturbs the gain leading to the loss of lasing, as exemplified in eq. (2.3).

enhance the excited state population through direct excitation of the analyte. The lasing wavelength (λ_L) of the DFB will be adjusted to overlap the absorption profile of the analyte, thus enabling energy transfer to occur.

- (2) The sensitivity of a non-linear device may be enhanced through the use of using cavities with high quality (Q) factors. The Q of the cavity is the timescale that energy is stored in the cavity compared to the rate of energy loss. Consequently, higher Q cavities will have longer photonic storage times, thus increasing the effective length scale over which the laser light is amplified. As a result, the change in intensity (sensitivity) as a result of the loss or gain of excited state population is exponential with respect to the length scale of laser light amplification. Additional sensitivity may be incorporated into a cavity by the direct modification of the Q factor itself. In the devised DFB sensor where laser amplification occurs, the presence of a receptor that absorbs upon detection of analyte in the grooves of the functionalized device may spoil the Q factor. Thus, the DFB device will show exponential sensitivity to target analytes through the loss of population inversion as well as Q factor reduction.

The surface modified laser cavity with receptor sites will be specific towards a targeted analyte. Upon binding of analyte, as shown in Figure 2.6, the absorption by the analyte at or near the lasing wavelength of the DFB cavity will perturb the gain and deactivate the laser cavity. Although this will be in effect a “turn off” sensor, the dimming of an intense laser emission will be readily detected against even a bright background. The extreme sensitivity of this non-linear sensing strategy is similar in magnitude to the detection limits of the absorption techniques of cavity ring-down (CRDS) and intracavity laser absorption (ICLAS) spectroscopies.

2.1.6 Parallels to Cavity Ring-down Spectroscopy

Single molecule detection requires highly sensitive quantitative techniques that can discriminate the targeted analyte from ubiquitous contaminants. Absorption spectroscopy is an attractive alternative for trace vapor detection; molecules absorb light at distinct, characteristic wavelengths allowing for the unique spectral identification of a chemical by measuring its absorption spectrum. However, traditional linear methods do not have the requisite sensitivity for detecting ppb or less. For example, carbon dioxide has an absorption at 1572.66 nm with a line strength of $\sim 1.8 \times 10$ cm / molecule;³³ to detect 100 ppm with a 5 cm cell requires an absorption measurement of 10^{-6} , which is beyond the limit of current systems. Trace gas detection is important for safety and environmental monitoring, and optical fibers and other types of micro-optic cells have made use of multi-pass techniques such as CRDS and ICLAS to increase the sensitivity of the gas sensors.³⁴ ICLAS and CRDS are related, powerful absorption techniques that obtain its sensitivity from allowing the possibility of very long effective cell lengths.^{35,36} CRDS involves placing a gas absorber in a cavity and monitoring the gas absorption via the loss of the cavity, which is determined from the decay time of light injected into the cavity. A simplified schematic of the detection setup is shown in Figure 2.7. Light from a pulsed or CW laser source is injected into a stable optical cavity formed by two, or more highly reflective mirrors. At the end of the laser pulse, or when the laser is turned off for CW radiation, the intracavity radiation will decay exponentially with a time constant (τ) that can be related as,³⁷

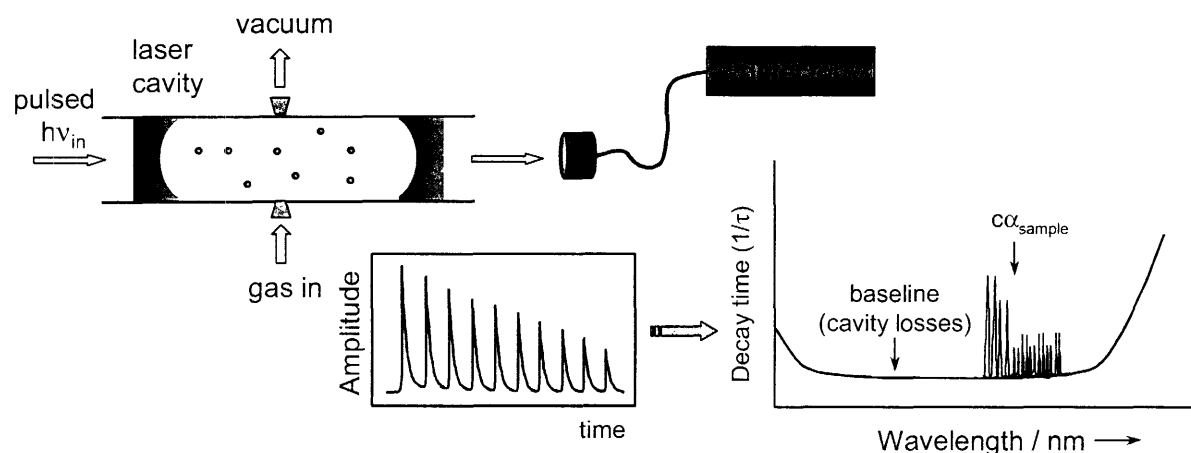


Figure 2.7. Simplified diagram of a setup for CRDS detection of trace vapor gas.

$$\frac{1}{c\tau} = \alpha(\lambda) + \frac{n(1-R) + A}{L} \quad (2.10)$$

where c is the speed of light, L is the roundtrip cavity length, and n is the number of cavity mirrors. The decay time is dependent upon the reflectivity of the mirrors (R), the round-trip loss due to scattering inside the cavity (A), and the wavelength dependent absorption of the intracavity gas, $\alpha(\lambda)$. Once the baseline losses in an empty cavity are determined (from R and A), the absolute absorption spectrum of the intracavity medium is immediately extracted by tuning the laser source and plotting $1/(c\tau)$ as a function of wavelength. The intracavity sample absorption per pass is obtained as a variation of cavity losses when the sample is admitted into the cavity, or when the wavelength is tuned around an absorption line. Another advantage of CRDS is that the absorption measurement is insensitive to laser intensity fluctuations.^{35,38} The cavity length L has a significant effect on the minimum absorption coefficient of the sample. For a single pass technique, the minimum $\alpha_{sample} \sim 10^{-3}-10^{-4} \text{ cm}^{-1}$ while for ICLAS or CRDS ($\sim 100,000$ passes), the minimum $\alpha_{sample} \sim 10^{-6}-10^{-11} \text{ cm}^{-1}$. Steinfeld and co-workers have demonstrated, using a CRDS set-up with a sensitivity of $2 \times 10^{-8} \text{ cm}^{-1}$ and reduced pressures (100 torr) of gas, baseline detection limits of approximately 1.2 ppb of TNT and similar explosives can be obtained.³⁷

Chapter 2

The increase in sensitivity garnered with the CRDS instrument, however, requires accompanying recognition algorithms to distinguish targeted analytes from the large number of interferents. While the absorbance signatures for the gases are distinct, some spectra contain only one feature that can overlap with peaks from interferents that absorb in the same region (e.g., water). The need to compile a spectral library of interferents and possible mixtures of compounds is a disadvantage of this technique. In addition, the quick sampling time needed for identification of explosives vapor (10 – 20 s) is too short to acquire a spectrum in the 2 μm window.

We seek to implement the approach of increased cavity path length of CRDS and ICLAS, which can offer 7 orders of magnitude increase in detection limit relative to linear methods, to our 3R sensing strategy with the hopes of extending detection to the single molecule limit.³⁹ This Chapter will describe the fabrication of thin film DFB laser cavities on optimized SiO_2 / TiO_2 matrices using soft lithography techniques. These structures can enable non-linear sensing through the expression in eq. (2.3) by perturbing the gain coefficient.

2.2 Results and Discussion

2.2.1 Synthesis of Thin Films

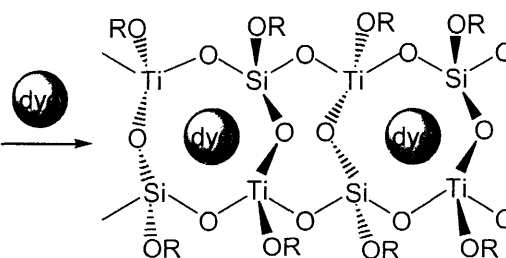
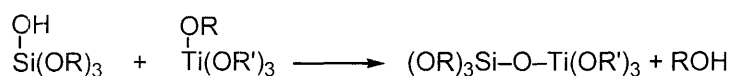
The matrix of choice for the slab waveguide was of a $\text{SiO}_2 / \text{TiO}_2$ composition. These films are attractive for waveguide construction because they are optically transparent through the visible and UV spectra regions, exhibit high optical homogeneity, their surfaces may be chemically modified, and their porosities can be tuned.^{40,41} Molecular doping into inorganic media not only stabilizes the guest organic molecules in the thin-film state, but it also exploits the optoelectronic potential of each “isolated” chromophore. The sol-gel technique for encapsulating organic chromophores is advantageous because its low-temperature process involving metal alkoxides allows for facile doping with less thermally stable molecules. Films were synthesized, according to Scheme 2.1, via conventional acid-catalyzed hydrolysis and condensation methods of sol-gel silicates prepared from $\text{Si}(\text{OEt})_4$ and $\text{Ti}(\text{OR})_4$ precursors ($\text{R} = \text{Bu}, \text{Et}$).^{24,40-42} After sufficient cross-linking, the sol-gel was then spin coated onto substrates and annealed at a high temperature to cure the films for subsequent characterization. Long reaction times resulted in the formation of either too viscous of a solution or a solidified gel, both useless for thin film preparation.

Chromophores were incorporated into the thin films in order to study the waveguiding

Partial Hydrolysis



Heterocondensation



Scheme 2.1. General sol-gel synthesis of the $\text{SiO}_2 / \text{TiO}_2$ matrix, where ($\text{R} = \text{Et}$) and ($\text{R}' = \text{Et}, \text{Bu}$). The dye chromophore is introduced in the acid-catalyzed condensation reaction, and further cross-linking formed the porous material.

properties of the synthesized materials. Laser dyes of varying photophysical properties were introduced at the condensation stage of the synthesis; these dyes included Coumarin 152 (C152; $\lambda_{\text{abs}} = 397 \text{ nm}$; $\lambda_{\text{ems}} = 510 \text{ nm}$), Sulforhodamine B ($\lambda_{\text{abs}} = 556 \text{ nm}$; $\lambda_{\text{ems}} = 575 \text{ nm}$), Rhodamine B ($\lambda_{\text{abs}} = 552 \text{ nm}$; $\lambda_{\text{ems}} = 580 \text{ nm}$), and Rhodamine 6G (R6G; $\lambda_{\text{abs}} = 530 \text{ nm}$; $\lambda_{\text{ems}} = 556 \text{ nm}$). The ability to dope the matrix with dyes of varying absorbance and emission properties (solution values given above) indicates the tunability of this reaction. Initial characterization studies were conducted on C152-doped samples, and the film's thickness and index dependence on the spin coating rate, annealing temperature and time, dye concentration, and [Si]:[Ti] were determined.

2.2.2 Composition Effects on Film Properties

Both the refractive index and smoothness of the films were tuned by varying the [Si]:[Ti] composition. The addition of titania to the films was needed to increase the refractive index and to facilitate thermal dissipation within the film (and thus prevent cracking under high light excitation fluxes). However, films containing higher titania concentrations yielded surfaces that were too rough and crystalline for proper waveguiding. Increasing the [Ti] also resulted in a smaller porosity of the films, therefore rendering the films less permeable to analytes and dopants.⁴² A systematic study of the film composition and its effect on the film's waveguide properties was undertaken.

Examination of the 2:1 [Si]/[Ti] films with a FTIR-coupled microscope and Atomic Force Microscopy (AFM) revealed extremely smooth surfaces. Films with mean surface roughness (rms) values of less than $\pm 0.5 \text{ nm}$ are considered to be very smooth. The AFM of a 2:1 [Si]/[Ti] film is shown in Figure 2.8(top). The rms was found to be $\pm 0.311 \text{ nm}$. Increasing the titania concentration produced samples that exceeded the $\pm 0.5 \text{ nm}$ rms condition; some films were visibly rough to the naked eye. An AFM image of one of these rougher samples (rms = $\pm 0.602 \text{ nm}$) is shown in Figure 2.8 (bottom).

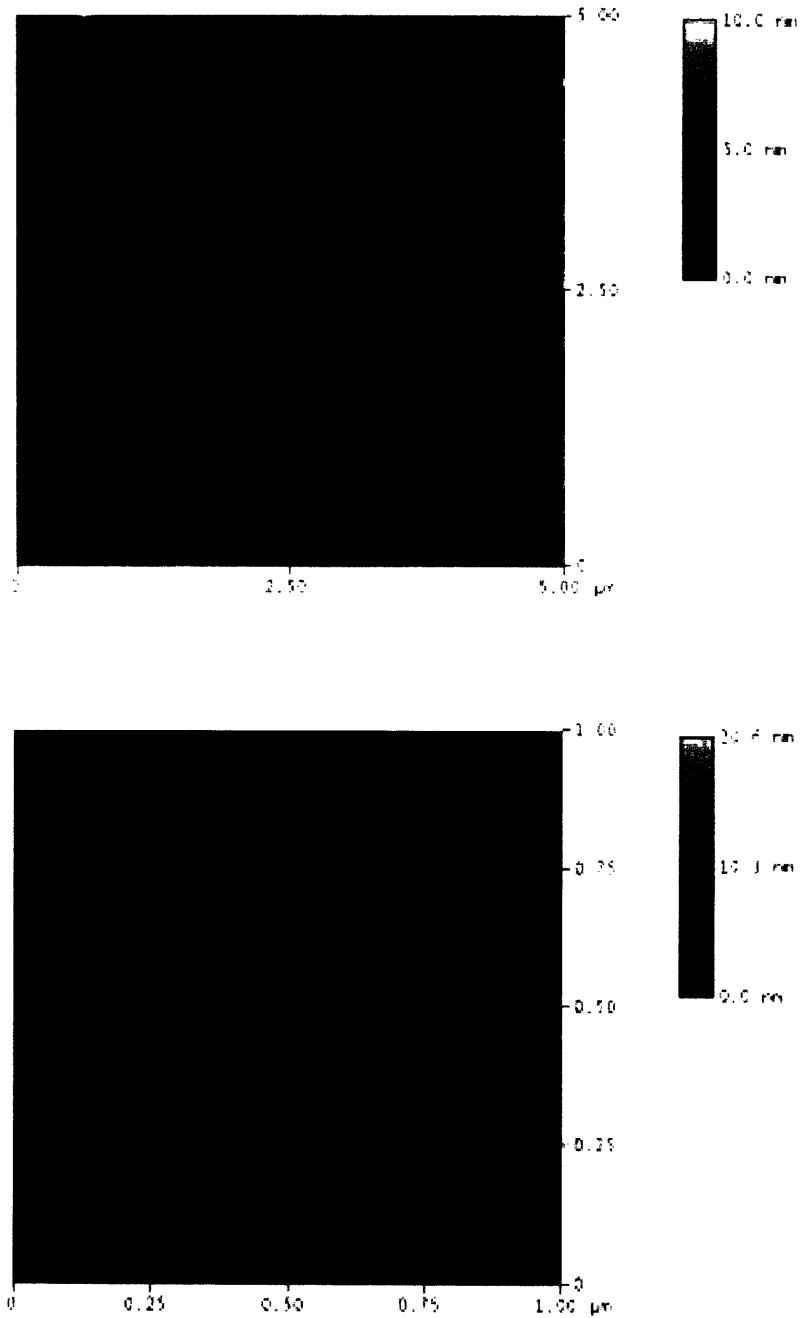


Figure 2.8. (top) AFM image of a 5 μm x 5 μm area of a 2:1 [Si]/[Ti] film with a rms = ±0.311 nm. (bottom) AFM image of a rougher film with rms = ±0.602 nm.

Chapter 2

The necessary optical constants and film thicknesses were obtained from optical ellipsometry measurements, which give the phase difference (Δ) of light relative to the incident light, and the angle (Ψ) whose tangent is the ratio of the magnitudes of the total reflection coefficients. For the spectroscopic ellipsometry measurements, Δ and Ψ were fit to a regression algorithm to obtain the Cauchy coefficients for $n(\lambda)$ and $k(\lambda)$, the real and imaginary refractive indices, respectively. The equations for $n(\lambda)$ and $k(\lambda)$ are often approximated by,⁴³

$$n(\lambda) = A + \frac{B}{\lambda^2} + \frac{C}{\lambda^4}; \quad k(\lambda) = \frac{D}{\lambda} + \frac{E}{\lambda^3} + \frac{F}{\lambda^5} \quad (2.11)$$

where A , B , C are the Cauchy coefficients and D , E , F are the Cauchy extinction coefficients. These Cauchy coefficients may be interpolated from the data to derive the film thickness (d) and refractive index (n) as a function of wavelength.

Single wavelength ellipsometry experiments were conducted on first generation samples (C152-doped). Discrepancies were found at differing single wavelengths. Such anomalies can result from absorbance of the films at the excitation wavelength since the solution of the instrumental solution parameters to generate the calculated refractive indices assumes film transparency at exciting wavelengths. For films of smaller thicknesses, data was reliably obtained and found reproducible for $\lambda_{\text{exc}} = 830$ nm.

A more accurate solution of the refractive index and film thickness is achieved from spectroscopic ellipsometry measurements. A plot of the refractive index as a function of the propagating frequency for a typical synthesized thin film is shown in Figure 2.9. For this sample, the thickness was calculated to be 349 nm and the refractive index at $\lambda = 585$ nm (propagating wavelength of light) was found to be ~ 1.59 . The average refractive index of the 2:1 [Si]/[Ti] R6G-incorporated matrices is $n = 1.6$. Increasing the titania concentration to 1.72:1 [Si]/[Ti] gave $n_2 \sim 1.7$, and films composed of 100% TiO_2 had a refractive index of approximately 1.92. It is important to note that d and n are calculated values, and they are independently verified with surface profilometry measurements of the film thickness.

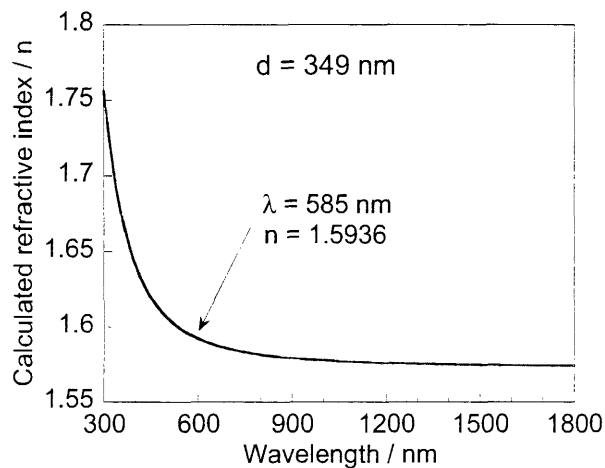


Figure 2.9. A plot of the calculated refractive index as a function of wavelength, obtained from spectroscopic ellipsometry measurements. For this film sample, a thickness of 349 nm and $n = 1.59$ ($\lambda = 585$ nm) were obtained.

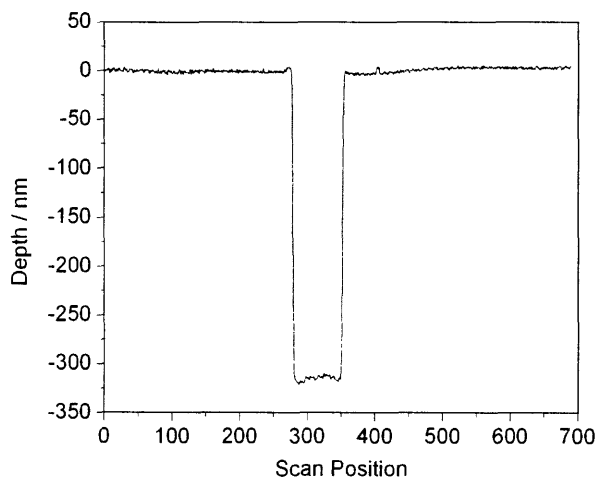


Figure 2.10. The surface profilometer trace for the sample whose ellipsometer data is shown above. The film thickness is $d = 318$ nm.

Table 2.1. Profilometry and Single Wavelength Ellipsometry Data for C152 Samples

200 °C, 3000 RPM Annealing time (min)	[C152] _{film} (M)	Profilometry thickness (d, nm)	Single $\lambda = 830$ nm Ellipsometry (d, nm)	Single $\lambda = 830$ nm Ellipsometry (n)
1	0.0775	246.7	257	1.575
5	0.0897	233.6	245	1.588
15	0.0925	228.2	238	1.611

Profilometry is a less sophisticated technique, where a tip examines the film surface and the resulting trace depicts the macroscopic surface morphology. The profilometry film thickness plot corresponding to the above ellipsometry measurement is shown in Figure 2.10. A $d = 318$ nm is measured and is in good agreement with the $d = 349$ nm measured by spectroscopic ellipsometry.

The thickness of the films can be tuned by controlling the reaction time for the acid-catalyzed cross-linking of the precursors and the spin coating rate. For example, spin coating films at 2000 RPM resulted in films 100 nm thicker than those spun at 3000 RPM. Spin coating rates of 4000-5000 RPM yielded films that were visibly rough and not homogeneous at the surface. The annealing temperature was increased from 150 °C to 200 °C to ensure effective curing of the titania in the films. Films annealed at 200 °C typically generated films with a refractive index of ~ 1.6 . The annealing time also had no profound effect on the thickness of the films and the refractive index, however it appeared that with increasing curing time, the effective concentration of C152 was augmented. Table 2.1 details film characteristics for a series of C152-doped films of the same initial solution concentration. An exhaustive study of film compositions showed that a 2:1 [Si]/[Ti] oxide composition to possess ideal properties for waveguiding.

From eq. (2.8), the minimum cut-off thicknesses (with $\lambda = 600$ nm) for a $n = 1.6$ film sandwiched between $n_{\text{air}} = 1.0$ and $n_{\text{substrate}} = 1.5$, is calculated to be 190 nm ($m = 0$) and 730 nm ($m = 1$). We see that for the films prepared here, a single mode will propagate through the slab waveguide. More generally, we find that the 2:1 [Si]/[Ti] films produced from our synthesis possess $d = 250 - 400$ nm, and thus will routinely support a single propagating mode.

2.2.3 Mesoporous Silica Cladding Layer

Maximal refractive index mismatch between the thin film and glass substrate was attempted by synthesizing a mesoporous silica cladding layer of refractive index values $n \sim 1.2$.⁴⁴ As demonstrated by Stucky and co-workers, well-ordered mesostructured silica films can be prepared by employing a triblock copolymer, poly(ethylene oxide)-poly(propylene oxide)-poly(ethylene oxide) (PEO-PPO-PEO).^{45,46} The use of a copolymer directing agent controls mesophase ordering and macroscopic morphology adopted by the silica. Because mesostructured silica materials are generally produced under nonequilibrium conditions, similar to those used to synthesize our $\text{SiO}_2/\text{TiO}_2$ films, the synthesis of mesoporous silica cladding layers on the slab waveguide was attempted.

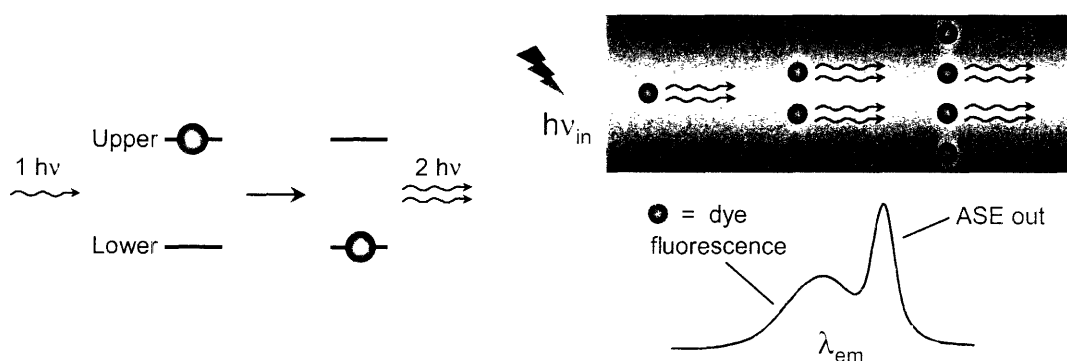
Unfortunately, the synthesis of smooth films by “controlled” volume fractions of material proved to be unsuccessful because of rough film morphologies. This was initially presumed to be due to the presence of remaining block copolymer within the film that was not fully decomposed and desorbed at the curing temperature of 150 °C. Desorption of the polymer occurs at 190 °C;⁴⁷ the existence of P123, which was likely present in the previous samples, was eliminated by curing the subsequent films at 195 °C for 15 min. The annealed samples appeared smoother, but the strong dependence of the surface morphology on the extent of Si hydrolysis makes this a difficult reaction to tune. Complete homogeneity of the silica aqueous mixture is necessary, but the presence of hydrophobic, non-hydrolyzed silicon alkoxides or 3D Si–O–Si networks (formed by extended cross-linking) disrupts ordering of the SiO_2 by P123.

For the sake of completeness, the optical characteristics of the films were defined. The calculated refractive index, as determined from single wavelength ellipsometry, was $n \sim 1.45 - 1.58$, far from the expected $n = 1.2$. For a sample spun at 3000 RPM, an average film thickness of 182.4 nm was obtained, with $n = 1.585$.

2.2.4 Optical Waveguiding of the Thin Films

The quality of the waveguide properties is demonstrated by the occurrence of amplified stimulated emission (ASE) from the excited states of the incorporated chromophore, R6G. For stimulated processes such as absorption and stimulated emission that occur at discrete states, the energy (and therefore frequency) of the light must correspond exactly to that of the energy difference between the two energy states. As shown in Scheme 2.2, stimulated emission results in the release of an additional photon into the same mode as the initial photon (at exactly the same energy (frequency), direction and polarization).² These two photons can each, in turn, stimulate the emission of two other photons, preserve these properties, and result in coherent light amplification. Because stimulated emission occurs when the photon energy is nearly equal to the atomic transition, ΔE , the process is restricted to a band of frequencies determined by the atomic linewidth.

Initial optical experiments with C152-doped films did not result in waveguide amplification, and only broad fluorescence was observed by excitation with $\lambda = 400$ nm. Dyes can undergo two major types of intermolecular photochemical reactions, oxidation and dimerization reactions, that will deactivate the radiative pathways. Thermal degradation pathways are also common for coumarins, where high optical pump power can cause thermal oxidation. Therefore, the next generation of prototypical film optical experiments relied on the



Scheme 2.2. (left) A molecule is excited to an upper energy level, and upon relaxation to a lower level, two photons are emitted. (right) Schematic of dye molecules incorporated into a thin film, and of the resulting ASE from the dye's broad fluorescence.

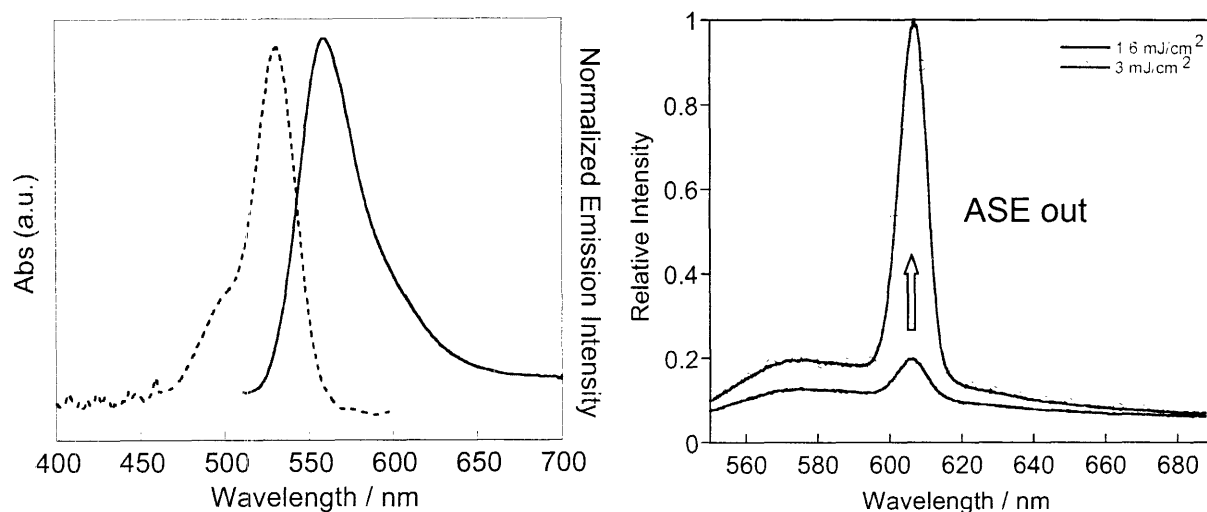


Figure 2.11. (left) Solution UV-vis spectrum (dashed) and steady-state fluorescence spectrum (solid) of R6G dye in ethanol, $\lambda_{\text{abs}} = 530$ nm and $\lambda_{\text{ems}} = 570$ nm. (right) Fluorescence spectra of a 2:1 [Si]/[Ti] film with R6G ($[\text{R6G}]_{\text{film}} \sim 0.095$ M). At low pump power, the beginnings of ASE is observed; an increase to 3 mJ cm^{-2} Nd:YAG excitation resulted in a pronounced narrowing and increase of the fluorescence.

laser dye Rhodamine 6G (R6G) because of its exemplary lasing efficiency,⁴⁸ small absorption cross-section at UV wavelengths and photostability when pumped with Nd:YAG lasers ($\lambda_{\text{exc}} = 532$ nm). With an emission maximum close to 570 nm, R6G exhibits a broad fluorescence and an extinction coefficient ϵ of $\sim 10^4 \text{ L mol}^{-1} \text{ cm}^{-1}$.⁴⁹ The concentration of R6G in the thin film state was determined to be ~ 0.095 M for a typical sample from solid-state UV-vis measurements.

ASE is established by the results shown in Figure 2.11. At very low pump power, only a broad fluorescence of incoherent emission centered at ~ 570 nm is detected from the 2:1 [Si]/[Ti] films. When the film is pumped at 8 mW (1.6 mJ cm^{-2}), a narrower band fluorescence is observed that is characteristic of ASE. With increasing pump power of 15 mW (3 mJ cm^{-2}), an exponential increase in gain and spectral narrowing of the guided ASE is observed. The narrow ASE linewidth (FWHM = 10 nm) is due to the finite linewidth of the gain function. It should be noted that only a small fraction of the pump photons are absorbed by the film itself due to the transverse pumping conditions, but there is a distinct red-shift of the λ_{max} for ASE relative to the dye's broad fluorescence which is attributed to self absorption of the film (overlap of the short wavelength region of the dye emission with the absorption band).

2.2.5 Distributed Feedback (DFB) Grating Fabrication

Implementation of second order DFB grating architectures to the synthesized films enables narrowing of the amplified stimulated emission (ASE) linewidth. Oscillation occurs in a DFB grating of period (Λ) at the Bragg wavelength (λ_B) that satisfies the condition in eq. (2.9). The periods of the master gratings, listed in Table 2.2, were fabricated for second order ($m = 2$) emitting structures and matched specifically to the emission wavelengths of the chromophores. As it is technically difficult to produce grating structures with periodicities $\Lambda < 300$ nm, chromophores that emit at higher energies, like coumarin dyes, were not incorporated into these structures. Rhodamine 6G (R6G) in the thin film state has an emission maximum approximately at $\lambda_{\max} = 580$ nm; the ASE demonstrated for R6G films exhibits $\lambda_{\max} = 610$ nm. For second order DFB SiO₂ / TiO₂ films with $n \sim 1.6 - 1.7$, the grating period can range from $\Lambda = 360 - 382$ nm, therefore two master gratings of $\Lambda = 360$ and 385 nm were implemented.

Soft lithography techniques were employed to emboss the SiO₂ / TiO₂ films with the DFB grating pattern. The master DFB gratings were fabricated on a silicon wafer with 300 – 500 nm pitches by using reactive-ion etch and interference lithography.⁵⁰ The quality of the master gratings were verified by high resolution Scanning Electron Microscopy (SEM), and images of a representative grating along with the removed photoresist are shown in Figure 2.12. The master gratings with small Λ are difficult and expensive to fabricate, and therefore they are preserved by pattern transfer to a poly(dimethyl)siloxane (PDMS) monolith. The troughs of the grating are only 50 nm deep and the shallow wells have made imprinting of the films difficult. Freshly spin-cast films are immediately pressed with the PDMS stamp at high temperatures, and the glassing

Table 2.2. DFB gratings specific for different waveguide media.

Λ (nm)	λ (nm)	Waveguide medium
280	450	SiO ₂ /TiO ₂ /coumarin dye
315	560	CdSe nanocrystals
333	600	CdSe nanocrystals
360	590	SiO ₂ /TiO ₂ /R6G dye

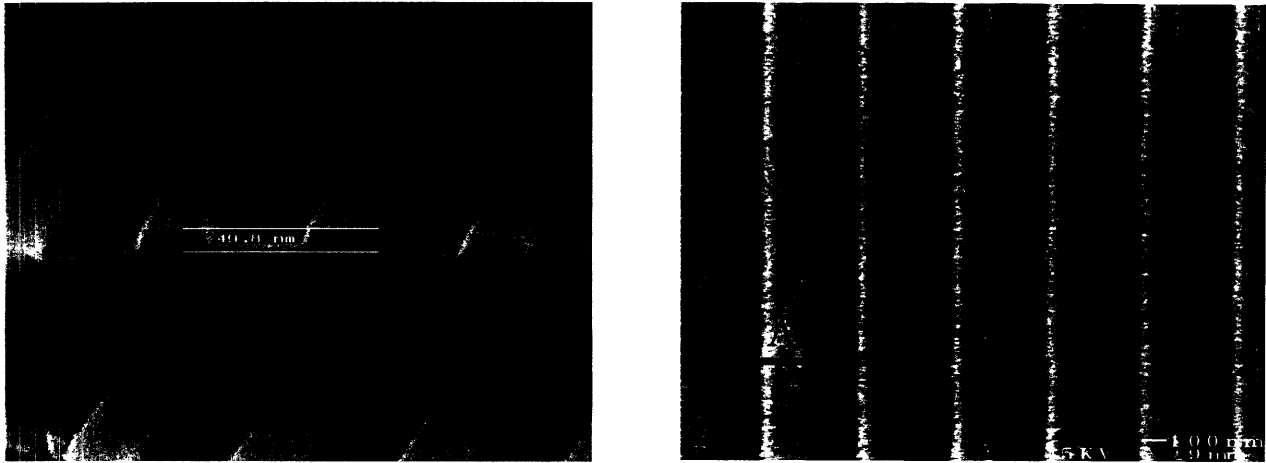
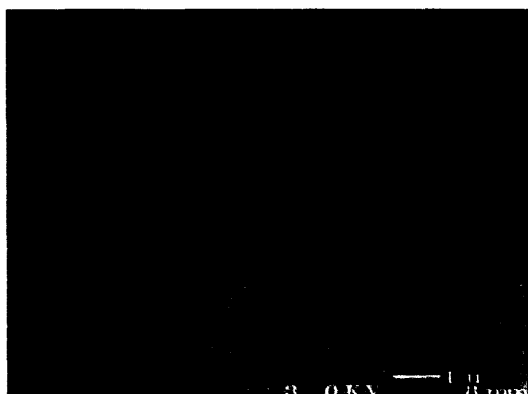


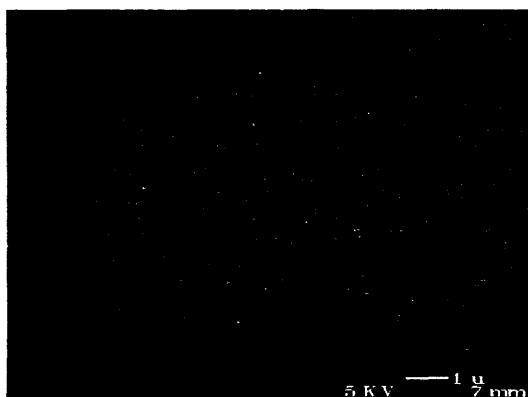
Figure 2.12. (left) SEM micrograph of the removed photoresist from the master grating indicating the 50 nm depth of the troughs. (right) Top-view SEM micrograph of Si master grating with $\Lambda = 360$ nm.

of the thin film can interfere with successful pattern transfer. SEM images of initial attempts indicated that the imprinting was slight, and modifications of the annealing temperature and length of PDMS embossment time were investigated.

A comparison of a room temperature stamped/cured sample and a room temperature stamped/high temperature cured sample is shown in the SEM micrographs of Figure 2.13. The overnight stamping of the 2:1 $\text{SiO}_2 / \text{TiO}_2$ films overnight with curing at room temperature resulted in an overall distribution of the grating pattern (Figure 2.13a). This was further confirmed with atomic force profilometry (AFP), similar to atomic force microscopy (AFM), which was conducted on room temperature stamping and cured samples. A representative trace is shown in Figure 2.14. Both the contact and the surface sampling mode, which is equivalent to the AFM tapping mode with no lateral motion, indicated that a grating impression was present on the films. However, the contact mode profile of a $6 \mu\text{m} \times 6 \mu\text{m}$ area showed that the embossment was uneven in distribution and the peak to trough height difference of the grating was measured to be 1.13 nm. The shallow grating depth can be attributed to artifacts from the tip pendulum



(a)



(b)

Figure 2.13. Scanning electron micrographs of stamped $\text{SiO}_2 / \text{TiO}_2$ films: (a) Room temperature cured film with $\Lambda = 360$ nm (3.0 kV, WD = 8 mm), (b) Room temperature stamped and cured at 150 °C for 2 min; $\Lambda = 360$ nm (5.0 kV, WD = 7 mm, 1° tilt).

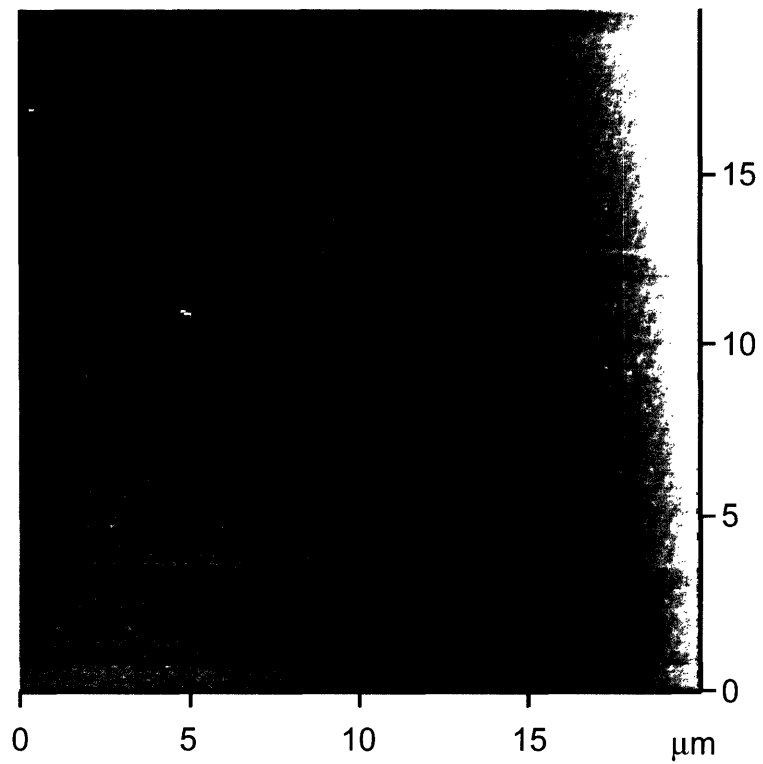


Figure 2.14. Atomic force profilometry (AFP) scan of a room temperature stamped film with $\Lambda = 385$ nm.

motion. Analysis of the surface sampling (tapping) mode profiles of the same sample resulted in an average grating depth of 10.23 nm, as shown in Figure 2.15.

Optimized stamping was obtained ultimately with films of varying $\text{Si}(\text{OEt})_4 / \text{Ti}(\text{OBu})_4$ concentrations. A representative scanning electron micrograph is shown in Figure 2.16. In the previous reactions, the $\text{Ti}(\text{OEt})_4$ precursor produced 1:1 condensation products with $\text{Si}(\text{OEt})_4$ because the homocondensation of silicates is slower than the heterocondensation with titania. The butoxide functionality of the $\text{Ti}(\text{OBu})_4$ precursor should slow down the rate of hydrolysis and the overall kinetics of the sol-gel reaction. A summary of the profilometry and spectroscopic ellipsometry characterization of these films with varying concentrations of [Ti] is shown in Table 2.3. With the increase in titania concentration, a large refractive index is obtained (similar to observations of previous films).

Table 2.3. Profilometry and Spectroscopic Ellipsometry Data for $\text{Si}(\text{OEt})_4 / \text{Ti}(\text{OBu})_4$ Films

195 °C for 2 min, 3000 RPM [Si] : [Ti]	Profilometry thickness (d, nm)	Spectroscopic Ellipsometry (d, nm)	Spectroscopic Ellipsometry (n)
2 : 1	301.4	340 ± 2	1.58
1.72 : 1	222.6	252 ± 1	1.70
only [Ti]	229.9	256 ± 1	1.93

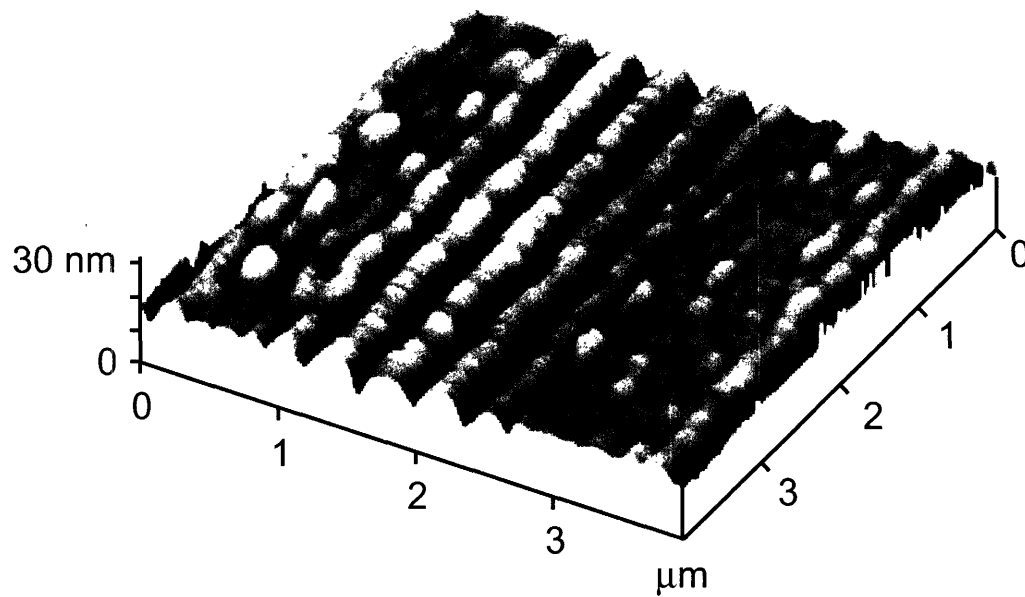
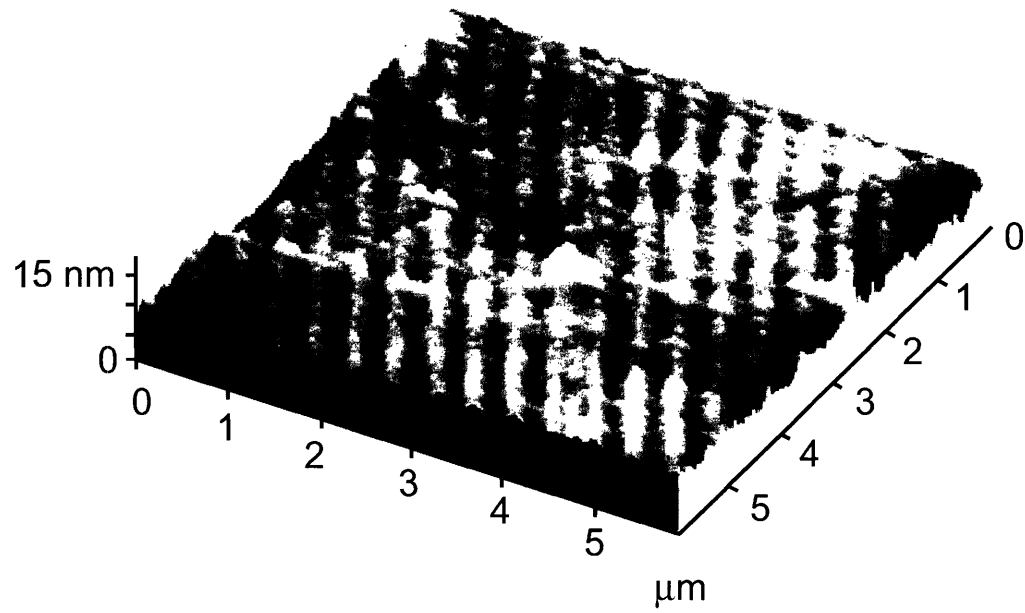


Figure 2.15. AFP profile (top = contact mode) of a room temperature stamped film. Approximate height difference between grating peak and trough was found to be 1.13 nm; (bottom = surface sampling / tapping mode) AFP of the same sample with 10.23 nm peak to trough distance.

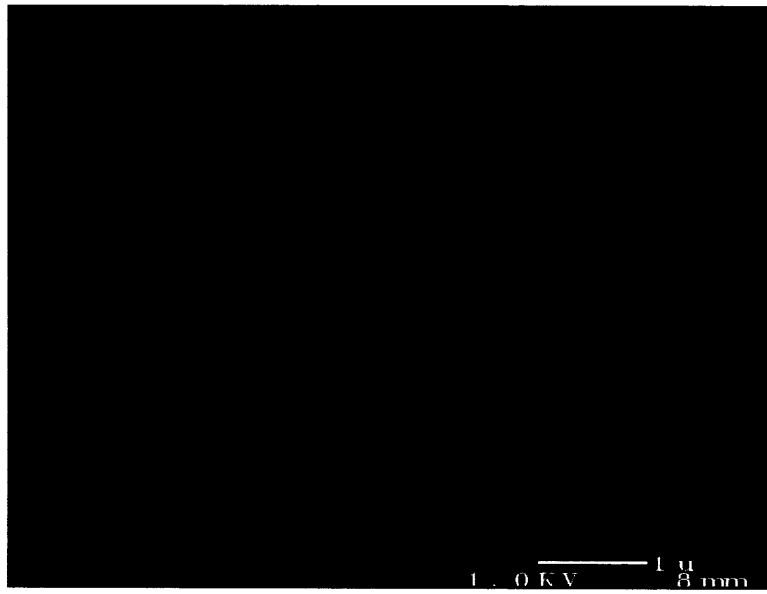


Figure 2.16. SEM image of a [Ti] film stamped at 195 °C (1 kV, WD = 8 mm).

2.2.6 Optical Characterization of DFBs

Rhodamine 6G doped DFB samples with $\Lambda = 360$ nm were optically characterized with the same detection setup used for the slab waveguides except the detector is now monitoring emission off the front face of the cavity. Excitation with the 532 nm radiation of a Nd:YAG laser resulted in stimulated emission. However, the $\text{Si}(\text{OEt})_4 / \text{Ti}(\text{OEt})_4$ films exhibited emission with a full-width-half-maximum (FWHM) of 12 nm and a quality (Q) factor of 50; representative spectra of these films are shown in Figure 2.17. The Q-factor of a laser cavity is calculated as the ratio of λ_L / FWHM .⁵¹ These are not high quality devices and that is attributed to the poor stamping of the films with the PDMS templates.

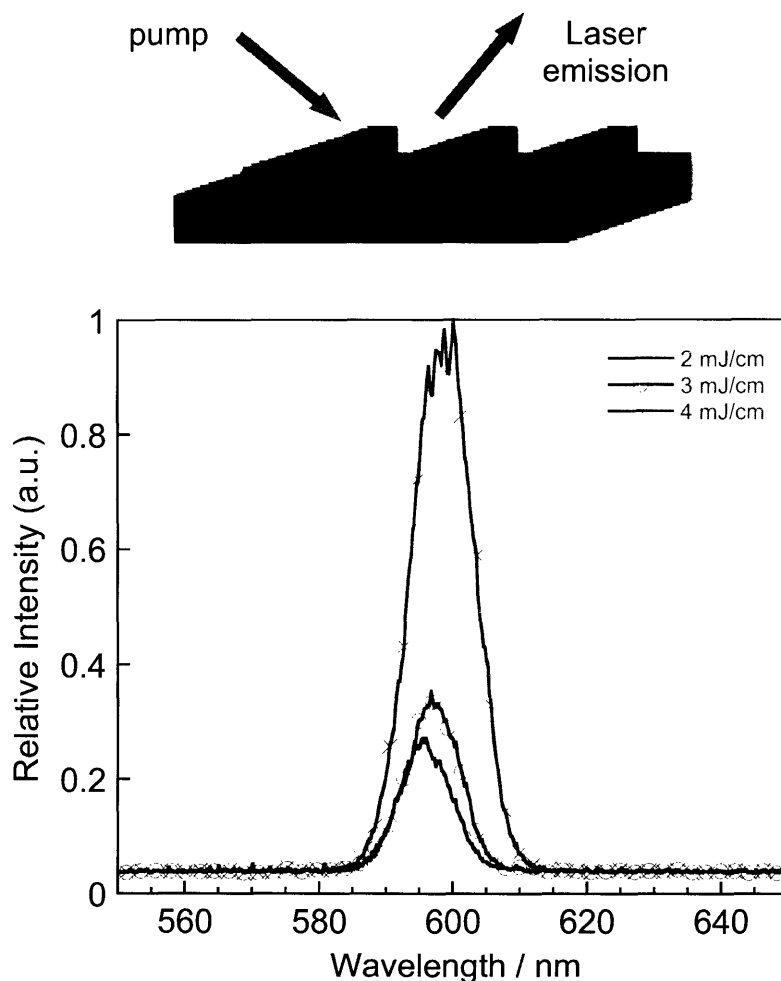


Figure 2.17. Emission observed from 2:1 $\text{Si}(\text{OEt})_4 / \text{Ti}(\text{OEt})_4$ films with $\Lambda = 360$ nm upon excitation with $\lambda = 532$ nm.

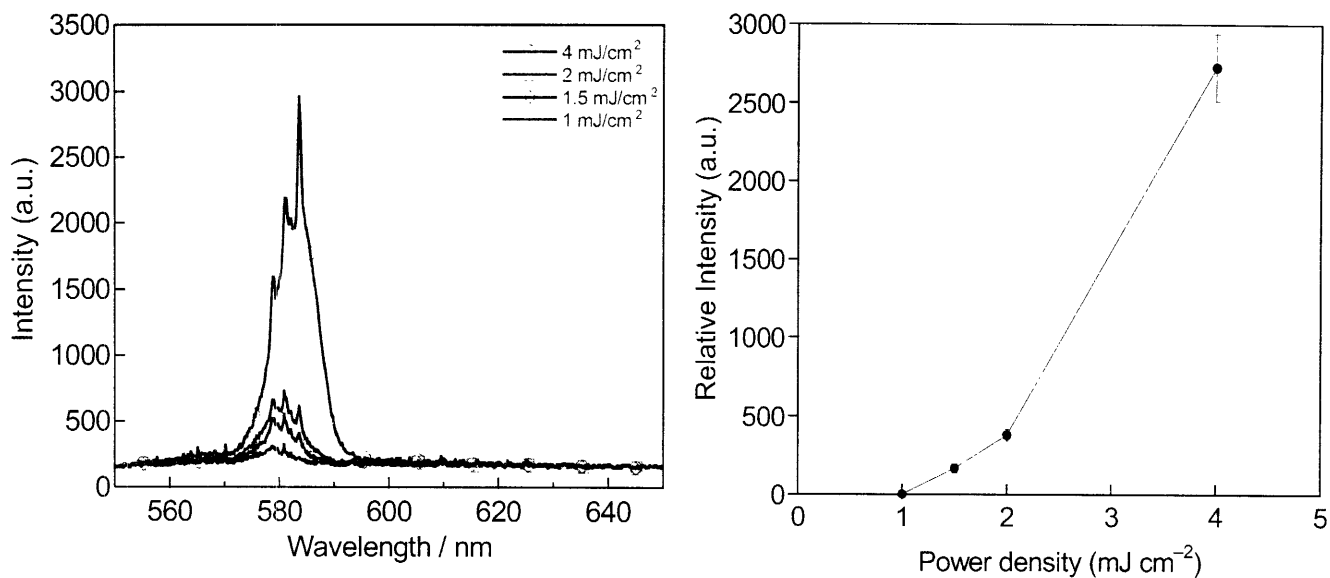


Figure 2.18. (left) Power dependent lasing emission observed from a 2:1 $\text{Si}(\text{OEt})_4 / \text{Ti}(\text{OEt})_4$ film with $\Lambda = 385$ nm upon excitation with $\lambda = 532$ nm. (right) Plot of relative intensity as a function of the power density.

New DFB films of R6G incorporated 2:1 $\text{Si}(\text{OEt})_4 / \text{Ti}(\text{OEt})_4$ were prepared in attempts to optimize the PDMS stamping technique. Emission off the front face of the second order emitting DFB was detected and the power dependence spectra are shown in Figure 2.18. With 5 mW (1 mJ cm^{-2}) excitation, only broad dye fluorescence is observed. Doubling the pump power to 10 mW (2 mJ cm^{-2}), a narrowing of the fluorescence is observed with several modes of the DFB. When the film is pumped at 20 mW (4 mJ cm^{-2}), a non-linear increase in intensity of one of the modes is evident. The presence of several modes can be attributed to the discrepancies in grating period distribution over the 1 cm length of the laser excitation beam. Stamping of $\text{Si}(\text{OEt})_4 / \text{Ti}(\text{OEt})_4$ films resulted in fewer modes, and the laser emission spectrum of the pure [Ti] is shown in Figure 2.19. Lasing emission is observed at 586 nm with a FWHM = 2.4 nm and a Q-factor of ~ 245 nm.

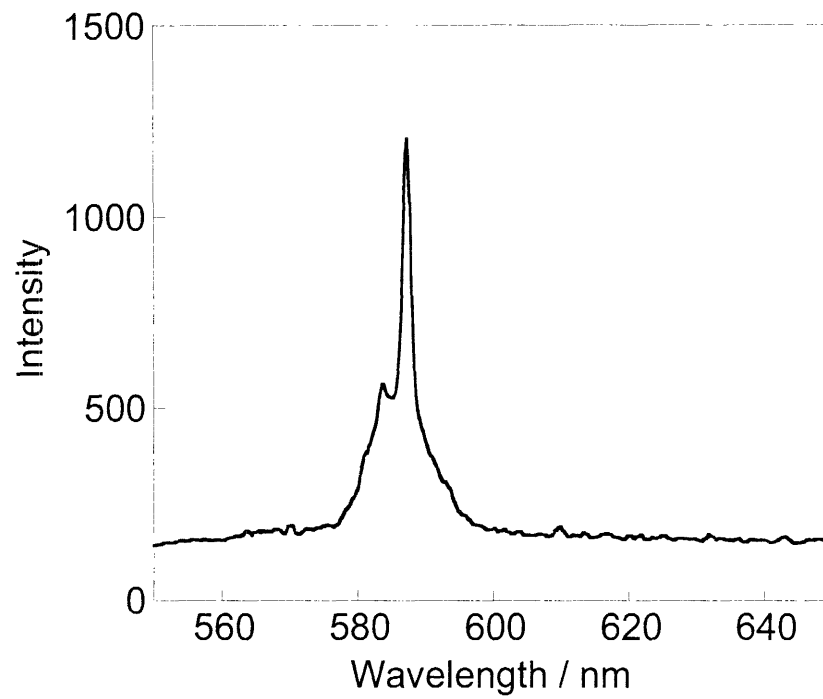


Figure 2.19. Lasing emission observed from a $\text{Ti}(\text{OBu})_4$ film with $\Lambda = 385$ nm upon excitation with $\lambda = 532$ nm.

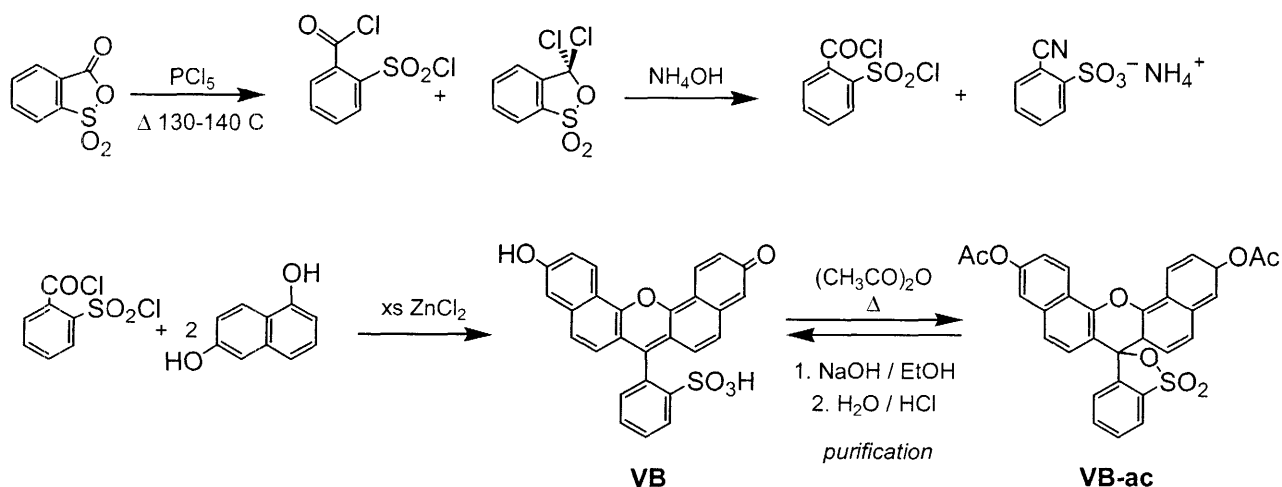
2.2.7 Vita Blue Dye Inclusion

The stamping technique was optimized for the DFB fabrication process, and the optical detection of laser emission from Rhodamine 6G was achieved. To transition these devices for the ultimate goal of chemical sensing, a new chromophore must be incorporated into the matrices to test its general application. A proof-of-concept experiment is to incorporate a laser dye that shifts its absorbance maximum away from the excitation wavelength ($\lambda_{\text{exc}} = 532 \text{ nm}$) upon a chemical reaction. The DFB no longer absorbs the pump beam and the lasing capabilities of the device are presumably deactivated, as shown in Figure 2.6.

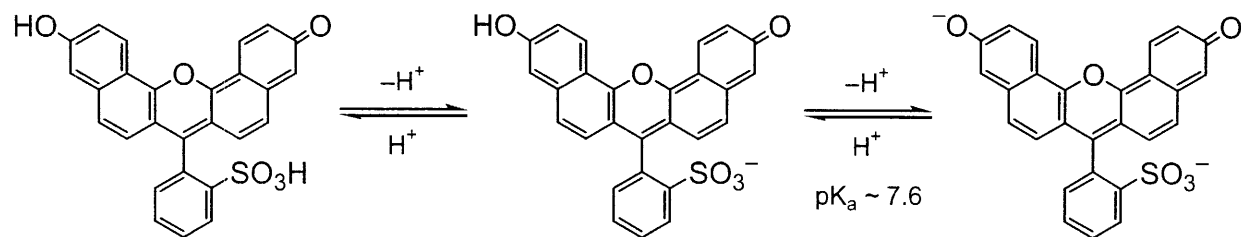
A prime example of such a chromophore is a pH indicator, where deprotonation/protonation events alter the spectroscopic properties of the dye. Since we are using green excitation light, there are few pH probes that absorb that far red in the visible region. One literature example of an intracellular pH probe was found,⁵² and the Vita Blue (VB) dye was synthesized following Scheme 2.3. The low-yielding synthesis of the dye, even in larger scale syntheses, is due to the deactivating character of the sulfonic acid groups in Friedel-Crafts acylations.⁵² This was a time-consuming disadvantage that was further exemplified with the large concentrations needed to infuse into the thin films.

Vita Blue dye has two distinct deprotonated states, shown in Scheme 2.4, that are similar

Scheme 2.3.



Scheme 2.4.



to fluorescein. Both the monoanionic and dianionic forms of the sulfone naphthofluorescein derivative are fluorescent,⁵² however the contribution of the monoanionic state is minimal. Titration studies were monitored by both absorption and emission spectroscopies. As seen in Figure 2.20, the absorption maximum red-shifts upon deprotonation ($pK_a \sim 7.6$),⁵² with a concomitant increase in emission intensity at $\lambda_{\text{ems}} = 660 \text{ nm}$. At high pH, the absorbance maximum of the dye shifts towards the laser excitation wavelength of 532 nm. Therefore, the titration measurements can be carried out in a flow cell with the DFBs and only at slightly basic pH will the lasing “turn-on”. Initial optical characterization of these films did not even result in the observation of amplified stimulated emission. VB has a low quantum yield ($\phi = 0.15$) relative to fluorescein⁵² and to that of R6G ($\phi = 0.95$),⁵³ which indicates its lower photo-efficiency in our thin film DFBs. The acid-base properties of the pH dye are also easily affected by the microenvironment, which is largely dependent on the concentration loading of the dye. With larger concentrations, even in solution, the VB dye is noted to dimerize and possibly form excimers. In addition, the local acidity of the matrix pores (due to the acid catalyzed hydrolysis of the sol-gel) may affect the absorption spectrum of the dye.

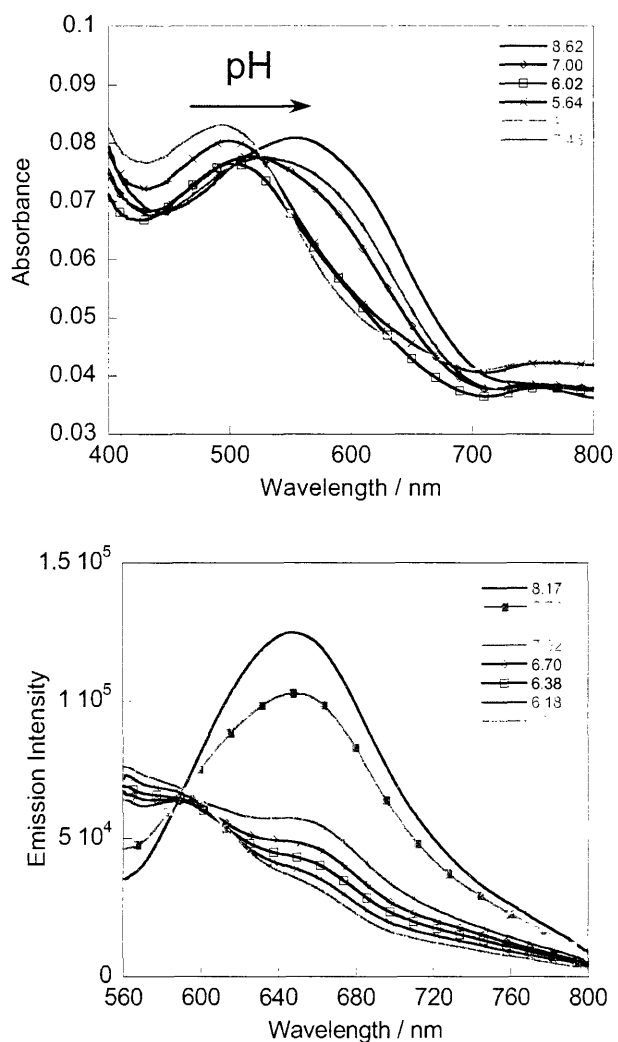


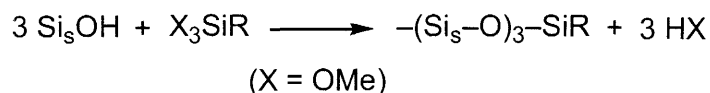
Figure 2.20. Titration of VB dye monitored by (top) UV-vis and (bottom) emission ($\lambda_{\text{exc}} = 540 \text{ nm}$) spectroscopies. A red-shift in absorbance and increase in fluorescence results from an increase in pH.

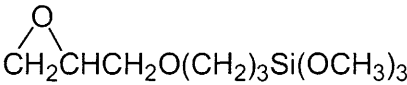
2.2.8 Covalent Attachment of Receptor Sites

The implementation of a signaling transduction mechanism for sensing into these laser platforms will require the thin films to be responsive and permeable to analyte. Chemical modification of these inorganic films is readily achievable and allows for the covalent attachment of reporter molecules of the 3R sensing scheme. The tunability of the porosity of these mixed silicate-titania films can also be exploited for the adsorbing of analyte into the matrix, however the challenge with this method is controlling the loading concentration of the chromophores. In addition to the development of highly sensitive detection of molecules at very low concentrations, the challenge of forthcoming sensing research is the design of portable and cost-effective devices. Although binding reversibility of analyte to the chemosensor recognition site has previously been emphasized, the construction of inexpensive sensing devices that can be multiplexed and widely distributed is also an acceptable alternative.

Covalent immobilization of the receptor sites onto the waveguide surface increases the overall stability and is preferred to electrostatic binding of charged groups. The receptor sites are commonly incorporated in various ways: (1) immobilization of the polymer/sol-gel onto a surface with the receptor incorporated in the waveguide by physical, physiochemical, or electrostatic binding methods; (2) the receptor is covalently grafted onto the polymer/sol-gel surface. With the latter case being the most stable, it is important to maintain the functionality of the receptor site upon binding, thus increasing the complexity of the chemistry.

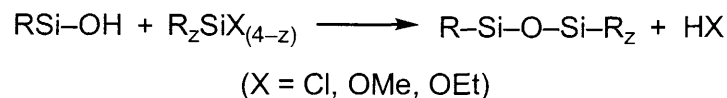
The advantage of the sol-gel thin films is the facility of covalent attachment of receptor sites to the surfaces. A whole host of modification chemistry exists for hydroxyl-terminated Si surfaces⁴⁰ and the representative silylation reaction and organic coupling agents are outlined in Scheme 2.5. Silanization is an optimal surface immobilization reaction, where the hydrogen atom bound to the hetero-atom of R-SiOH is substituted with a silyl group. The simplified reaction is shown in Scheme 2.6, where X is a chlorine or a hydrolyzable group such as a methoxy or ethoxy group, typically in an organosilane $R_zSiX_{(4-z)}$. The functional group R_z can be

Scheme 2.5.

Organofunctional Groups	Coupling Agents
vinyl	$\text{CH}_2=\text{CHSi}(\text{OCH}_3)_3$
chloropropyl	$\text{Cl}(\text{CH}_2)_3\text{Si}(\text{OCH}_3)_3$
epoxy	
methacrylate	$\text{CH}_2=\text{C}-\text{C}(\text{CH}_3)\text{OO}(\text{CH}_2)_3\text{Si}(\text{OCH}_3)_3$
primary amine	$\text{H}_2\text{N}(\text{CH}_2)_3\text{Si}(\text{OC}_2\text{H}_5)_3$
methyl	$\text{CH}_3\text{Si}(\text{OCH}_3)_3$

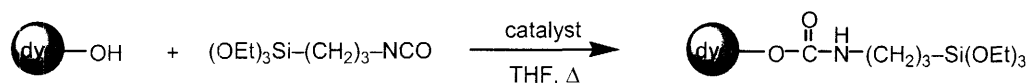
an acrylic compound for film polymerization, or an epoxy function oxidized in aldehyde for antibody covalent grafting by amino groups of the protein in a Schiff base reaction. Dimethylamine silanes are more reactive compared to chlorosilanes and alkoxy silanes, and principal silanization agents include: aminopropyltriethoxysilane (APTES), dimethyldichlorosilane and octadecyltriethoxysilane. Other techniques include activating the surfaces by coupling to an amino group, which can then be attached to a receptor site with a carboxylic acid functionality with either *N*-hydroxysuccinimide (NHS) or dicyclohexyl carbodiimide (DCC) as a coupling agent.

One can envision the patterning of the silicate surfaces with various receptors specific for different analytes that absorb at different wavelengths. An array of chemo- and bio-sensors can be built on DFB laser cavities by incorporating reporter chromophores of varying emitting wavelengths into specific areas of the cavity embossed with the respective grating period Λ . In

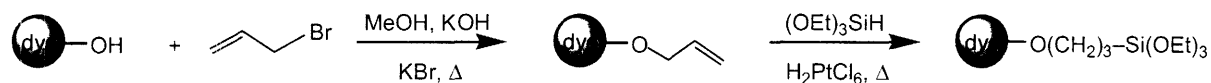
Scheme 2.6.

Scheme 2.7.

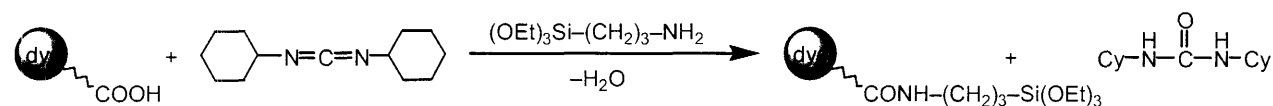
Urethane linkage



Propoxy linkage



Silylation via dehydrative coupling

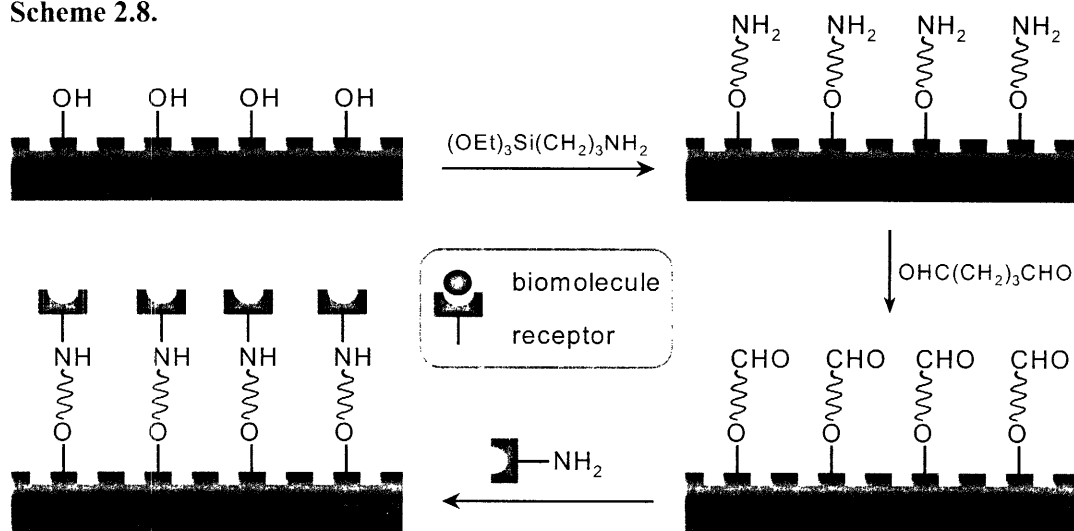


order to move to the multiplexing of these high gain sensors, the covalent attachment chemistry and the dependence on the concentration of receptors must be investigated.

To date, three methods of coupling chemistry have been explored as routes for attaching dye chromophores to the silicate-based matrix synthesized in this Chapter. In following Scheme 2.7, the dye used was 7-hydroxy-4-methylcoumarin (Coumarin 4) with its hydroxyl functionality appropriate for the coupling chemistry with the propoxy and urethane linkers.^{54,55} For the propoxy linker chemistry, the intermediate allyloxy coumarin was crystallized as white needles and characterized by ¹H NMR. It was then treated with triethoxysilane in the presence of H₂PtCl₆ catalyst, and it took several days to go to completion. The use of the olefin hydrosilylation catalyst H₂PtCl₆ resulted in the precipitation of Pt(0) and the need for oxygen as a co-catalyst may have hindered the overall synthesis of the propoxy-linked coumarin.

The synthesis for the urethane linkage was monitored by FTIR and ¹H NMR. The disappearance of the isocyanate peak (2290 cm⁻¹) and the increase of the urethane peak (1765 cm⁻¹) were monitored by FTIR (see Appendix). Isolation of the urethane-linked coumarin allowed characterization by ¹H NMR, UV-vis and emission spectroscopies. The solution absorbance showed high energy dye transitions, and excitation at 375 nm resulted in

Scheme 2.8.



fluorescence at $\lambda_{\text{max}} = 450 \text{ nm}$; this is consistent with the spectroscopic characterization of Coumarin 4.⁵⁶ Dehydrative coupling of a carboxylic acid group on a Rhodamine 610 dye and APTES with the DCC coupling agent was also attempted. The Sulforhodamine B dye with a sulfonyl chloride moiety was also coupled to APTES in pyridine. These preliminary reactions are all viable methods for covalently linking a dye chromophore and relevant receptors with similar functionalities onto the $\text{SiO}_2 / \text{TiO}_2$ film surfaces.

Upon successful coupling, the silanes can be used in the hydrolysis and condensation reactions of Section 2.2.1. The concentrations of the dye-attached silane relative to the silica and titania precursors must be worked out in order to prepare optimized waveguiding samples. Ultimately, biosensing can be performed with the $\text{SiO}_2 / \text{TiO}_2$ DFBs by surface modification of a biomolecule such as biotin, and subsequently flowing through various concentrations of the glycoprotein avidin. APTES can also be used in the silanization of the surface with pendant amino groups, and upon reaction with glutaraldehyde an active aldehyde is attached at the surface, as shown in Scheme 2.8. Finally, the aldehyde can react with a primary amine of a protein to form the final -CH=N-protein .⁵⁷ Optical performance of the modified waveguides must be assessed and once they are optimized, the receptor-functionalized DFBs will be generalized for highly specific and sensitive non-linear biosensing applications.

2.3 Conclusions

The synthesis of thin films that have the proper physical and optical requirements for DFB implementation has been achieved. Exhaustive compositional studies of the concentration dependent synthesis of inorganic SiO₂/ TiO₂ matrices for waveguiding were conducted. We find that 2:1 SiO₂/TiO₂ matrix composition with dye loadings of $\sim 10^{-2}$ M possess the desired properties for optical waveguiding:

- A mean surface roughness of $\leq \pm 0.500$ nm as determined by AFM is obtained.
- A refractive index of $n \sim 1.60$ is deduced from spectroscopic ellipsometry measurements.
- And a film thickness that falls within the range of the calculated minimum cut-off thicknesses that will support the m^{th} mode ($d = 250 - 400$ nm).

Optical characterization of these films indicated that they exhibit amplified stimulated emission properties, a necessary condition for DFB lasing to be achieved.

In addition, we optimized the stamping of the thin films with a PDMS rendering of the DFB grating. A narrowing of the stimulated emission modes off the front face of the second order emitting DFB structures was observed, with a FWHM of 2.4 nm and a Q-factor of 245. This is a relatively good quality laser device, considering the impregnated organic chromophore. Numerous attempts to incorporate pH sensitive dye Vita Blue into the DFBs did not result in a lasing cavity. These results indicated that the local environment was changing the spectroscopic properties of the dye, and more studies must be carried out to stabilize the organic chromophore; the low photoefficiency and stability of the dye may be circumvented by covalent attachment to the film. Future investigations of the SiO₂ / TiO₂ DFB cavities will require covalent modification of the surfaces to provide further stability to the receptor and reporter sites.

2.4 Experimental

2.4.1 General Methods

All synthetic manipulations were conducted under air and moisture-free conditions using standard Schlenk-line techniques or a nitrogen-filled glove box.

Spin casting was carried out on a Headway Research spin coater and cured on a Corning stirrer/hot plate, both located in the Bawendi Lab at MIT. Both the spin coater and the hot plate were housed in a small, portable glove box to control the local environment. Prior to spin casting, the box was purged with nitrogen until the humidity range was between 19 - 24%.

Surface profilometry was conducted on a Tencor P-10 (KLA-Tencor Corp.) instrument, with a 2.0 μm stylus tip. Single wavelength ellipsometry measurements with a Gaertner Scientific Three Wavelength/Variable Angle Ellipsometer were made on first generation samples. The Fink Lab at MIT generously allowed us to use their scanning wavelength SOPRA-GES 5 spectroscopic ellipsometer. FTIR reflectance measurements were carried out on Si substrate samples with a Nicolet Magna 860 spectrometer coupled with a Spectra Tech Nic Plan FTIR microscope. Absorbance measurements on thin film samples were carried out on a Cary 5E Dual Beam spectrophotometer. Steady state solution emission spectra were obtained (in a 1 cm pathlength quartz cuvette) from a custom-built Photon Technology Instruments fluorometer installed with a Hamamatsu R928 photomultiplier tube and a 150 W Xe excitation lamp. With the exception of our fluorometer and the spectroscopic ellipsometer, all the instruments are maintained in the Analysis Shared Experimental Facility at the MIT Center for Materials Science and Engineering (CMSE).

All NMR spectra were collected at the MIT Department of Chemistry Instrumentation Facility (DCIF) on a Varian Mercury 300 or Varian Unity 300 Spectrometer at 25 ± 2 °C. Chemical shifts are reported using the standard δ notation in ppm. ^1H NMR spectra were referenced to residual solvent peaks.

2.4.2 Materials

Laser dyes were obtained from Lambda Physik Inc. Solvents for syntheses were of reagent grade or better, and degassed prior to use. Water was OmniSolv (EMD Chemicals Inc.) grade and also degassed. Starting reagents were obtained from Aldrich Chemical Co., TCI America, and Strem Chemicals, and all materials were used as received. NMR solvents (Cambridge Isotope Laboratories) were either dried using appropriate agents or used as received in glass ampoules. Glass substrates were cut from 25 mm × 75 mm microscope slides (VWR) into approximately 1 cm × 0.25 cm pieces. Silicon substrates for profilometry, ellipsometry, AFM and FTIR measurements were cut from 4 inch p-type (B-doped) <1,0,0> wafers, with $\rho = 2 - 3.5 \Omega\cdot\text{cm}$ and 500 - 550 μm thickness (Silicon Quest, CA). Glass and silicon substrates were cleaned using Piranha solution (7:3 by vol. conc. $\text{H}_2\text{SO}_4 / \text{H}_2\text{O}_2$) and subsequently with the RCA SC-1 method (7:1:1 by vol. $\text{H}_2\text{O} / \text{H}_2\text{O}_2 / \text{NH}_4\text{OH}$).⁵⁸ They were then dried with a stream of clean, pressurized nitrogen.

2.4.3 Synthesis of $\text{SiO}_2/\text{TiO}_2$ Matrix

The sol-gel matrices were prepared by the acid-catalyzed partial hydrolysis of $\text{Si}(\text{OEt})_4$ (99.999%, Aldrich Chemical Co.) and $\text{Ti}(\text{OR})_4$ (R = Et; Strem Chemicals, PURATREM or R = Bu; TCI America) at various concentrations (1:1, 2:1, 1.72:1, 4:1, 1:2, 100% [Ti]). The two precursors were mixed under an inert nitrogen atmosphere (glove box conditions). The laser dye solution of degassed, anhydrous ethanol (0.02 M) was then introduced, followed by the dropwise addition of 0.2 mL 2 N HCl. Reactions were carried out at room temperature, under N_2 atmosphere, and allowed to react from 1 hr to overnight.

Thin films were prepared by syringing the sol through an Acrodisc syringe filter (13 mm with 0.2 μm HT Tuffryn membrane) onto substrate and spin coating at 2000 - 5000 RPM to give various thicknesses. The samples were subsequently cured at 150 - 200 °C for 2 min.

2.4.4 Preparation of PDMS Stamps

The DFB master gratings were fabricated in the labs of Prof. Henry Smith at the MIT Research Laboratory of Electronics (RLE) using the reactive-ion etch (RIE) method⁵⁹ on silicon wafers. The $\sim 1 \text{ cm}^2$ templates were evacuated inside a vacuum chamber for 20 and 2 min intervals, cycled twice, in the presence of tridecafluoro-1,1,2,2-tetrahydrooctyltrichlorosilane (United Chemical Technologies). Poly(dimethyl)siloxane (PDMS) stamps of these master templates were prepared using precursors obtained from Dow Corning Corp., where Sylgard 184 Silicone Elastomer base and Silicone Elastomer curing agent were mixed (10:1 ratio by weight) and degassed in a vacuum chamber for 1-2 hours. The mixture was then poured onto the master grating sample and allowed to cure for 2 days at room temperature, whereupon the PDMS was removed from the master grating and cut into re-usable stamps.

2.4.5 Preparation of DFB Samples

The thin films upon which the grating pattern is embossed are prepared as described in Chapter 2.4. The films are spin-cast at 3000 RPM for 1 min onto clean substrates at room temperature in a controlled environment (low humidity, N_2 purged). Freshly spun films were embossed with the PDMS stamps with the appropriate grating period. The films were then cured at high temperature on a heat plate at $200 \text{ }^\circ\text{C}$ for 2 min, with even weight distribution placed on the stamp. For room temperature stamped films, a heavier lead weight block was clamped securely over the freshly spun films and left to cure for two days before removing the PDMS stamp.

2.4.6 Characterization Techniques

2.4.6.1 Surface Profilometry

Surface profilometry measurements were performed on a thin film spin coated on Si substrates. A uniform scratch along the thin film surface was generated, and the film depth was

obtained with a 2.0 μm tapping tip. A thickness was obtained from an average of at least 3-5 separate measurements for each sample, upon leveling of the data.

2.4.6.2 Single Wavelength Ellipsometry

Single wavelength ellipsometry measurements were carried out on C152-doped samples, where excitation with an Ar laser ($\lambda = 488 \text{ nm}$), a HeNe laser ($\lambda = 633 \text{ nm}$), or a diode laser ($\lambda = 830 \text{ nm}$) was dependent on the absorbance of the films. The angle of incidence was at $\phi = 70^\circ$ and the polarizer angle was set at 45° . The default Si substrate n_s and k_s values are set by the MULTIFILM program, which used old retardation values from 1997 to generate Ψ and Δ parameters. New substrate parameters were subsequently generated with a reference sample for each excitation wavelength: ($\lambda = 488 \text{ nm}$; $n_s = 4.337$; $k_s = -0.081$), ($\lambda = 633 \text{ nm}$; $n_s = 3.850$; $k_s = -0.020$), and ($\lambda = 830 \text{ nm}$; $n_s = 3.659$; $k_s = -0.004$).

2.4.6.3 Spectroscopic Ellipsometry

The spectroscopic ellipsometer was scanned every 8 or 10 nm from $\lambda = 300 - 1800 \text{ nm}$, with the analyzer angle at 45° and the incident angle stepped every 3° from $72 - 78^\circ$. Integration time was set at 10 s or 20 s for more absorbing samples. The ellipsometric parameters were fit to a Levenberg-Marquardt regression algorithm function: $\cos(2\Psi)$ and $\sin(2\Psi)\cos(\delta)$, and in some cases, absorption corrections were necessary to obtain a satisfactory fit (SOPRA-Winelli V4.07). The regression analysis was performed using the Cauchy dispersion model, which yielded the film thickness and the Cauchy coefficients. The Cauchy parameters were interpolated from the data and the refractive indices and film thicknesses were then derived as a function of wavelength.

2.4.6.4 Atomic Force Microscopy

The surface morphology was determined by Atomic Force Microscopy (AFM) using a Nanoscope IIIa Scanned Probe Microscope housed at the CMSE. The mean surface roughness (rms) was determined from a roughness analysis and a plane curve correction routine.

2.4.6.5 Atomic Force Profilometry

Atomic force profilometry (AFP) was conducted on a pilot instrument, KLA Tencor Nanopics 2100, in both contact and surface sampling modes. Contact mode scans were conducted on a $6\ \mu\text{m} \times 6\ \mu\text{m}$ area with 512×512 pixels/line resolution and a 1.33 Hz scan speed, and are dependent on the tip motion (pendulum movements) throughout the measurement. Surface sampling mode, similar to tapping mode of AFM, gave more accurate grating depth measurements due to the lack of lateral motion of the tip as it traced the surface. Scans were carried out at 0.67 Hz with 512×512 pixels/line resolution. AFP measurements were conducted only on room temperature stamped and cured samples.

2.4.6.6 Scanning Electron Microscopy

Scanning Electron Microscopy (JEOL 6320FV Field-Emission High Resolution SEM) of the films on Si substrates determined the confirmation of successful pattern transfer. The SEM is maintained by the MIT CMSE Electron Microscopy Shared Experimental Facility. These samples were found to easily charge under the electron beam, and contamination from the sample was also observed at low voltages. Both backscattering and secondary electron setups were also used with the BSE and SEI detectors, respectively, in hopes of obtaining higher resolution images of the patterned thin films. Images of sufficient quality were eventually obtained with either objective aperture 2 or 3, an accelerating voltage of 1 kV - 2 kV, a working distance (WD) of 8mm, and a slight tilt of the sample ($3^\circ - 3.7^\circ$). The images were obtained by integration of 100 - 198 snapshots, followed by image processing with the 2D Average, Cube, and SQRT functions. The master gratings with $\Lambda = 360\ \text{nm}$ and $385\ \text{nm}$ were also examined using SEM, with an accelerating voltage of 5 kV, 8 mm WD, and no tilt angle.

2.4.7 Synthesis of Mesoporous Silica Layer

The incorporation of a cladding layer with a lower refractive index than substrate was attempted with the synthesis of a mesoporous silica layer ($n = 1.2$). The synthesis required using

Chapter 2

the (ethylene oxide)₂₀–(propylene oxide)₇₀–(ethylene oxide)₂₀ triblock copolymer series (Pluronic P123, BASF) as the structure-directing agent.⁴⁶ Using the pure tetraethyl orthosilicate precursor, 3.5 g (3.75 ml) of Si(OEt)₄ was hydrolyzed with 1.3 g H₂O (pH = 1.3, HCl, dropwise addition) under nitrogen for 2 hrs until the solution was homogeneous. P123 (1 g) was completely dissolved in 10 g anhydrous EtOH and added dropwise to the silica/water solution. The reaction was stirred under nitrogen and allowed to age at room temperature for two days to promote silica cross-linking.

Films were prepared by spin coating at 2000 - 3000 RPM onto glass substrates, and cured at 150 °C for 15 min. Subsequent syntheses shortened the room temperature aging of the silica/P123 mixture to 1 hr and curing of the films to 195 °C. Single wavelength ellipsometry measurements were made for these samples at $\lambda_{\text{exc}} = 633$ and 830 nm, and the calculated thicknesses and refractive indices were too varied to be accurate. However, they were not close to the expected value of 1.2, with refractive indices in the range of 1.45 - 1.55.

2.4.8 Optical measurements

Absorption spectra on thin films were obtained on a Cary 5E Dual Beam spectrophotometer, with the subtraction of reference spectra taken of glass substrates. A schematic of the optical detection setup is shown in Figure 2.21. Spectroscopic measurements involved excitation with a 50 Hz Nd:YAG laser (Continuum NY60) using the 532 nm second harmonic radiation which passed through a cylindrical lens to focus the beam to a stripe, and a dichroic filter to pass the appropriate wavelengths. A filter wheel was placed in the incident beam path to change the power of the excitation source. Samples were mounted in a cryostat (Janis) evacuated to 10^{-5} atm and cooled with liquid nitrogen down to 80 K. The cryostat was rotated to position the sample about $\sim 45^\circ$ to the incident beam to enable front-face detection of second order laser emission, and in the case of ASE measurements, the fiber optic/detector was placed $\sim 90^\circ$ to the sample surface. The emission from the sample was fed through a fiber optic

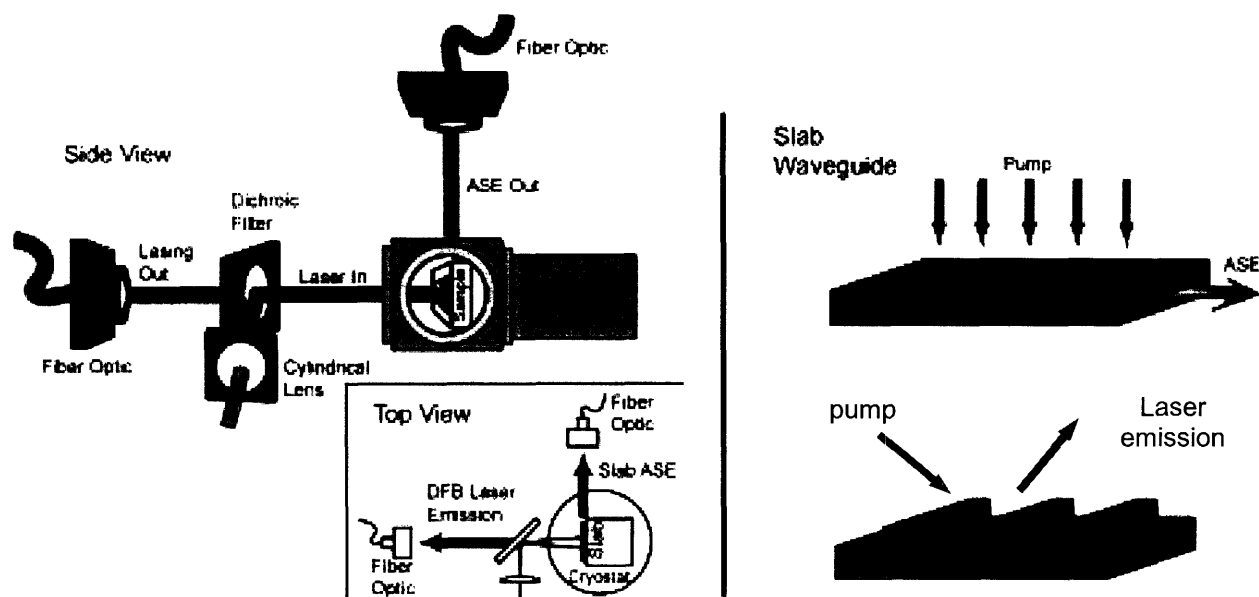


Figure 2.21. Schematic of the optical detection setup for a slab waveguide and for a DFB.

cable into a CCD spectrophotometer with an entrance aperture of 25 μm and 600 l/mm grating blazed at 500 nm (Ocean Optics HR 2000). Integration times for data acquisition were set to be 300 - 1000 ms. Power dependence measurements were obtained at the same location for the samples, and pump power readings were taken before and after each measurement.

2.4.9 Synthesis of Vita Blue (VB) Dye

The synthesis followed modified literature procedures.⁵² The starting material, 2-chlorosulfonyl benzoylchloride, was synthesized by refluxing 2-sulfobenzoic anhydride (15.35 g, 0.083 mol) and PCl_5 (32 g, 0.154 mol) under nitrogen. The evolution of HCl and OPCl_3 was observed, and the pale yellow solution was heated for 2.5 hrs. The hot solution was poured onto ice and extracted with the slow addition of 100 ml ether; it was slightly exothermic and was further quenched with the addition of more ice. Removal of the aqueous phase and drying the ethereal fraction overnight with MgSO_4 yielded a white solid.

All of the product from the above reaction was used without further purification, and was added to a round bottom with 1,6-dihydroxynaphthalene (8 g, 0.05 mol) and ZnCl_2 (3.5 g, 0.025

mol). The mixture was heated up to 90 - 95 °C and gas evolution was observed. A solution of NaOH (6 g in 100 ml water) was added and the reaction stirred for 15 min. The solid was filtered off and the dark green filtrate was acidified with concentrated HCl until neutralized. Now murky red-brown, the solution was filtered and the solid was dissolved in ethanol (150 ml). The ethanol was brought to a boil and subsequently cooled to 4 °C overnight. Dark red-brown solid was obtained and characterized by negative-ion ESI-MS (Applied Biosystems Mariner Mass Spectrometer) as the crude VB product.

The crude VB product was then converted to the diacetate (VB-ac) by dissolving the solid (0.096 g, 0.2 mmol) in acetic anhydride (30 ml) and refluxing for 4 hrs. The orange-brown solution was filtered hot and the acetic anhydride was removed by vacuum distillation. The brown solid was recrystallized with ether at 4 °C, and repeated multiple times to yield more product. Finally, VB-ac was dissolved into an ethanolic solution of NaOH, which instantly turned blue-green and solvent was stripped in vacuo. The pale green solid was dissolved in degassed water and concentrated HCl (~ 1 ml) was added dropwise until the solution turned purple with precipitate formation. The super fine magenta purple solid was then centrifuged to remove the supernatant and recrystallized by layering methanol and ether at 4 °C. After multiple recrystallizations, purple solid was obtained and characterized by ESI-MS to be the VB product. ESI-MS *m/z*: [M + H] 465.

2.4.10 Synthesis of Propoxy Coumarin Linkage

7-Hydroxycoumarin (1 g, 6 mmol) was added to a solution of KOH (0.36 g, 6 mmol) and KBr (0.038 g, 0.3 mmol) in methanol (45 ml). The reaction was heated to 40 °C for 20 min under nitrogen. Allyl bromide (0.61 ml, 7 mmol) was added dropwise, and the reaction was refluxed for 6 hrs. After cooling the almost colorless solution to room temperature and with the addition of water, white solid precipitated. The extraction of the product into diethyl ether and removal of solvent resulted in a white solid. Recrystallization from methanol at 4 °C yielded white needles of allyl coumarin, which were characterized by ¹H NMR spectroscopy.

Chapter 2

Allyl coumarin (0.5 g, 2.33 mmol) was dissolved in anhydrous toluene and triethoxysilane (0.56 ml, 3 mmol) was added dropwise. The solution was heated to 50 °C, H₂PtCl₆ catalyst (8 wt. % in H₂O; 0.0011 g, 2.6 × 10⁻⁶ mol) was added, and the reaction was brought up to 70 °C. After reacting for 4 days, Pt(0) was filtered off and the remaining pale yellow solution was stripped of solvent *in vacuo*. The yellow oil was recrystallized with dichloromethane and pentane. ¹H NMR (300 MHz, CDCl₃) δ / ppm: 7.52 (d, 1H, 9 Hz), 6.9 (qd, 2H, 8.7 Hz, 2.7 Hz), 6.15 (d, 1H, 1.5 Hz), 5.5 (q, 1H), 4.63 (dq, 4H, 5.4 Hz), 2.45 (s, 3H), 1.58 (s, 2H), 1.28 (m, 9H), 0.9 (t, 2H, 6.6 Hz).

2.4.11 Synthesis of Urethane Coumarin Linkage

7-hydroxycoumarin (1 g, 6 mmol) was dissolved in 40 ml anhydrous THF. Isocyanatopropyltriethoxysilane (ICTES; 1.78 g, 7 mmol) was added dropwise to the reaction mixture, stirring under nitrogen. Upon addition dibutyltin laurate, the reaction was refluxed overnight. After cooling to room temperature and removal of solvent *in vacuo*, white solid was obtained. ¹H NMR of the crude product indicated the presence of ICTES starting material, which needed to be removed by heating to high temperature under vacuum. The white solid was washed with cold methanol (dry ice/acetone) and then with dry hexane to further remove starting material. The product was then recrystallized from methylene chloride and pentane, and subsequently characterized by ¹H NMR with resonances that correspond to reported values. ¹H NMR (300 MHz, CDCl₃) δ / ppm: 7.6 (d, 2H, 9.3 Hz), 7.15 (m, 2H), 6.25 (s, 1H), 5.6 (broad t, 1H), 3.9 (q, 6H, 6.9 Hz), 3.32 (q, 2H, 6 Hz), 2.45 (s, 3H), 1.75 (m, 2H), 1.29 (t, 9H, 6.9 Hz), 0.75 (t, 2H, 8.1 Hz).

2.5 References

1. Marcuse, D. *Theory of Dielectric Optical Waveguides*; Academic Press: San Diego, 1991.
2. Silfvast, W. T. *Laser Fundamentals*; Cambridge University Press: Cambridge, 1996.
3. Kogelnik, H. in *Topics in Applied Physics*, Tamir, T., Ed.; Springer-Verlag: Berlin, 1979, v. 7, p. 13-81.
4. Kogelnik, H.; Shank, C. V. *J. Appl. Phys.* **1972**, *43*, 2327.
5. Ghafouri-Shiraz, H.; Chu, C. Y. *J. Fiber Int. Optic* **1991**, *10*, 23.
6. Champagne, A.; Camel, J.; Maciejko, R.; Kasunic, K. J.; Adams, D. M.; Tromborg, B. *IEEE J. Quant. Electron.* **2002**, *38*, 1493.
7. Soderstrom, D.; Lourdudoss, S.; Carlstrom, C.-F.; Anand, S.; Kahn, M.; Kamp, M. *J. Vac. Sci. Technol., B* **1999**, *17*, 2622.
8. Chen, B.; Wang, W.; Wang, X.; Zhang, J.; Zhu, H.; Zhou, F. *Proc. SPIE-Int. Soc. Opt. Eng.* **1998**, *3547*, 12.
9. Rohbadey, J.; Martin, D.; Glick, M.; Silva, P. C.; Jouneau, P.-H.; Marti, U.; Reinhart, F. *K. Electron. Lett.* **1997**, *33*, 297.
10. Sin, Y. K.; Qiu, Y.; Muller, R. E.; Forouhar, S. *Electron. Lett.* **2001**, *37*, 567.
11. Liao, Z. L.; Flanders, D. C.; Walpole, J. N.; Demeo, N. L. *Appl. Phys. Lett.* **1985**, *46*, 221.
12. Miller, L. M.; Verdeyen, J. T.; Coleman, J. J.; Bryan, R. P.; Alwan, J. J.; Beernink, K. J.; Hughes, J. S.; Cockerill, T. M. *Photonics Technol. Lett.* **1991**, *3*, 6.
13. Shi, L.; Zhang, G.-X.; Wang, J.; Lo, D. *J. Opt. A: Pure Appl. Opt.* **2003**, *5*, L1.
14. Zhu, X.-L.; Lo, D. *Appl. Phys. Lett.* **2002**, *80*, 917.
15. Voss, T.; Scheel, D.; Schade, W. *Appl. Phys. B* **2001**, *73*, 105.
16. Oki, Y.; Yoshiura, T.; Chisaki, Y.; Maeda, M. *Appl. Opt.* **2002**, *41*, 5030.
17. Oki, Y.; Yoshiura, T.; Chisaki, Y.; Maeda, M. *Appl. Opt.* **2002**, *41*, 5030.

Chapter 2

18. Zhu, X.-L.; Lo, D. *Appl. Phys. Lett.* **2002**, *80*, 917.
19. Shi, L.; Zhang, G.-X.; Wang, J.; Lo, D. *J. Opt. A: Pure Appl. Opt.* **2003**, *5*, L1.
20. Zhu, X.-L.; Lo, D. *Appl. Phys. Lett.* **2000**, *77*, 2647.
21. Shank, C. V.; Bjorkholm, J. E.; Kogelnik, H. *Appl. Phys. Lett.* **1971**, *18*, 395.
22. Kogelnik, H.; Shank, C. V. *J. Appl. Phys.* **1972**, *43*, 2327.
23. Griffel, G.; Marshall, W. K.; Grave, I.; Yariv, A. *Opt. Lett.* **1991**, *16*, 1174.
24. Yanagi, H.; Hishiki, T.; Tobitani, T.; Otomo, A.; Mashiko, S. *Chem. Phys. Lett.* **1998**, *292*, 332.
25. Stathatos, E.; Lianos, P.; Stangar, U. L.; Orel, B. *Chem. Phys. Lett.* **2001**, *345*, 381.
26. Maruszewski, K. *J. Molecular Structure* **1999**, *479*, 53.
27. Zhang, Q. Y.; Que, W. X.; Buddhudu, S.; Pita, K. *J. Phys. Chem. Solids* **2002**, *63*, 1723.
28. Lo, D.; Parris, J. E.; Lawless, J. L. *Appl. Phys. B* **1993**, *56*, 385.
29. Sundar, V. C.; Eisler, H.-J.; Deng, T.; Chan, Y.; Thomas, E. L.; Bawendi, M. G. *Adv. Mater.* **2004**, *16*, 2137.
30. Sundar, V. C.; Eisler, H.-J.; Bawendi, M. G. *Adv. Mater.* **2002**, *14*, 739.
31. Förster, Th. *Ann. Phys.* **1948**, *2*, 55.
32. Scholes, G. *Annu. Rev. Phys. Chem.* **2003**, *54*, 57
33. Stewart, G.; Whitenett, G.; Atherton, K.; Culshaw, B.; Johnstone, W. *Proc. SPIE-Int. Soc. Opt. Eng.* **2004**, *4829*, 963.
34. Brown, S. S. *Chem. Rev.* **2003**, *103*, 5219.
35. Herman, M.; Lievin, J.; Auwera, J. V.; Campargue, A. *Adv. Chem. Phys.* **1999**, *108*, 1.
36. Morville, J.; Romanini, D.; Kachanov, A. A.; Chenevier, M. *Appl. Phys. B* **2004**, *78*, 465.
37. Todd, M. W.; Provencal, R. A.; Owano, T. G.; Paldus, B. A.; Kachanov, A.; Vodopyanov, K. L.; Hunter, M.; Coy, S. L.; Steinfeld, J. I.; Arnold, J. T. *Appl. Phys. B* **2002**, *75*, 367.

Chapter 2

38. Romanini, D.; Kachanov, A. A.; Sadeghi, N.; Stoeckel, F. *Chem. Phys. Lett.* **1997**, *264*, 316.
39. Rose, A.; Zhu, Z.; Madigan, C. F.; Swager, T. M.; Bulovic, V. *Nature* **2005**, *434*, 876.
40. Brinker, C. J.; Scherer, G. W. *Sol-Gel Science: The Physics and Chemistry of Sol-Gel Processing*; Academic Press: San Diego, 1990.
41. Avnir, D. *Acc. Chem. Res.* **1995**, *28*, 328.
42. Zhang, W.; Liu, W.; Li, B.; Mai, G. *J. Am. Ceram. Soc.* **2002**, *7*, 1770.
43. Tompkins, H. G. *A User's Guide to Ellipsometry*; Academic Press: Boston, 1993.
44. Grosso, D.; Balkenende, A. R.; Albouy, P. A.; Ayrat, A.; Amenitsch, H.; Babonneau, F. *Chem. Mater.* **2001**, *13*, 1848.
45. Schmidt-Winkel, P.; Yang, P.; Margolesee, D. I.; Chmelka, B. F.; Stucky, G. D. *Adv. Mater.* **1999**, *11*, 303.
46. Alberius, P. C. A.; Frindell, K. L.; Hayward, R. C.; Kramer, E. J.; Stucky, G. D.; Chmelka, B. F. *Chem. Mater.* **2002**, *14*, 3284.
47. Zhao, D.; Feng, J.; Huo, Q.; Melosh, N.; Fredrickson, G. H.; Chmelka, B. F.; Stucky, G. D. *Science* **1998**, *279*, 548.
48. Kubin, R. F.; Fletcher, A. N. *J. Lumin.* **1982**, *27*, 455.
49. Brackmann, U. *Lambdachrome Laser Dyes*; Lambda Physik: Göttingen, Germany, 1997.
50. Schattenburg, M. L.; Aucoin, R. J.; Fleming, R. C. *J. Vac. Sci. Technol., B.* **1995**, *13*, 3007.
51. Silfvast, W.T. *Laser Fundamentals*; Cambridge University Press: Cambridge, 1996.
52. Gee, L. G.; Berry, G. M.; Chen, C.-H. *Cytometry* **1989**, *10*, 151.
53. Kubin, R. F.; Fletcher, A. N. *J. Lumin.* **1982**, *27*, 455.
54. Suratwala, T.; Gardlund, Z.; Davidson, K.; Uhlmann, D. R. *Chem. Mater.* **1998**, *10*, 199.
55. Suratwala, T.; Gardlund, Z.; Davidson, K.; Uhlmann, D. R. *Chem. Mater.* **1998**, *10*, 190.
56. Brackmann, U. *Lambdachrome Laser Dyes*, Lambda Physik, Göttingen, Germany, 1997.

Chapter 2

57. Sutherland, R. M.; Dähne, C.; Place, J. F.; Ringrose, A. R. *Clin. Chem.* **1984**, *30*, 1533.
58. Elam, J. H.; Nygren, H.; Stenberg, M. J. *J. Biomed. Mater. Res.* **1984**, *18*, 953.
59. Smith, H. I. *Submicron- and Nanometer-Structures Technology*; NanoStructures Press: Sudbury, MA, 1994.

**Chapter 3. Distributed Feedback Grating Architectures
for Diffraction Based Arrays**

3.1 Diffraction Grating Response

3.1.1 Introduction to Diffraction Theory

The diffraction gratings of Chapter 2 may be used directly as sensing elements without the need for resonant stimulated emission. In this experiment, light is simply diffracted off of the grating. The intensity of the diffracted response can be variable to target analytes, thus establishing this method for sensing applications. Before the chemoresponsive diffraction measurement is presented, it is useful to review diffraction theory briefly. When a plane wave monochromatic beam is incident on the grating normal to the substrate's surface, diffraction occurs with a set of beams of order m ($m = 0, \pm 1, \pm 2, \pm 3 \dots$) depicted in Figure 3.1. The diffracted beams appear at angles ϕ_m with respect to the normal, as defined by the equation,

$$\sin \phi_m = \frac{m\lambda}{\Lambda} \quad (3.1)$$

where λ is the optical wavelength, and Λ is the grating period. This spatially periodic contrast of the complex index of refraction (\tilde{n}), which is the sum of real (n) and imaginary (k) components, is given by,

$$\tilde{n}(x, \lambda) = n(x, \lambda) + ik(x, \lambda) \quad (3.2)$$

where n and k at position x along the grating are wavelength dependent. It is important to note that $k(x, \lambda)$ is the absorptivity of the material at wavelength λ and position x and is given by,¹

$$k(\lambda) = \frac{2.3\lambda A(\lambda)}{4\pi d} \quad (3.3)$$

where $A(\lambda)$ is the absorbance and d is the thickness of the material. A periodic contrast of either n or k will result in diffraction, where phase grating behavior is a consequence of modulating the former and amplitude grating behavior is caused by the contrast of the latter. Modulation of both n and k in a grating is described as a mixed grating. When the grating material is non-resonant

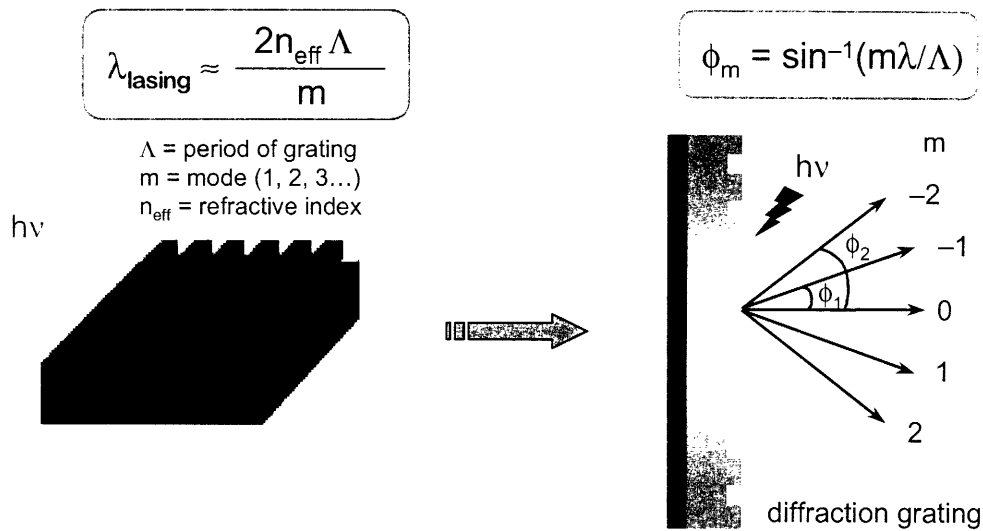


Figure 3.1. Using a DFB to obtain a diffraction grating pattern of specific modes ($m = 0, \pm 1, \pm 2 \dots$) at angles ϕ_m .

(i.e., the lattice material does not absorb excitation light), the lattice exhibits pure phase grating behavior. Under resonance conditions, the lattice behaves as a mixed grating so it requires treatment of both $n(\lambda)$ and $k(\lambda)$ in detection studies.

It is assumed that in most experimental situations that the total diffraction efficiency is low ($\eta < 0.01$), so it is approximated for a grating produced by a sinusoidal variation of n and/or k as,^{2,3}

$$\eta(\lambda) = \exp\left[-\frac{2.3A(\lambda)}{\cos\theta}\right] \left[\frac{\pi d}{\lambda \cos\theta}\right] \left[\Delta k(\lambda)^2 + \Delta n(\lambda)^2\right] \quad (3.4)$$

where θ is the Bragg angle, and $\Delta n(\lambda)$ and $\Delta k(\lambda)$ are, respectively, the difference in the peak-null values of n and k at a specific wavelength. One can see from eq. (3.4) that η is proportional to the square of the absorptivity and refractive index modulation terms.

3.1.2 Chemoresponsive Diffraction Measurements

Operationally, the diffraction efficiency is obtained as the ratio of the diffracted signal intensity to the non-diffracted signal intensity ($I_{1,0} / I_{0,0}$), as shown in Figure 3.2. The DFB

architectures constructed in Chapter 2 are approximated as “thin” gratings, where there is little variation in the thickness of these films. The diffraction efficiency for these samples is approximated by,⁴

$$\eta_{1,0} = a \left(\frac{\pi d}{\lambda \cos \theta} \right)^2 [(\Delta n)^2 - (\Delta k)^2] \quad (3.5)$$

and η is directly proportional to the square of the grating path length, d , and the square of the difference in refractive index, Δn , between the chemoresponsive lattice and the surrounding medium, $\Delta n = n_{\text{lattice}} - n_{\text{medium}}$, at a constant probe wavelength λ . When the grating is non-resonant, $\Delta k = 0$, and therefore the change in η is simply a function of the index contrast before and after analyte exposure.

If gratings exhibit electronic resonance, in conditions where the lattice material absorbs the probe light, the changes in diffraction efficiency can be significantly amplified and therefore the detection limits of this signal transduction method will be increased.^{4,5} This is shown in Figure 3.2, where the sol-gel film that makes up the diffraction grating material is impregnated with a molecule that absorbs at the excitation laser wavelength. To impart selectivity to this technique, impregnation of the sol-gel matrix with a solvatochromic compound/dye will provide

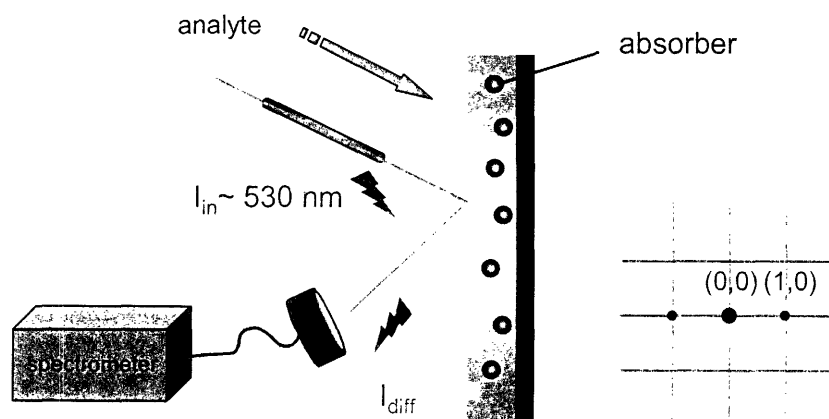


Figure 3.2. Diagram of detection setup for diffraction gratings, where the diffraction spot intensity ($I_{1,0}$) is monitored relative to the undiffracted spot intensity ($I_{0,0}$) as a function of Δn .

both a chromophore and a chemoresponsive site in the grating. Bailey and Hupp have exploited the vapo-chromic behavior for resonant gratings and find that the change in refractive index induces a photonic lattice response to a representative analyte can be amplified by 3.5 orders of magnitude.⁴ Examples of devices that employ similar detection methods relying on index contrasts include optical fibers and waveguides,⁶⁻⁸ thin-film interferometry from porous silicon,⁹⁻¹² Bragg-reflector-based porous silicon microcavities,¹³ Kretschmann geometry surface plasmon resonance (SPR) spectroscopy,^{14,15} and localized surface plasmon (LSPR) spectroscopy.¹⁶ Analyte recognition can be introduced to the overall detection scheme by incorporating chemically specific receptor sites to these sensors.^{10,13}

Hupp and co-workers have constructed 2-D gratings or “photonic lattices” of $[\text{Pt}(\text{CNC}_6\text{H}_4\text{C}_{10}\text{H}_{21})_4][\text{Pd}(\text{CN})_4]$ and polymers featuring nanoscale pores.^{4,5} A hexane suspension of the molecular squares is micropatterned using capillary action and a PDMS stamp with an array of $5 \times 5 \mu\text{m}^2$ features. With a lattice periodicity of $\sim 10 \mu\text{m}$, these materials readily diffract monochromatic visible light, generating a characteristic diffraction pattern that is related to the physical pattern of the lattice by a Fourier transform. Upon exposure to volatile organic compounds (VOCs) such as chloroform and methanol, the gratings with initial refractive index (n) adsorb the VOCs. The uptake results in a change in the material’s complex refractive index, \tilde{n} , which is accompanied by a change in the degree of index contrast between the lattice and the surrounding medium (in this case, air). This ultimately leads to a change in the diffraction efficiency (η) of the grating,¹

$$\eta_m = \frac{I_m}{I_i} \quad (3.6)$$

where the diffraction efficiency of the m^{th} order diffracted spot is the ratio of the intensity of that spot (I_m) and the intensity of the incident beam (I_i). The presence of polarizable analyte species in the material causes the refractive index of the lattice to increase, since the air ($n = 1$) or water ($n = 1.33$) in the void space is replaced by an organic compound with higher $n \sim 1.4 - 1.5$. With

the increased index of the porous material, a greater degree of index contrast with the surrounding environment and an increase in diffraction efficiency is obtained. This method is deemed general because all molecules contain polarizable electrons; therefore, all molecules have the capability of inducing changes in refractive index and diffraction efficiency when impregnated in porous host matrices. The major drawback to this transduction mechanism and other similar schemes that rely on changes in refractive index is the lack of chemical selectivity in signaling generation.

The porous “vapochromic” $[\text{Pt}(\text{CNC}_6\text{H}_4\text{C}_{10}\text{H}_{21})_4][\text{Pd}(\text{CN})_4]$ compound is responsive only to a range of volatile organic compounds at saturation vapor pressures.^{17,18} The chemoresponse depends on the molecule’s adsorption of analyte and the ensuing change in the absorption spectrum of the square lattice provides sensing amplification through resonance. In addition, Hupp used polymers (polyepichlorohydrin, polyisobutylene and polybutadiene) that act as a host to organic solvents, limiting the chemoresponse of his diffraction gratings to the adsorption of analyte with low selectivity. To impart targeted detection with a resonant response, the squares (and its absorbance) must be modified for different analytes and this can prove to be cumbersome for the countless number of environmental interferents. With the approach described in this Chapter, the use of the $\text{SiO}_2 / \text{TiO}_2$ DFBs fabricated in Chapter 2 separate the resonant response from both receptor site and matrix porosity. A matrix with controlled porosity, which can be augmented with a covalently attached receptor site for specificity and an external dye for resonance, is advantageous to the polymer and molecular square devices. What is needed are precisely the DFBs already described in Chapter 2, only with a larger grating periodicity (Λ) required for visible diffraction. The separation of the receptor site from the resident chromophore imparts versatility to these diffraction gratings. Additionally, more complicated structures for self-referencing and correction, as will be described below in Section 3.3, can be constructed.

3.2 Results and Discussion

The diffraction sensor arrays of Hupp and co-workers motivated us to investigate whether the SiO₂ / TiO₂ DFB structures fabricated in Chapter 2 demonstrate similar responses to volatile organic compounds. By impregnating the film with a dye that absorbs the excitation wavelength, we can monitor the *resonance* amplified changes in the diffraction intensity. The porosity of the films allow for diffusion of analyte and solvents into the matrix. Polar solvents are expected to associate well with the surface and the pore walls of the sol-gel matrix because the pore environment reflects that of an aqueous alcohol solvent.¹⁹ Solvents with higher dielectric constants were also found to diffuse faster into porous sol-gel glasses than solvents with lower dipole moments.^{20,21} As a comparison, the bulk diffusion coefficients for acetonitrile²² and chloroform²³ are $4.04 \times 10^{-9} \text{ m}^2/\text{s}$ and $2.44 \times 10^{-9} \text{ m}^2/\text{s}$, respectively. When the solvents reside in the sol-gel pores, the effective diffusion coefficients are significantly lower: $10.8 \times 10^{-10} \text{ m}^2/\text{s}$ and $4.1 \times 10^{-10} \text{ m}^2/\text{s}$ for acetonitrile and chloroform, respectively.²⁰ Interestingly, the factor of difference between the bulk and pore diffusion coefficients is much larger for chloroform and other non-polar solvents. Polar solvents like methanol and acetonitrile can form stronger hydrogen bonds with the surface silanol bonds, which is expected to immobilize the adsorbed solvent molecules and slow down translational displacement. However, the polar molecules are presumed to have faster adsorption and desorption processes at the surface, and higher mobility within the pores of the sol-gel, resulting in a higher measured diffusion coefficient.²¹ These literature results prompted us to test the porosity and vapochromic diffraction response of the DFBs in the presence of non-polar (chloroform) vs. polar (acetonitrile and methanol) vapors.

Initial experiments were conducted on a 2:1 SiO₂ / TiO₂ film doped with 4-dicyanmethylene-2-methyl-6-(p-dimethylaminostyryl)-4*H*-pyran (DCM), a laser dye that exhibits spectral changes in the presence of different solvents. The DCM dye also absorbs at the excitation wavelength $\lambda = 532 \text{ nm}$, and thus can provide signal amplification as a resonant type grating. A grating pattern, with $\Lambda = 385 \text{ nm}$ from the PDMS stamps described in Chapter 2, was

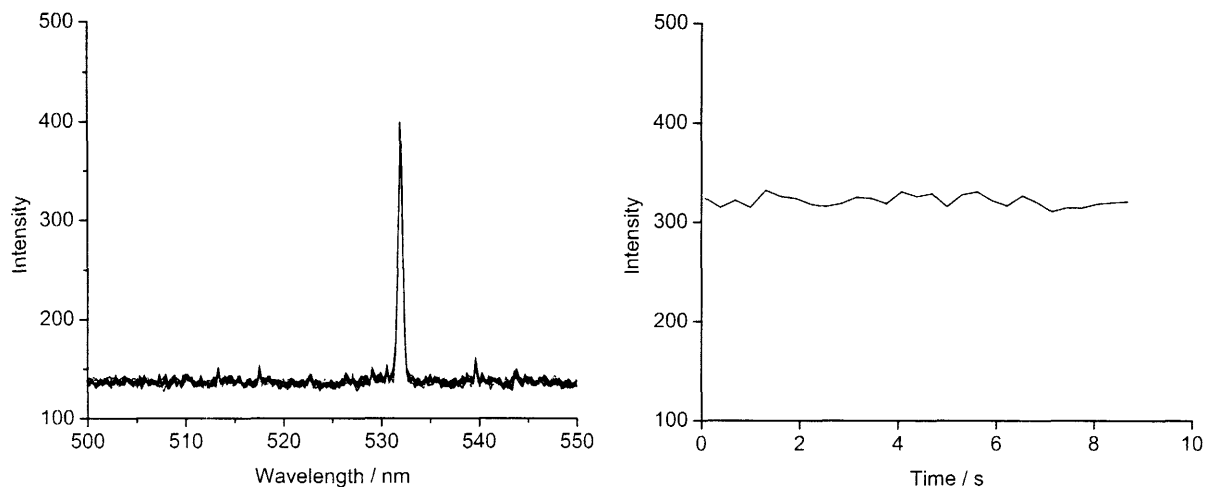


Figure 3.3. (left) Monitoring the diffracted spot for a sol-gel DFB impregnated with DCM dye. (right) Time trace of the intensity. Data collected every 300 ms.

imposed on the sample. One diffraction spot was observed, as expected from Bragg's law, and the intensity of that beam was monitored with a CCD spectrophotometer. Excitation sources included both a He-Ne laser and a green laser pointer, both of which were confirmed to have stable radiation output before measurements. Time response and reproducibility are crucial factors for the vapor detection system studied here, and the introduction of solvents to the DFB was repeated in monitoring film responses.

A control experiment monitoring the diffracted spot intensity ($\lambda_{\text{exc}} = 532 \text{ nm}$) upon exposure of the film to pressurized air is shown in Figure 3.3. The trace on the right of Figure 3.3 plots the corresponding intensity as a function of time with the data collected every 300 ms. As expected, the diffraction intensity remains relatively constant ($\pm 5.6 \text{ a.u.}$). Figure 3.4 shows the time-resolved diffraction response of this test grating upon repeated exposure/pause cycles of two polar organic solvents: acetonitrile and methanol. Upon exposure of the $\text{SiO}_2 / \text{TiO}_2$ gratings with acetonitrile vapor, possessing a dielectric constant $\epsilon = 38.8$,²⁴ the intensity of the monitored diffraction spot changed dramatically. Over the course of 2 min, the vapor was cycled in and out, and the traces in Figure 3.4a show the response of the grating as the acetonitrile solvent diffuses in and out of the pores. The local refractive index mismatch is altered when there are resident

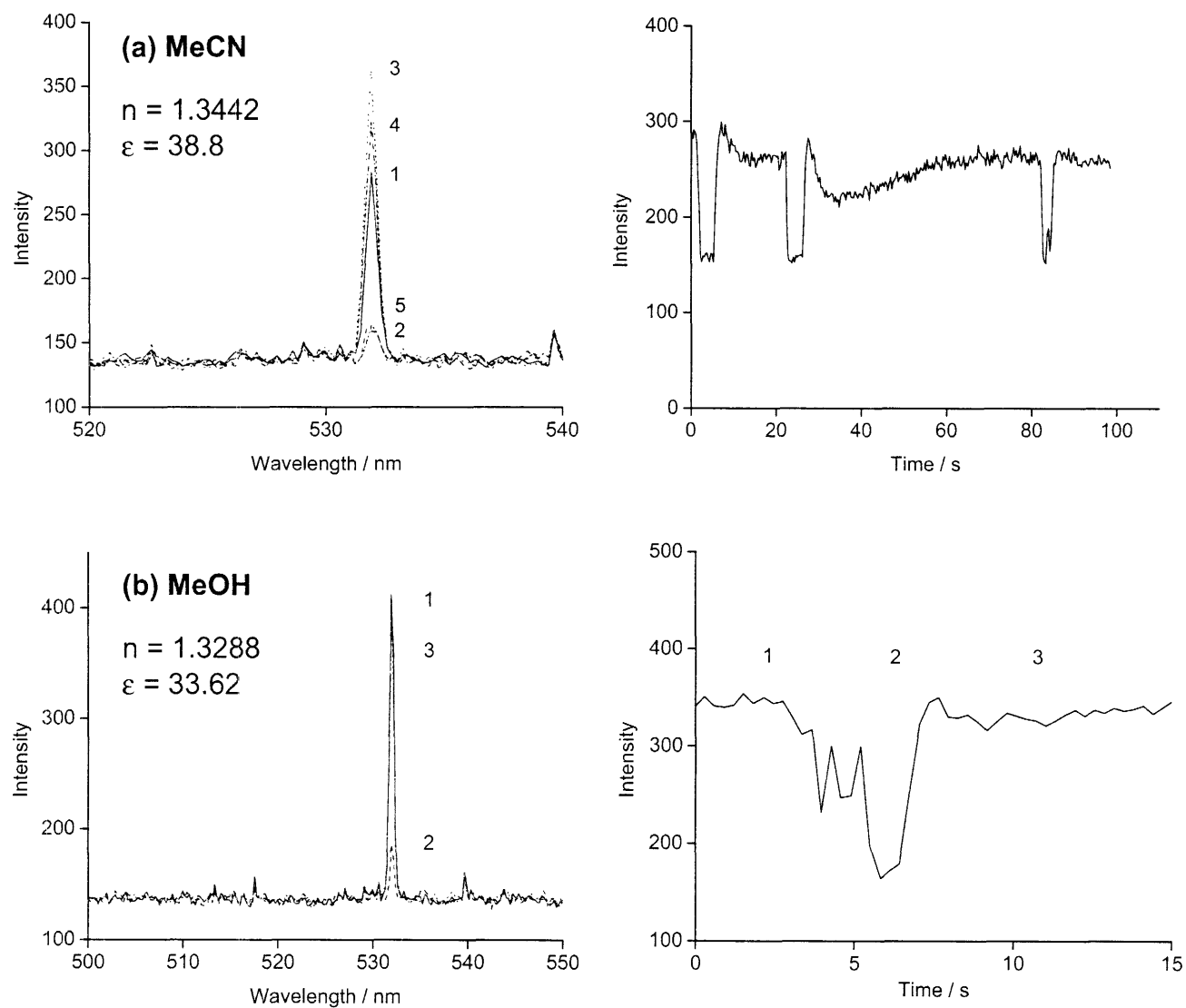


Figure 3.4. (left) Monitoring the diffracted spot for a sol-gel DFB impregnated with DCM dye. (right) Time trace of the intensity. Data collected every 300 ms. (a) Acetonitrile and (b) methanol are compared here. Refractive index (n) and dielectric constant (ϵ) are listed for each solvent.

solvent molecules in the sol-gel matrix, resulting in a change in diffraction efficiency, as explained by eq. (3.5). This qualitative contrast in intensity is mirrored in experiments where the same sample is exposed to methanol ($\epsilon = 33.62$).²⁴ As shown in Figure 3.4b, the intensity of the diffracted spot decreases in the presence of methanol and recovery of the intensity is observed when the solvent diffuses out of the pores.

In contrast, non-polar solvents have a smaller diffusion coefficient in sol-gels; therefore, chloroform ($\epsilon = 4.806$)²⁴ should not be able to penetrate pores as efficiently and the films should not exhibit any response. As shown in Figure 3.5, the intensity remains relatively constant with a standard deviation of ± 6.1 a.u. Although these are very preliminary results, they do indicate that the prepared $\text{SiO}_2 / \text{TiO}_2$ films are porous to analyte and that the diffracted spot intensity is affected by changes in the effective refractive index. These proof-of-concept experiments demonstrate the ability of the sol-gel DFB gratings to signal (as a simple diffraction grating) the presence of polar compounds (VOCs). Inclusion of an absorbing organic chromophore within the pores serves to increase the index mismatch and thereby amplifying the diffraction grating response by resonance.

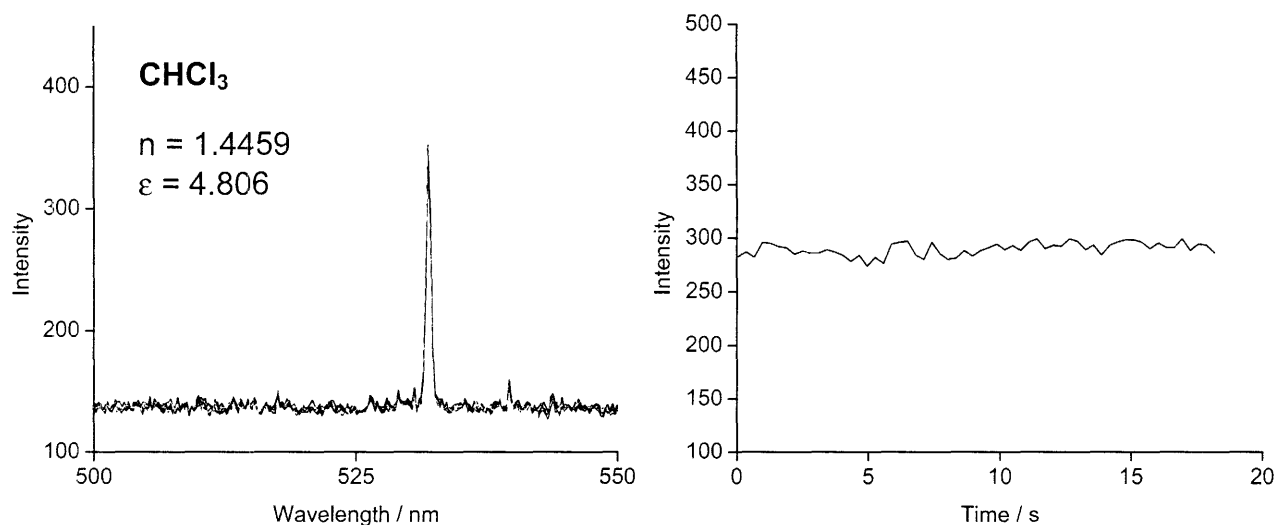


Figure 3.5. (left) Monitoring the diffracted spot for the same sample as in Figure 3.4. Refractive index (n) and dielectric constant (ϵ) is listed for chloroform. (right) Time trace of the intensity. Data collected every 300 ms.

3.3 Future Directions

The preliminary experiments shown in Figure 3.4 and 3.5 did not measure the diffraction efficiency of the grating, as related in eq. (3.6). To obtain η , two photodetectors (monitoring $I_{0,0}$ and $I_{1,0}$) wired in a circuit to generate a signal output are required. The initial experiments were conducted with the only available CCD detector at the time. Since then, we have been able to construct a detector with two phototransistors wired in a Wheatstone Bridge configuration, which is then connected to a voltmeter to obtain current output. The reading can then be digitized by feeding the signal into a National Instruments Data Acquisition card interfaced with LabView software. More photodiodes can then be added to the series for multiplex measurements.

For future experiments, the ability to monitor multiple diffraction spots requires gratings with larger periodicities. One can envision positioning a photodiode at each higher order diffraction peak to further ensure accuracy in measurements. The master gratings obtained from RLE have spacings of $\Lambda = 280 - 360$ nm, which are too narrow to diffract visible light with more than one mode. Ruled reflective gratings with 600 grooves/mm blazed for 500 nm light were obtained, and were used to fabricate PDMS templates. Those stamps were then used to generate efficient diffraction gratings on the thin films, and future sensing investigations should be

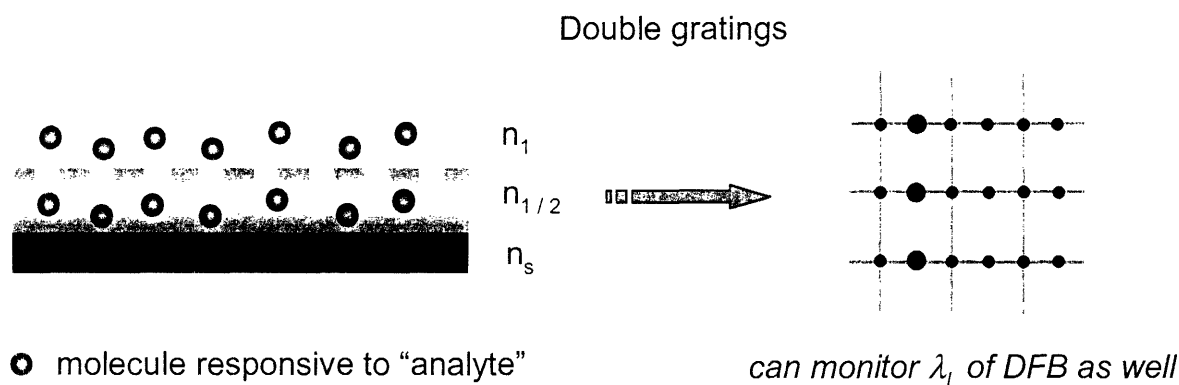


Figure 3.6. Use of second grating (with n_1 or n_2) allows it to act as a control channel in sensing measurements. For a resonant grating with appropriate Λ , the lasing of the DFB (λ_L) can also be monitored.

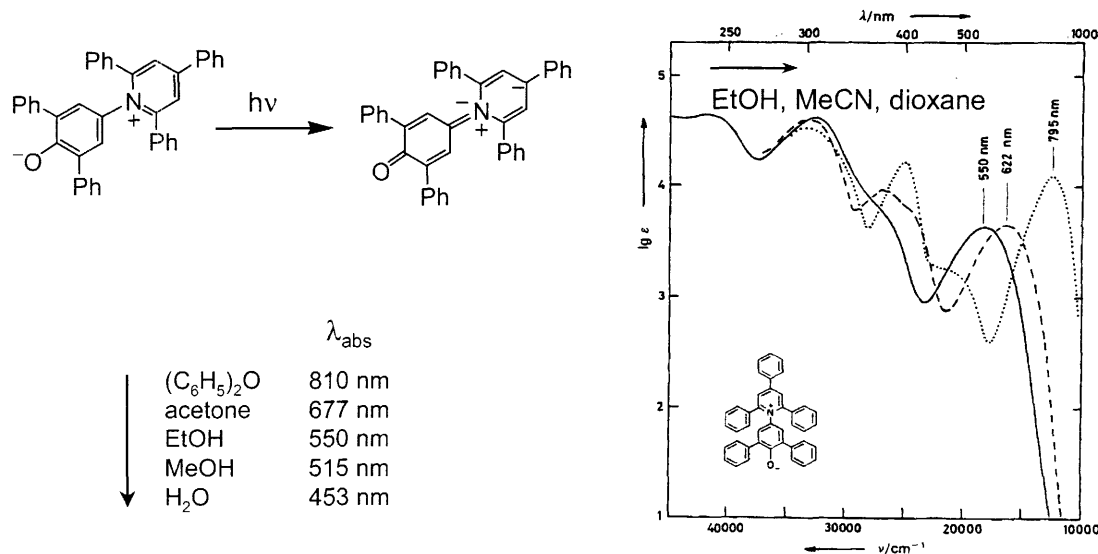


Figure 3.7. Reichardt's dye (pyridinium-*N*-phenoxide betaine) exhibits a hypsochromic shift as shown in the absorbance spectrum on the right (from Ref. 25).

performed on these visible light diffracting platforms.

Use of a solvatochromic dye that is responsive to one solvent and not all others will provide a useful proof-of-principle experiment to test the utility and amplification potential of this technique to our films. An additional grating of the same material (i.e., with same refractive index n_1) or different material (n_2) hosting the chemoresponsive chromophore can also be imposed as the bottom “cladding” layer. This second grating, with its own diffraction pattern, can serve as the control channel; the intensity of the monitored diffracted spot of the second grating should not change in the presence of analyte. The index mismatch, a factor of the diffraction efficiency, is not as drastic for the bottom layer as it is for the top grating, which contrasts with air. The detection of analyte can be further confirmed by the parallel measurements of both gratings, as depicted in Figure 3.6. If the diffraction grating has the appropriate period to act as a DFB, then the emission (λ_L) from the laser cavity can also be monitored. A well-known solvatochromic dye is pyridinium-*N*-phenoxide betaine (Reichardt's dye), which exhibits a hypsochromic shift in its absorbance spectrum.²⁵ The range of its absorption maximum from non-polar ethers to water is shown in Figure 3.7. What is ideal about

this dye is its ability to shift its absorption peak off- and on-resonance in the presence of the respective solvent. This will prove to be powerful because the diffraction efficiencies will vary greatly between those two states of the grating.

3.4 Concluding Remarks

In this thesis, two possible and exciting avenues of future work for the DFBs are described. The silica – titania films of our DFB lasers can easily be modified via silylation coupling reactions. Execution of these surface functionalizations, the chemistry of which has been previously explored, will result in numerous possibilities for chemo- and bio-sensing applications. Immobilization of laser dye chromophores and indicators is just the beginning of surface modification chemistry that can be utilized, and similar reactions can be carried out with bioreceptors and silanes to provide receptor sites for targeted biomolecules.

Although a lot of work has been described in Chapter 2 regarding the optical waveguiding and emission properties of our DFB thin films, the diffraction grating itself can be exploited in a much simpler manner. The diffraction grating, with the appropriate periodicity, possesses a diffraction pattern upon probing with visible light. Its diffraction efficiency is a function of the index contrast between the host material and its environment; the presence of an organic analyte within the material induces a change in the index mismatch and ultimately the intensity of the diffraction spots. Fortunately, our porous waveguide matrices are suitable for adsorption of analyte and allow for the incorporation of a variety of chromophores to fabricate resonant gratings. Especially with the incorporation of two gratings into one device, the performance capabilities will be unprecedented, allowing for multiple measurements to be made in parallel.

3.5 Experimental

3.5.1 Materials

Glass and silicon substrates were cleaned using Piranha solution and subsequently with the RCA SC-1 method. They were then dried with a stream of clean, pressurized nitrogen. Laser dyes were obtained from Lambda Physik, Inc. Solvents are reagent grade or better. Film precursors were obtained from Sigma Aldrich, Strem Chemicals and TCI America. All materials were used as received.

3.5.2 Preparation of PDMS Stamps

The DFB master template for these studies was a ruled grating blazed for 500 nm with 600 lines/mm obtained from Thor Labs. The grating was evacuated inside a vacuum chamber for 20 min and 2 min intervals, cycled twice, in the presence of tridecafluoro-1,1,2,2-tetrahydrooctyltrichlorosilane (United Chemical Technologies). Poly(dimethyl)siloxane (PDMS) stamps were prepared from mixing precursors Sylgard 184 Silicone Elastomer base and Silicone Elastomer curing agent (Dow Corning Corp.) in a 10:1 ratio (wt. %). The degassed mixture was then poured onto the template and allowed to cure for 2 days at room temperature. Although this “master grating” is not fabricated on a silicon substrate, the PDMS preparation can be repeated without destroying the grating.

3.5.3 Preparation of Diffraction Gratings

The sol-gel thin films are prepared as mentioned previously; the films are spin-cast at 2000 - 3000 RPM for 1 min onto clean glass substrates at room temperature in a controlled nitrogen-purged environment of low humidity. Immediately after spinning, the PDMS stamp and a 200 g weight are placed on top of the film to emboss the pattern. The films are then cured at 200 °C for 2 min.

A second method for the grating with larger periods was also used where the sol-gel was syringed onto the substrate, and the PDMS stamp was subsequently placed onto the glass without spinning. The film was then cured at 200 °C for 2 min with even weight distribution placed on the stamp. Diffraction gratings were successfully transferred mainly at the two ends of the substrate and less so at the middle where the pattern appeared to smear out.

3.5.4 Diffraction Grating Measurements

The light source utilized is a Helium-Neon laser (Melles Griot) or a diode laser pointer ($\lambda = 532$ nm). The samples were mounted so that the incident laser beam was normal to the sample. The diffracted beam was focused onto the fiber optic detector that fed into a CCD spectrophotometer with an entrance aperture of 25 μm and 600 lines/mm grating blazed at 500 nm (Ocean Optics HR 2000). Vapor from solvent was directed straight onto the sample and the intensity of the diffracted beam was monitored as a function of time (minutes).

A more elaborate setup was constructed so that both diffracted and undiffracted beams are collected using infrared phototransistors (Radio Shack) powered by a 9V battery, and the signal is digitized by a personal computer via a National Instruments DAQ card and Lab View software. The sample can be mounted in a specially designed flow cell that was fabricated at the MIT Central Machine Shop. Solvent and other organic analyte are injected through PTFE tubing and constant gas pressures can be introduced with a simple aquarium pump.

3.6 References

1. Schanze, K. S.; Bergstedt, T. S.; Hauser, B. T.; Cavalaheiro, C. S. P. *Langmuir* **2000**, *16*, 795.
2. Fayer, M. D. *Annu. Rev. Phys. Chem.* **1982**, *33*, 63.
3. Nelson, K. A.; Casalegno, R.; Miller, R. J. D.; Fayer, M. D. *J. Chem. Phys.* **1982**, *77*, 1144.
4. Bailey, R. C.; Hupp, J. T. *J. Am. Chem. Soc.* **2002**, *124*, 6767.
5. Bailey, R. C.; Hupp, J. T. *Anal. Chem.* **2003**, *75*, 2392.
6. *Chemical and Biochemical Sensing with Optical Fibers and Waveguides*; Artech House: Norwood, MA, 1996.
7. Kooyman, R. P. H.; Lechuga, L. M. *Handbook of Biosensors and Electronic Noses*; CRC Press: Boca Raton, FL, 1997.
8. Lenferink, A. T. M.; Schipper, E. F.; Kooyman, R. P. H. *Rev. Sci. Instrum.* **1997**, *68*, 1582.
9. Gao, J.; Gao, T.; Li, Y. Y.; Sailor, M. J. *Langmuir* **2002**, *18*, 2229.
10. Dancil, K.-P. S.; Greiner, D. P.; Sailor, M. J. *J. Am. Chem. Soc.* **1999**, *121*, 7925.
11. Liu, R.; Schmedake, T. A.; Li, Y. Y.; Sailor, M. J.; Fainman, Y. *Sensors and Actuators, B* **2002**, *87*, 58.
12. Gao, J.; Gao, T.; Sailor, M. J. *Appl. Phys. Lett.* **2000**, *77*, 901.
13. Chan, S.; Homer, S. R.; Fauchet, P. M.; Miller, B. L. *J. Am. Chem. Soc.* **2001**, *123*, 11797.
14. Grassi, J. H.; Georgiadis, R. M. *Anal. Chem.* **1999**, *71*, 4392.
15. Jordan, C. E.; Frutos, A. G.; Thiel, A. L.; Corn, R. M. *Anal. Chem.* **1997**, *69*, 4939.
16. Malinsky, M. D.; Kelly, K. L.; Schatz, G. C.; Van Duyne, R. P. *J. Phys. Chem. B* **2001**, *105*, 2343.

Chapter 3

17. Exstrom, C. L.; Sowa, J. R.; Daws, C. A.; Janzen, D.; Mann, K. R. *Chem. Mater.* **1995**, *7*, 15.
18. Daws, C. A.; Exstrom, C. L.; Sowa, J. R.; Mann, K. R. *Chem. Mater.* **1997**, *9*, 363.
19. Dunn, B.; Zink, J. I. *Chem. Mater.* **1997**, *9*, 2280.
20. Koone, N.; Shao, Y.; Zerda, T. W. *J. Phys. Chem.* **1995**, *99*, 16976.
21. Koone, N.; Zerda, T. W. *J. Sol-Gel Sci. Technol.* **1997**, *8*, 883.
22. Kovacs, H.; Kowalewski, J.; Maliniak, A.; Stilbs, P. *J. Phys. Chem.* **1989**, *93*, 962.
23. Mills, R.; Malhotra, R.; Woolf, L. A.; Miller, D. G. *J. Chem. Eng. Data* **1994**, *39*, 929.
24. Weast, R. C., Ed. *CRC Handbook of Chemistry and Physics*, 55th ed.; CRC Press: Cleveland, Ohio; 2003
25. Reichardt, C. *Solvents and Solvent Effects in Organic Chemistry*; VCH Publishers: Weinheim, Germany, 1988.

**Chapter 4. Reversibly Caged Dyes for Molecular Tagging Velocimetry
Measurements of Microflows**

4.1 Introduction

4.1.1 Sensing Physical Phenomena

The previous chapters have focused on attempts to bring the 3R chemosensing strategy to the nanoscale regime, where the challenge has been to amplify a fluorescent signal for detection at small length scales. The ability to control and perform such physical and chemical transformations over small spatial domains is an emerging theme of future chemical sciences. The development of the chemical sciences in microenvironments, however, demands more than a static architecture – it will also demand a fundamental understanding of flow and mass transport over small length scales. With this understanding, the interaction of analyte with the micro-fabricated devices of Chapters 2 and 3 may be controlled.

Microscopic flows are driven either electroosmotically or by a pressure differential. Important and unresolved issues are connected to the flow field generated in the microdomain and the motion of the various constituents carried by the fluid. In particular, the nature of the boundary conditions at the wall of these devices, which is of fundamental importance to the prediction of the flow, has eluded description. A variety of physical variables may impact these boundary conditions, including the nature of the fluid (e.g., polarity), the wall surface charge characteristics and surface roughness. To date, few diagnostic techniques permit this quantitative information to be obtained. Current tools for mapping flow in small channels and determining wall boundary conditions near their surfaces are largely accomplished with particle-based techniques. These techniques become severely problematic when the size of the flow channels shrink. As the size of the seed particles decreases, the reduction in their scattering efficiency makes them unsuitable for detection. Even if fluorescent-coated particles are used, flow measurements are always hampered by the potential interaction of particles with walls and by complications arising from forces that act on the particles that do not originate from the fluid. These constraints are eliminated when the particles are replaced with *molecular* markers, such as the 3R optical supramolecules described in Chapter 1.

A key feature of 3R system for *chemical sensing*, as described in Chapter 1, is that the analyte is in direct equilibrium with the recognition site. The intensity of the signal is therefore proportional to dynamic communication with the analyte, and the success of the optical supramolecules relies on the luminescence properties to be affected by analyte in the environment. However, when the optical chemosensor is made insensitive to the environment by eliminating this equilibrium, a bright, invariant emission is observed. Elimination of the equilibrium between the analyte and the receptor minimizes external quenching mechanisms, allowing the resulting phosphorescence to measure physical phenomena. Signals of this type may be used to implement *physical sensing* techniques that are of particular utility to understanding flows. Figure 4.1 illustrates the approach that we have used to transform the 3R chemical sensors into physical sensors. By effectively capping the supramolecule to entrap the lumophore inside the CD, ternary 3R active sites can maintain the long-lived signaling for physical sensing applications.

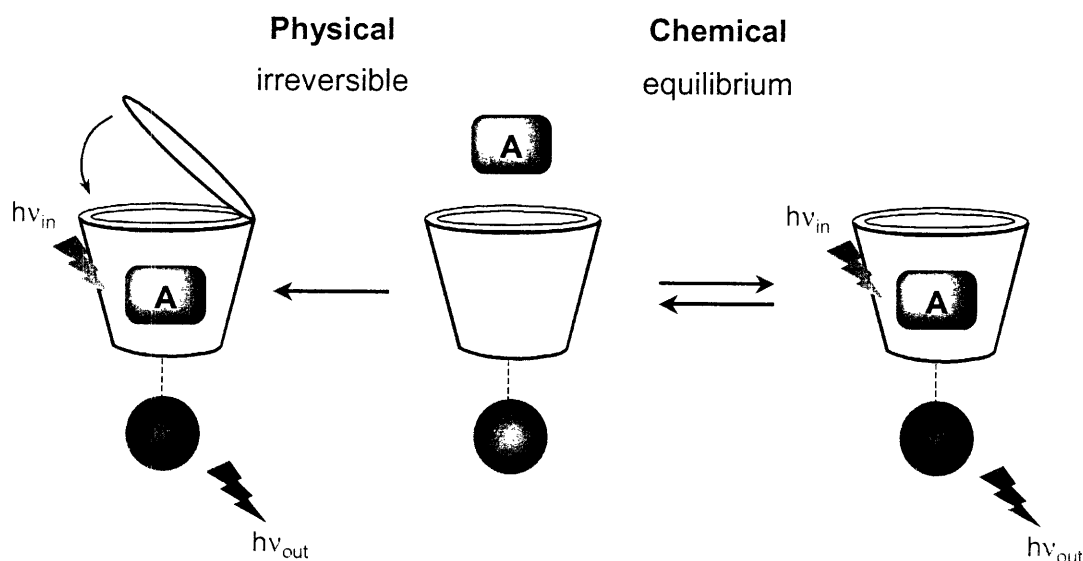


Figure 4.1. Amended 3R scheme from Chapter 1 to include physical sensing. The ability to detect physical phenomena with molecules is currently an irreversible process.

4.1.2 Molecular Tagging Velocimetry (MTV)

Turbulence is a fundamental phenomenon, and the use of optical techniques is central to quantitatively measuring the motion of fluids. Particle Imaging Velocimetry (PIV)¹ is a state-of-the-art optical technique for measuring fluid flow, where the fluid is seeded with particles like polystyrene microspheres or metal particles. A section of the flow is illuminated with a sheet of laser light, and the reflection identifies the positions of the particles. After a period of time (Δt), a subsequent laser sheet records the positions, and the velocity of a defined group of particles can be determined. Although this is a powerful technique because it can instantaneously measure the velocity of a fluid at many points, there are many drawbacks to using particles. It is assumed that the particles encompassed with the initial laser sheet remain in the same layer of fluid to be illuminated again. However, with highly three-dimensional flows, this is not the case. In addition, particles themselves possess inertia and may not necessarily track with the fluid flow, especially when it changes suddenly. Finally, particles may not enter areas of interest for measurement, especially at a critical boundary layer and at the core of strong, concentrated vortices.

These limitations are overcome by the development of Molecular Tagging Velocimetry (MTV),²⁻⁴ which incorporates the use of a soluble luminescent compound, such as the ones shown in Figure 4.1, as an *in situ* probe of dynamic fluid flow. Since the molecules are part of the flow, all problems associated with particles are eliminated in the MTV technique. In a typical MTV experiment, laser excitation off a grating of the molecular probes within a fluid generates a glowing grid. Distortion of this grid is monitored in real time by a CCD camera, and the velocity vectors of the flow are then calculated from the time-resolved snapshots of the glowing grid. By measuring the distance and direction each grid intersection travels and knowing the time delay between each image, the two velocity components in the grid plane may be determined.

Bringing physical sensing to the microdimensions requires the development of new optical diagnostic techniques to quantitatively measure both macroscopic and microscopic flows

of interest to fundamental fluid physics and applied engineering. This Chapter reports on progress towards the development of new molecular probes that incorporate this “turn-on” approach for measuring turbulence in slow flow and microflow systems. It will be important to elucidate the photophysical mechanism by which these sensors operate, as such evaluation is necessary to optimize their detection capabilities.

4.1.3 Limitations of MTV in the Microdomain

The particle-to-molecule motivation that drove our group to create the MTV technique for studies of macroscopic flows also presents itself in studies of microflows. The most developed experimental tool for the *in situ* imaging of microflows is the recent μ PIV technique (extension of Particle Image Velocimetry, PIV, to microfluidics).^{5,6} As is the case for macroscopic measurements, several complications arise from the use of particle tracers in microflow geometries. These complications are due to the fact that the fluid motion is not measured directly but is inferred from the motion of particles. Particles in strong regions of shear, such as those encountered near walls, move away from the wall due to an induced lift force. As the size of seed particles decreases (200 nm particles are typical of high resolution measurements), these shear-induced effects are minimized but at the expense of significant reduction in scattering efficiency. The most challenging issues in interpreting solid particle motion near boundaries and in microchannels is the need to account for the effect of electrothermal, electrophoretic and dielectrophoretic forces, which must be determined in order to isolate the particle motion that is due to motion of the fluid.

These complications are circumvented by molecular-based techniques. Preliminary investigations to date have used caged-fluorescent dyes to image microflows.⁷ Most of this work was qualitative, and the uncaged dyes used so far are charged molecules. The motion of this “charged tag” is significantly perturbed in electroosmotic flows (EOF) owing to the presence of a strong external electric field. In these cases, the dye does not follow the motion of the carrier neutral fluid. This problem is eliminated with the optical supramolecular approaches using

neutral tracers. Nevertheless, the MTV approach as developed to date possesses one very significant limitation for the measurement of microflows: the non-quenchable, emissive excited states live for 10 ms. Since the CCDs that are used are sufficiently sensitive to detect luminescence comfortably over 5 lifetimes, flows may be imaged over timescales of 50 ms. Within these limits, tracers currently employed for MTV enable flows with speeds of 1 mm/s or faster to be measured. However, the flow structures of pertinence to microflows can move as slow as 0.001 mm/s. To advance the MTV technique by even one order of magnitude the luminescence lifetime (τ) of a tracer must be pushed to 100 ms. Unfortunately, most lifetimes of phosphorescent molecules do not approach this limit and thus previous approaches developed in our group are therefore inapplicable to the microflow problem.⁸ In light of these limitations, conceptually new tracers must be developed that can produce an image according to photophysical principles other than direct phosphorescence. Additionally, there are several other limitations in chemistry and photophysics of MTV tracers that will need to be overcome for the measurement of microflows. The design of new molecules and materials demands the following:

- The luminescence must be intense (i.e., non-quenched) and long-lived.
- The tracers must be compatible with hydrophobic and aqueous solutions.
- The tracers must exhibit reversibility so multiple measurements can be made on the same molecularly doped fluid.

This Chapter presents the development of new tracers that meet the foregoing criteria. The chemical design of these new MTV tracers is motivated by the Photo-Activated Non-intrusive Tracing of Molecular Motion (PHANTOMM) technique of Lempert, et al.⁹ PHANTOMM is based on tracers that would otherwise luminesce if not for the attachment of a deactivating group. Current sensors for measuring slow fluid flows employ a laser dye appended to a deactivating group to render a non-emissive assembly. This assembly is de-caged photolytically by a laser pulse to free the luminescent sensor, which can then be tracked indefinitely by simple fluorescence imaging techniques with a second interrogating laser pulse

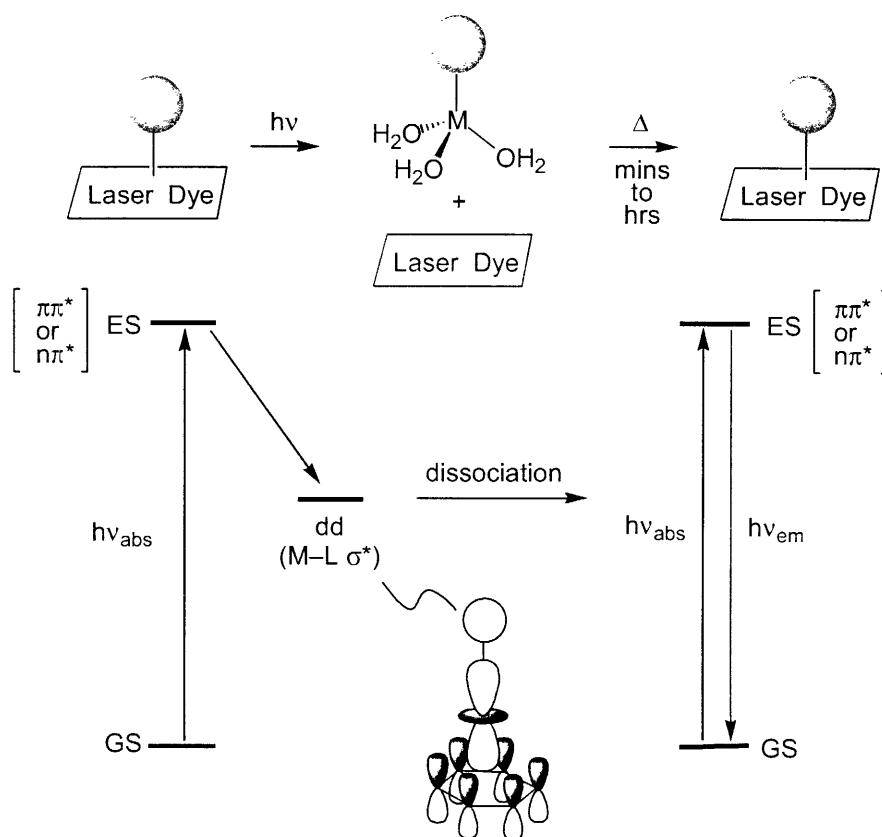


Figure 4.2. The design of reversible “caged” laser dye tracers for application of MTV to very slow flows. The photophysics required for photolytic de-caging of the laser dye is shown below the schematic.

(or other source to illuminate the flow field). Chromophores such as fluorescein and pyrene are covalently appended with methoxynitroaromatic groups, which render the latent fluorescent dye non-emissive. Although clever in design, these sensor systems have limitations including irreversible de-caging that occurs in room light. The luminescent dye is generated by photolytic cleavage of the covalent bond, and this irreversible reaction allows only one measurement per de-activated dye. Moreover, generalization of the strategy to other laser dyes is difficult since the dye functionalities must be compatible with the caging chemistry.

4.1.4 Reversible Caged-Dyes as Tracers for MTV

The problems of the PHANTOMM technique have been addressed by developing new classes of *reversibly* photo-activated dyes that display the time-dependent luminescence needed

Chapter 4

for measuring slow fluid flows and that can be reversibly de-caged. In this design, a tracer dye is freed upon excitation by a “write” laser. Once liberated, dyes can be imaged by its fluorescence, produced upon the delivery of a second excitation pulse from a “read” laser to provide the crucial velocimetry information. Reversible complexation of the dye permits the use of fluorescence based emission, since the tracing is coupled to the photolytic de-caging of the dye.

A schematic representation of the desired photophysics for this system is depicted in Figure 4.2: a metal-based head group (gray circle = L_{head}) with non-emissive, ligand field d-d states short-circuits the emissive $\pi-\pi^*$ excited state of the laser dye in the caged complex. The dye complexed to the metal head-group will not luminesce because the excited state will decay to these low-lying ligand field states. However, if the d-d state is dissociative with respect to the coordinated laser dye (i.e., a metal (d_{z^2})-dye σ^* state), then laser excitation will free the dye from the complex. Upon liberation from the metal head-group, the dye is able to emit upon excitation from a second laser pulse. By uniting the PHANTOMM technique with MTV: (1) the fluid is tagged by the fluorescence grid; (2) long emission lifetimes of the dye are not required (i.e., only where the laser has written a pattern will emission be observed); and (3) oxygen quenching is circumvented since the fluorescent excited state is too short-lived to react with diffusing oxygen. In Figure 4.2, the dye can re-attach to the head group in solution by classical substitution pathways to regenerate the tracer for subsequent measurements. The caging / de-caging timescales may be controlled by varying the electronic properties of the head group and the laser dye.

Of the various L_{head} fragments shown in Figure 4.3, this Chapter will focus specifically on the synthesis and reactivity of laser dye complexes of Cp^*Ru . The Cp^*Ru metal fragments display the requisite arene binding and photophysical properties for such a strategy. The Cp^*Ru head group, comprising an anionic $6e^-$ donor ligand and a Ru^{III} or Ru^{II} metal center, bind aromatic substrates in an η^6 -coordination mode to form 17 and 18 electron species, respectively. As shown in Figure 4.2, photolytic de-caging releases the free dye into solution and water

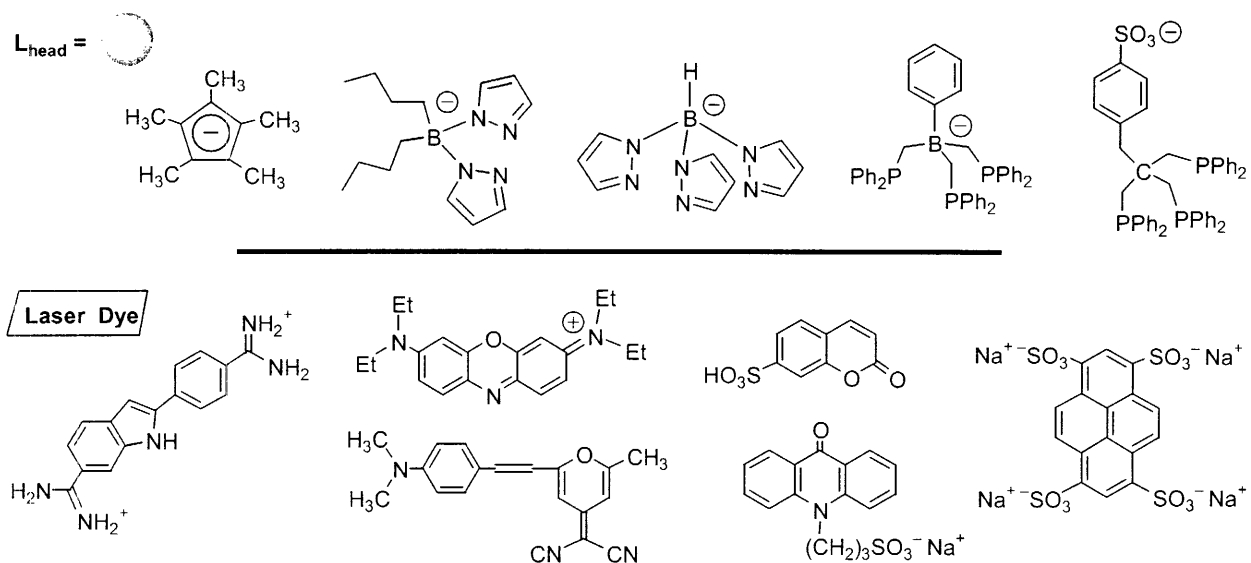


Figure 4.3. Various metal head groups (L_{head}) and laser dye systems that can be implemented in the development of MTV tracers for very slow flows. This chapter will focus on $L_{\text{head}} = \text{Cp}^*$ complexes with Ru and its photochemical and thermal reactivity with a couple laser dyes.

(solvent) substitution occurs at the metal center to form a $[\text{Cp}^*\text{Ru}(\text{OH}_2)_3]^{n+}$ ($n = 1,2$) complex. To reverse the de-caging, the re-attachment of the dye to the metal complex should occur thermally in the absence of light.

The feasibility of the design of Figure 4.2 has previously been established by Mann and co-workers with their studies of CpRu^{II} -arene and aromatic dye complexes.¹⁰⁻¹⁵ In this work, the photochemistry was performed in non-aqueous and weakly coordinating solvents. We have found that the Mann chemistry does not translate to aqueous solution because the $18e^-$ aquo complex, $[\text{CpRu}^{\text{II}}(\text{OH}_2)_3]^+$, produced upon dye liberation is substitutionally inert. The water ligands are inert to substitution by aromatic laser dyes, thus circumventing the regeneration of the original complex. Thus we studied systems in which $L_{\text{head}} = \text{Cp}^*$, where the anionic ligand affects the donor properties of the metal head group. Unlike Cp, the more electron rich Cp^* will serve to labilize the solvent (S) groups of a $[\text{L}_{\text{head}}\text{Ru}^{\text{II}}(\text{S})_3]^+$ complex. Laser dyes are chosen to possess a negative charge or to be neutral, allowing the effect of electric fields on EOF properties to be examined. In addition, a head group attached to a remote part of the π -aromatic system of

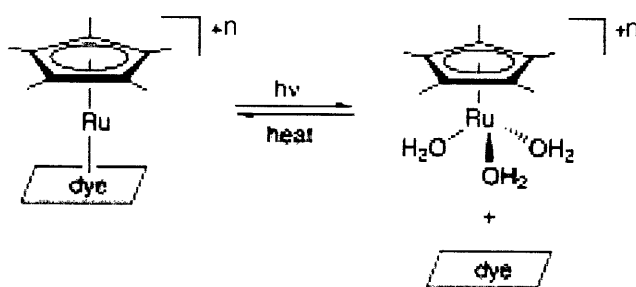
Chapter 4

the dye will not deactivate luminescence. Thus in exploring the chemistry of Figure 4.2, we are cognizant of the need to attach the deactivating metal head group to the dye's arene rings from which luminescence originates. Spectroscopic studies will focus on the timescales for the de-caging event in order to further understand the photophysical properties of these systems. A thorough understanding of the fundamental photophysics leading to de-caging will permit the development of new sensors for monitoring the slow fluid flows of the microdomain.

4.2 Results and Discussion

4.2.1 Synthesis of Ruthenium Arene Complexes

Previous studies in the group using an aqueous solution of the $[\text{Cp}^*\text{Ru}^{\text{III}}(\text{OH}_2)_3]^{2+}$ species with PSA indicated that the reversible caging scheme was possible. The $[\text{Cp}^*\text{Ru}^{\text{III}}(\text{OH}_2)_3]^{2+}$ species is formed by dehalogenation of $[\text{Cp}^*\text{RuCl}_2]_2$ in an acidic environment ($\text{pH} = 2$) to prevent polymerization and formation of the hydroxide derivative, $[\text{Cp}^*\text{Ru}(\text{OH})_2]_2$.¹⁶ A solution of the purported $[\text{Cp}^*\text{Ru}^{\text{III}}(\text{OH}_2)_3]^{2+}$ species, in the presence of excess PSA, is heated to form the “caged” complex assumed by the absence of dye emission. This solution was photolyzed and subsequently heated again, and these studies indicated that the caging process was reversible, as shown in Scheme 4.1. The complexes involved in these experiments were not well-characterized and hard to isolate. This is possibly due to the greater Lewis acidity of Ru^{III} -aquo complexes, which are prone to polymerization.^{17,18} These initial studies suggested that stable model complexes of Ru^{II} can be synthesized since the Ru^{III} species were unstable in solution and tended to oligomerize. In order to ascertain whether the active species involved Ru^{II} or Ru^{III} , $[\text{Cp}^*\text{Ru}^{\text{II}}\text{-dye}]^+$ complexes were prepared and isolated for detailed spectroscopic and photochemical studies in both aqueous and non-aqueous media.



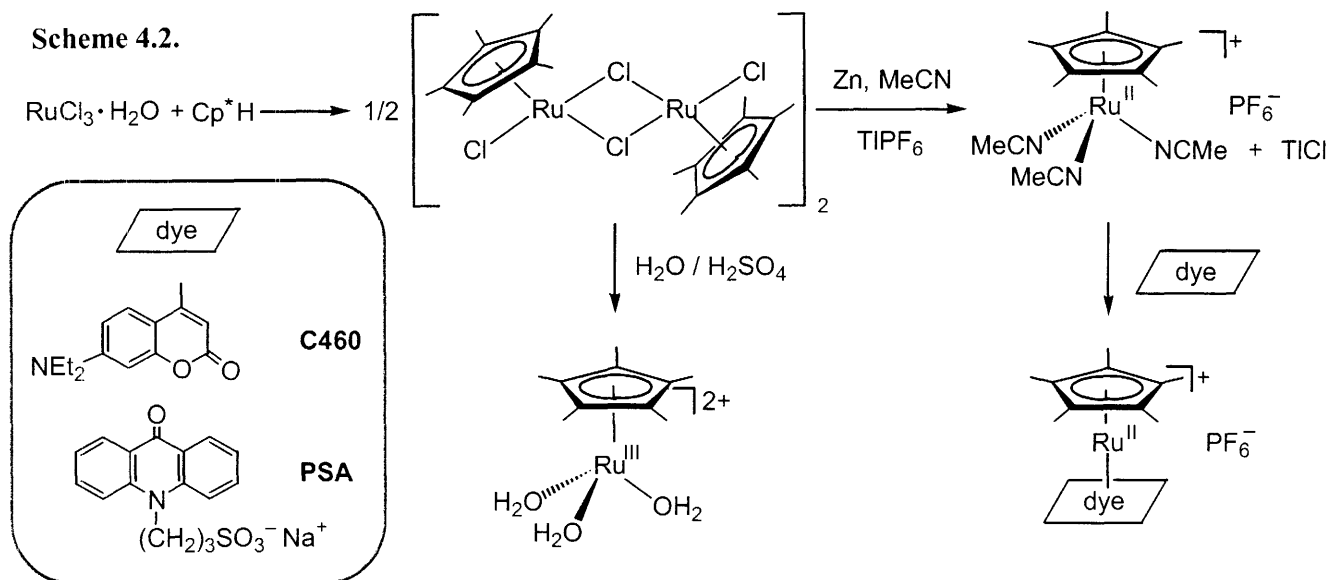
Scheme 4.1. General reaction of the reversible caged dye system where the complexed dye is non-emissive and upon photolysis, the dye is fluorescent upon excitation.

4.2.1.1 [Cp*Ru(NCMe)₃]PF₆ (**5**)

The [Cp*Ru(NCMe)₃]PF₆ (**5**) synthon was chosen as the precursor for the Ru^{II}-arene complexes because the acetonitrile ligands are considerably photolabile.¹⁵ Electrophilic solvento (S) complexes of the [Cp*Ru(S)]⁺ fragment have been prepared from a variety of precursors; these cations are potent but soft electrophiles that are prone to complex to virtually any six electron ligand.¹⁹ Initial syntheses involved stirring the commercially available polymeric precursor [Cp*RuCl]₄ in acetonitrile with AgOTf. The product was a mixture that included a black solid, which was presumed to be due to the reaction between the starting material and trace H₂O to form the cubane [Cp*Ru(OH)]₄ complex.¹⁹ The commercial starting material was determined to be wet, so it was independently synthesized from the reduction of commercially available [Cp*RuCl₂]_n with Super-Hydride. The orange-brown product was then refluxed in acetonitrile with AgOTf, and AgCl was observed to precipitate. However, the desired compound **5** could not be isolated from the brown mixture.

The failure of the above methodology stressed the importance of freshly prepared [Cp*RuCl₂]_n polymer (n = 2) to prevent extended cross-linking over time. Refluxing RuCl₃•H₂O and Cp*H in ethanol was the preferred route to make the extremely hygroscopic [Cp*RuCl₂]₂ starting material.²⁰ Coordinatively unsaturated Ru^{III} species, like [Cp*RuCl₂]₂, are valuable synthons for the generation of Cp*Ru^{II} complexes under mild conditions.^{19,21} The [Cp*RuCl₂]₂ complex typically undergoes ligand substitution reactions at room temperature. However, it appeared from the previous reactions that the polymer precursors were not completely reduced to generate **1** in high yield. A modified preparation of **5** involving Zn as the reducing agent and salt metathesis with TIPF₆ was used.²² The NMR spectrum of the resulting product showed the characteristic broad singlet for acetonitrile protons.

The reactivity of the synthon with simple arenes was tested by adding benzene to a CH₂Cl₂ solution of **5**, since thermally more stable metal-arene bonds are formed in the presence of aromatics. Characterization of this reaction by ¹H NMR indicated complete conversion of **5** to



the $[\text{Cp}^*\text{Ru}(\text{C}_6\text{H}_6)]\text{PF}_6$ product.¹⁵ Ligand exchange studies of **5** in CD_3CN were conducted at room temperature over the course of 1 hr and were monitored by ^1H NMR. The spectra, obtained every 10 min, indicated that the CH_3CN ligands were freely exchanging with the CD_3CN solvent; the acetonitrile lability precluded obtaining a crystal structure of **5**.

4.2.1.2 $[\text{Cp}^*\text{Ru}]^+$ Laser Dye Complexes

Scheme 4.2 summarizes the synthesis and reaction chemistry of the $[\text{Cp}^*\text{Ru}]^+$ complexes detailed below. The clean reaction of benzene with **5** indicated the facile η^6 -coordination of arenes to the $[\text{Cp}^*\text{Ru}]^+$ fragment. Initial laser dye reactivity studies were conducted with the commercially available 7-diethylamino-4-methylcoumarin (Coumarin 460; C460). Mann and co-workers have synthesized a range of $[\text{Cp}^*\text{Ru}(\text{coumarin})]^+$ compounds and it was found that the photolysis of these compounds in acetonitrile generated $\text{Cp}^*\text{Ru}(\text{NCMe})_3^+$ and free coumarin dye.²³ Kinetic measurements of arene displacement of $[\text{Cp}^*\text{Ru}(\eta^6\text{-anthracene})]^+$ vs. $[\text{Cp}^*\text{Ru}(\eta^6\text{-anthracene})]^+$ compounds with acetonitrile resulted in a pseudo-first-order rate constant approximately a factor of 5 smaller for the Cp^* ligated compounds.¹³ An increase in the Ru-arene bond strength or the greater steric restriction of the methyl groups in the Cp^* complexes is probably the cause for the decrease in reactivity (similar for photochemical reactions which is

due to the electronic effects not steric). Therefore, $[\text{Cp}^*\text{Ru}(\text{C460})]\text{PF}_6$ (**6**) compound was synthesized from the reaction of **5** with C460 in dichloromethane. The structural characterization by x-ray diffraction studies shown in Figure 4.4 shows the $[\text{Cp}^*\text{Ru}]^+$ fragment bound with η^6 -coordination to the benzenoid ring of the dye. Selected bond distances for the carbons of the arene ring are listed in Table 4.1, which indicate that the aromaticity is maintained in the solid-state structure (complete ORTEP labeling and structure tables are compiled at the end of this Chapter). The facile replacement of the acetonitrile ligands by the polyaromatic compound required no heat and short reaction times. Complex **6** was also found to be stable in dichloromethane, which is a significantly less donating solvent than CH_3CN . Purification of the compound on diatomaceous earth columns provided successful removal of decomposition products and unreacted starting materials. The ^1H NMR spectrum for compound **6** revealed a characteristic upfield shift of the aromatic protons in C460, allowing complexation to be determined by NMR. The aliphatic protons of the laser dye were slightly shifted ($\delta < 0.1$ ppm), but the aromatic protons were shifted upfield by 0.53 - 0.9 ppm. This net shielding of the arene protons is characteristic of coordination with a $[\text{Cp}^*\text{M}]^+$ group.

Complexes of propylsulfonated acridone (PSA) was subsequently targeted because of the dye's water solubility, which is appropriate for MTV studies in aqueous solutions. The commercially available 9(10H)-acridone was sulfonated in a single step reaction with neat propane sultone, a useful reagent for the derivatization of aliphatic and heterocyclic aromatic amines.^{24,25} The cleanly synthesized PSA was characterized by both ^1H NMR and UV-vis (Figure 4.6b) spectroscopies in aqueous solutions ($\lambda_{\text{abs}} = 390, 410$ nm; $\epsilon = 4.86 \times 10^4 \text{ M}^{-1}\text{cm}^{-1}$). PSA has two potential arene rings to which the $[\text{Cp}^*\text{Ru}]^+$ fragment can bind.

The room temperature reaction of **5** and PSA yielded $[(\text{Cp}^*\text{Ru})_2(\text{PSA})](\text{PF}_6)$ (**7**) whose structural characterization is shown in Figure 4.5. The thermal ellipsoid plot clearly shows η^6 -

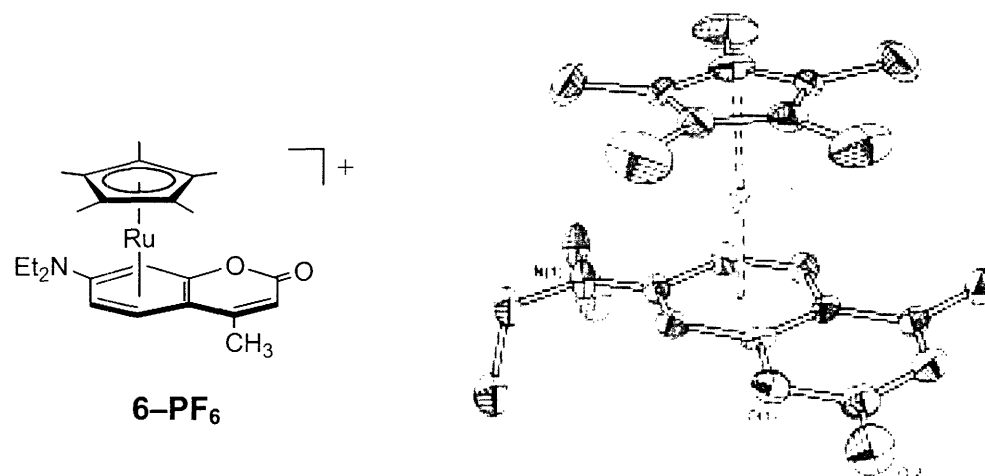


Figure 4.4. Thermal ellipsoid plot (50% probability) of $[\text{Cp}^*\text{Ru}(\text{C460})]^-$ (**6-PF₆**). Solvent molecules, counter anion and hydrogen atoms have been omitted for clarity.

Table 4.1. Selected bond lengths (Å) of the arene (Ar) carbons, $\text{Cp}^*\text{-Ru}$, and Ru-arene of $[\text{Cp}^*\text{Ru}(\text{C460})]^+$ (**6-PF₆**).

C–C Bond Distances in Ar of (6-PF₆) / Å			
C(1)–C(2)	1.429(8)	C(3)–C(4)	1.393(8)
C(1)–C(6)	1.431(8)	C(4)–C(5)	1.399(8)
C(2)–C(3)	1.432(8)	C(5)–C(6)	1.399(8)
Ru–Centroid Bond Distances of (6-PF₆) / Å			
$\text{Cp}^*\text{-Ru}$	1.78(3)	Ru-Ar	1.68(3)

Chapter 4

coordination of the polyaromatic dye to two $[\text{Cp}^*\text{Ru}]^+$ fragments. Formation of a dinuclear species is common as evidenced by the formation of $[(\text{Cp}^*\text{Ru}^{\text{II}})_2(\text{arene})]^{2+}$ (arene = anthracene, phenanthrene, pyrene) complexes, which were only characterized by NMR.²⁶ The carbon bond lengths of both arene rings of PSA, along with the Ru–arene and Cp*–Ru distances are listed in Table 4.2, which show that the aromaticity in the arene rings are retained upon coordination. In the aromatic region of the ^1H NMR spectrum of **7**, all four resonances are shifted upfield (~ 1 ppm) relative to free PSA, allowing spectroscopic confirmation of bound arene. These upfield shifts result from large changes in the π -system of the dye arene rings. Monitoring of the reaction by ^1H NMR showed that dinuclear **7** is preferentially formed. No evidence of the formation of a mono-Cp*Ru analogue of **7** was obtained even when excess dye was present.

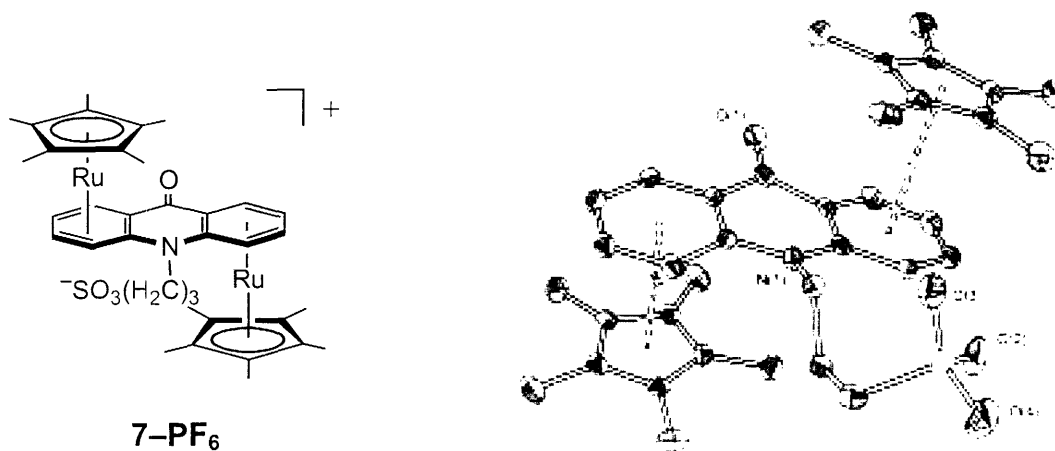


Figure 4.5. Thermal ellipsoid plot (50% probability) for $[(\text{Cp}^*\text{Ru})_2(\text{PSA})]^+$ (**7-PF₆**). For clarity, solvent molecules, counter anion and hydrogen atoms were omitted.

Table 4.2. Selected bond lengths (Å) of the arene (Ar) carbons, Cp*–Ru, and Ru–arene of $[(\text{Cp}^*\text{Ru})_2(\text{PSA})]^+$ (**7-PF₆**).

C–C Bond Distances in Ar of (7-PF₆) / Å			
C(11)–C(12)	1.403(5)	C(13)–C(14)	1.426(5)
C(11)–C(16)	1.404(5)	C(14)–C(15)	1.428(5)
C(12)–C(13)	1.404(5)	C(15)–C(16)	1.433(5)
C(18)–C(23)	1.426(5)	C(20)–C(21)	1.409(5)
C(18)–C(19)	1.430(5)	C(21)–C(22)	1.414(5)
C(19)–C(20)	1.426(5)	C(22)–C(23)	1.397(5)
Ru–Centroid Bond Distances of (7-PF₆) / Å			
Cp*–Ru(1)	1.80(2)	Ru(1)–Ar	1.69(2)
Cp*–Ru(2)	1.80(3)	Ru(2)–Ar	1.70(2)

4.2.2 Electronic Absorption Spectra of Compounds 6 and 7

The electronic structure of free laser dye provides a reference for interpreting the photophysics of **6** and **7**. The UV absorption band of coumarin dyes is assigned as the π - π^* transitions of the aromatic π system, which includes both the pyrone moiety and arene of the dye. C460 has a substituted amino group in the 7-position and the chromophore originates from a polar, intramolecular charge transfer (ICT) excited state.²⁷ This lowest singlet excited state has a large dependence on solvent polarity and the nature of the alkyl substituent on the amine. The ICT transition has a $\lambda_{\text{max}} = 370$ nm in the absorbance spectrum of free C460 in dichloromethane, and the fluorescence maximum is observed at $\lambda_{\text{max}} = 425$ nm. For unbound PSA in acidic aqueous solution, the room temperature UV-vis spectrum exhibits π - π^* transitions at $\lambda_{\text{abs}} = 395$ and 410 nm. A higher energy dye transition is located at 260 nm.

The room temperature UV-vis spectrum of **6** in Figure 4.6a shows one broad transition in the ligand field region with a metal-to-ligand charge transfer (MLCT) band. The MLCT can be described as a $d\pi(\text{Ru})$ - $\pi^*(\text{pyrone})$ transition, and is partially obscured because it occurs at energies similar to other π - π^* transitions of coordinated dye. The higher energy spectral features present for free dye ($\lambda_{\text{abs}} = 250 - 260$ nm) are also evident in the spectrum of **6**; a shoulder is present at 270 nm which can be assigned to a dye based π - π^* transition. No d-d bands of the Ru center were observed, most likely because the weak transitions are obscured by the more intense π - π^* and MLCT bands. Complexation of the C460 benzenoid site to the metal center results in the disappearance of the ICT band at 370 nm, as shown in Figure 4.6a. This is attributed to the partial localization of the π -electrons to form the Ru-arene σ bonds, which destabilizes the polar charge transfer state and disrupts the aromatic conjugation of the dye. The pyrone moiety is now isolated from the π -aromatic interaction and the ICT chromophore is basically replaced by an unsubstituted pyrone that absorbs at 305 nm.²⁸ The extinction coefficient for **6** was determined to be $\epsilon = 1128 \text{ L mol}^{-1} \text{ cm}^{-1}$ ($\lambda_{\text{abs}} = 377$ nm). The room temperature steady state emission spectrum of **6** has relatively no C460 emission at 425 nm (baseline spectrum in Figure 4.7b).

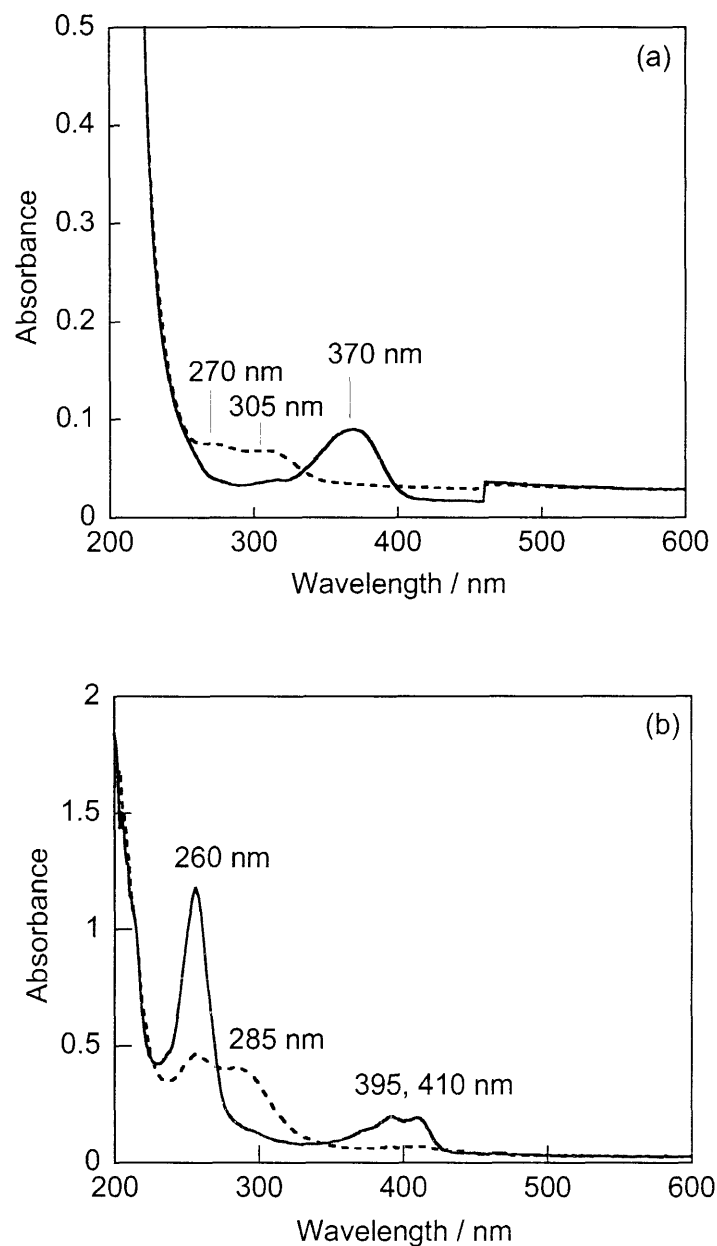


Figure 4.6. (a) UV-vis spectra of free C460 (—); (λ_{\max} = 370 nm) and **6** (---); (λ_{\max} = 270, 305 nm) in dichloromethane. The step in the dye spectrum is due to the lamp crossover at 460 nm. (b) UV-vis spectra of free PSA (—) in acidic aqueous solution (λ_{\max} = 260, 395, 410 nm), and **7** (---); (λ_{\max} = 260, 285 nm).

The room temperature absorbance spectra comparing bound PSA (black) and free dye (red) are shown in Figure 4.6b. For **7**, complexation of PSA results in the disappearance of the low energy dye transitions at $\lambda_{\text{abs}} = 395$ and 410 nm, again indicating that the $[\text{Cp}^*\text{Ru}]^+$ fragments strongly interfere with the dye chromophore. The room temperature UV-vis spectrum of **7** shows a high energy dye-based transition at 260 nm and a weak MLCT band at 285 nm that is not present in the free PSA spectrum. Steady state emission spectra of the complex exhibit relatively weak $\pi-\pi^*$ bands of PSA at the dye-localized transitions of 425 and 450 nm. This is likely due to the presence of the laser dye as an impurity, as a very small amount (0.0001%) in each complex would be sufficient to cause emission to be observed.²³

4.2.3 De-caging Photochemistry of $[\text{Cp}^*\text{Ru}(\text{C460})]\text{PF}_6$ (**6**)

Irradiation of acetonitrile solutions of **6** with UV-vis white light leads to rapid changes in the absorption spectrum, as shown in Figure 4.7a. The photolysis of **6** at the high energy ligand field region ($\lambda_{\text{exc}} = 305$ nm) was monitored by both UV-vis and steady state emission spectroscopies. Displacement of C460 was confirmed by the decrease in the absorbance at 270 and 305 nm and concomitant growth of free dye absorbance at 370 nm. The non-existent dye emission bands in Figure 4.7b are observed to grow immediately upon photolysis. The absorption and emission spectra in Figure 4.7 were taken at various time intervals ($t = 0, 1, 2, 4$ and 15 min), where decomposition was observed at $t = 15$ min with the decrease in free dye transitions. The decomposition is not surprising because of the high flux of UV energy excitation and it is important to note that MTV experiments do not require such long exposure times for flow measurements. These results indicated that the de-caging of the laser dye occurs upon photolysis at the metal centered transition and ligand substitution with the CH_3CN solvent occurs. The quantum yield (Φ_p) determination of the photo-decaging event involved irradiation with lower energy photons to avoid decomposition during photolysis; excitation with 365 nm yielded $\Phi_p = 8.6 \times 10^{-4}$ for the photoreaction. Shifting the excitation wavelength to even lower

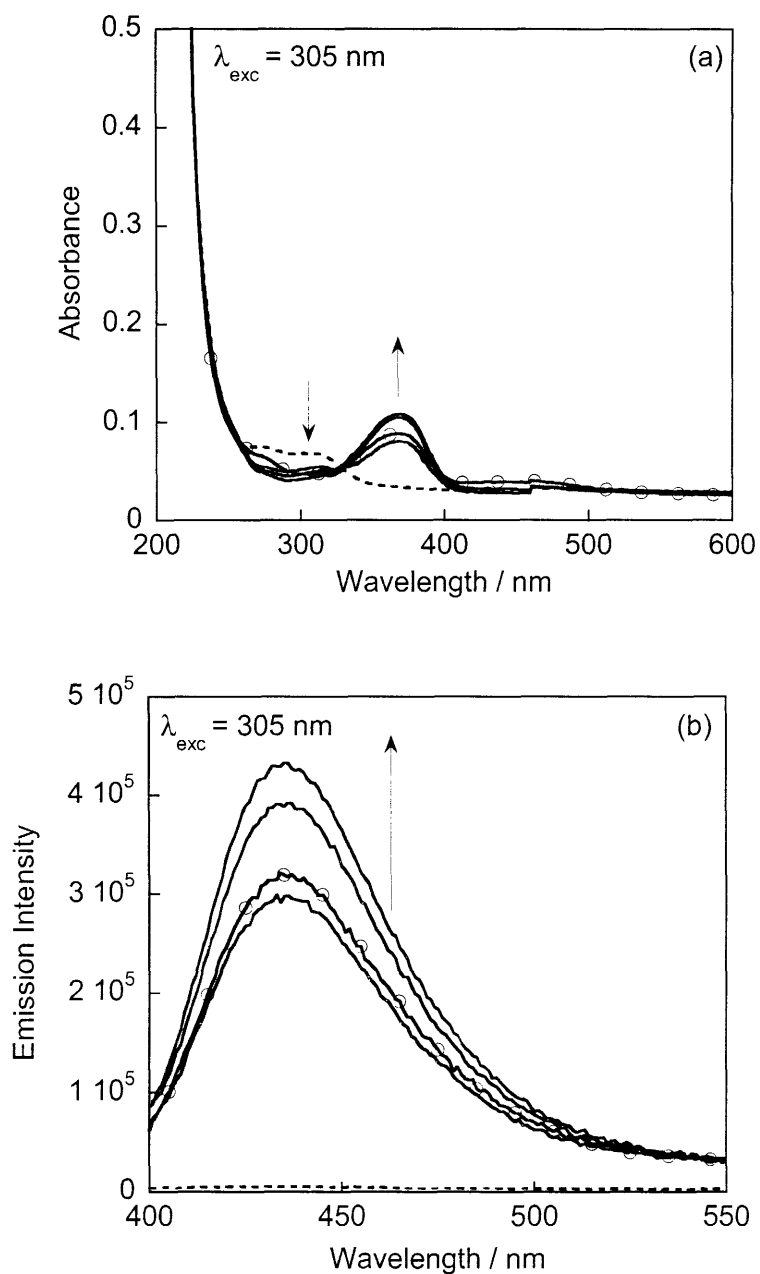


Figure 4.7. (a) Absorbance spectra monitoring photolysis of **6**. Initial spectrum (----) has $\lambda_{\text{abs}} \sim 310$ nm. Upon bulk photolysis with $\lambda_{\text{exc}} > 305$ nm at $t = 1, 2,$ and 4 min, absorbance of free C460 ($\lambda_{\text{abs}} = 370$ nm) appears (—). After $t = 15$ min irradiation (○), decomposition is observed. (b) Accompanying emission spectra of the above photolysis of **6**. Initial spectrum (----) has no C460 emission and upon photolysis, emission at $\lambda_{\text{ems}} = 425$ nm is observed (—). After $t = 15$ min irradiation (○), decrease in C460 emission intensity is apparent.

energy ($\lambda_{\text{exc}} = 405 \text{ nm}$) did not result in the formation of any observable photoproduct as the absorbance spectrum did not change over the course of 30 hours.

4.2.4 De-caging Photochemistry of $[(\text{Cp}^*\text{Ru})_2(\text{PSA})]\text{PF}_6$ (**7**)

Photochemical studies were conducted with white light on samples of **7** in acidic aqueous solutions. Both absorption and emission spectra were taken at one minute intervals to monitor the photoreactions, as shown in Figure 4.8. Immediately upon photolysis with either $\lambda_{\text{exc}} = 305$, 400 or 435 nm, the MLCT band at 285 nm decreased in absorbance with the concomitant increase in free PSA absorbance features centered at 260, 395 and 410 nm. Isosbestic points are maintained in the duration of the photoreaction, indicating clean conversion of **7** to PSA. These results along with the increase in fluorescence intensity in the emission spectra indicate the photolytic de-caging of the dye. Heating of the solutions in the dark at temperatures ranging from 30 - 60 °C did not result in re-complexation of the dye to the $[\text{Cp}^*\text{Ru}]^+$ group. The photolytic decaging of this system appeared to be irreversible, with the presumed formation of a stable $[\text{Cp}^*\text{Ru}^{\text{II}}(\text{OH}_2)_3]^+$ complex.

4.2.5 Reactivity of the $[\text{Cp}^*\text{Ru}^{\text{III}}]^{2+}$ Fragment

The studies mentioned in Section 4.2.1 indicated that the reversible caging process was possible, and thus the initial experiments with Ru^{III} were repeated to determine the active species. It must be emphasized that the aqueous chemistry of $[\text{Cp}^*\text{Ru}(\text{OH}_2)_3]^{n+}$ is complex because of competing oligomerization reactions that form hydroxide-bridged species. The aquo species are also difficult to isolate because of their relatively fast exchange rates in solution.

Free PSA dye was added to an aqueous solution of freshly prepared $[\text{Cp}^*\text{Ru}^{\text{III}}(\text{OH}_2)_3]^{2+}$ with concentrations ranging from 3:1 to 10:1 (Ru : PSA). The absorbance spectrum of the initial mixture is shown in Figure 4.9a (black), and both free dye and MLCT bands are present. Heating these solutions in the dark to 45 °C resulted in a change in the absorbance spectrum shown in

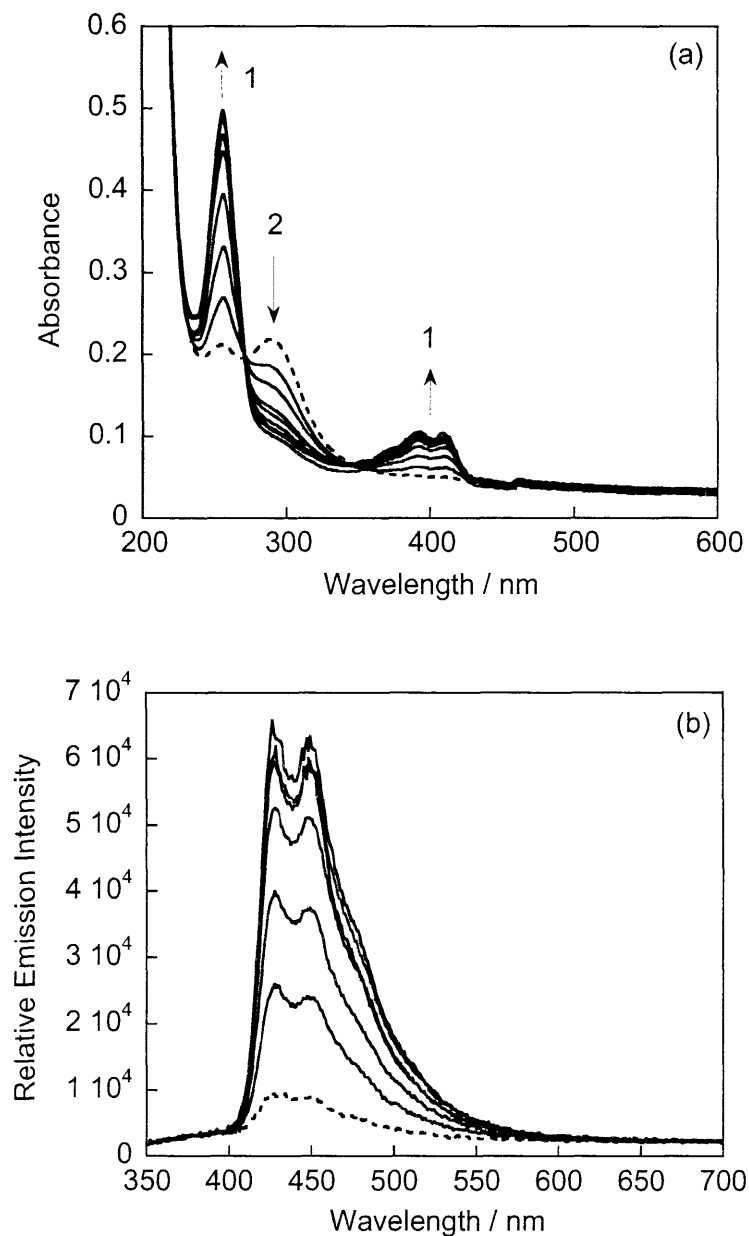


Figure 4.8. (a) Absorbance spectra upon photolysis of **7** at $\lambda_{\text{exc}} = 395$ nm. Initial spectrum (----) exhibits no dye based transitions (1) and has a MLCT transition (2). Subsequent spectra (—) taken at 1min intervals show growth in (1). (b) Accompanying emission spectra for the above photoreaction. Initial spectrum (----) of **7** with growth of PSA fluorescence intensity upon photolysis (—).

Figure 4.9a (red), where the absorption bands at ~ 400 nm attributed to free PSA are not distinguishable from the baseline of the spectrum. Subsequent photolysis of this solution with $\lambda_{\text{exc}} = 435$ nm regenerates the tris-aquo complex and free PSA in solution, as shown in Figure 4.9b. The absorption spectra maintain clean, isosbestic behavior as the PSA transitions increase in absorbance. This heating and photolysis cycle can be repeated to generate Ru^{III} photoproducts, which contrasts with the behavior of the Ru^{II} complex **7**. Difference absorbance spectra of these reactions with excitation at $\lambda_{\text{exc}} = 395$ nm (Figure 4.10a) and $\lambda_{\text{exc}} = 435$ nm (Figure 4.10b) exhibit isosbestic points and further exemplify a clean photolytic de-caging of the PSA dye. The ability to thermally re-complex the laser dye to the metal in this reversible system can be explained by the greater Lewis acidity of the Ru^{III} center.^{18,29} The aromatic dye is a better ligand than water for the electron deficient $[\text{Cp}^*\text{Ru}^{\text{III}}]^{2+}$ fragment, thereby forming a more stable $[\text{Cp}^*\text{Ru}^{\text{III}}(\text{PSA})]^{2+}$ complex in solution. Conversely, the $[\text{Cp}^*\text{Ru}^{\text{II}}]^+$ fragment reacts with water to form the more stable tris-aquo complex, rendering the Ru^{II} de-caging system to be irreversible for **6** and **7**.

The reduction potential of the $\text{Ru}(\text{OH}_2)_6^{3+/2+}$ couple is 0.21 V (vs. SCE).³⁰ The solutions of the $[\text{Cp}^*\text{Ru}(\text{OH}_2)_3]^{2+}$ ion show a reversible signal in the cyclic voltammogram with a reduction potential of roughly 0.07 V (vs. SCE), which correlates well with a reported value.¹⁶ The solutions being slightly more difficult to reduce can be explained by the added electron density from the Cp* ligand to the metal center. The more electrophilic Ru^{III} metal center and the higher water exchange rate for Ru^{III} cations can explain the ability of PSA to re-complex to $\text{Cp}^*\text{Ru}^{\text{III}}$ in solution.

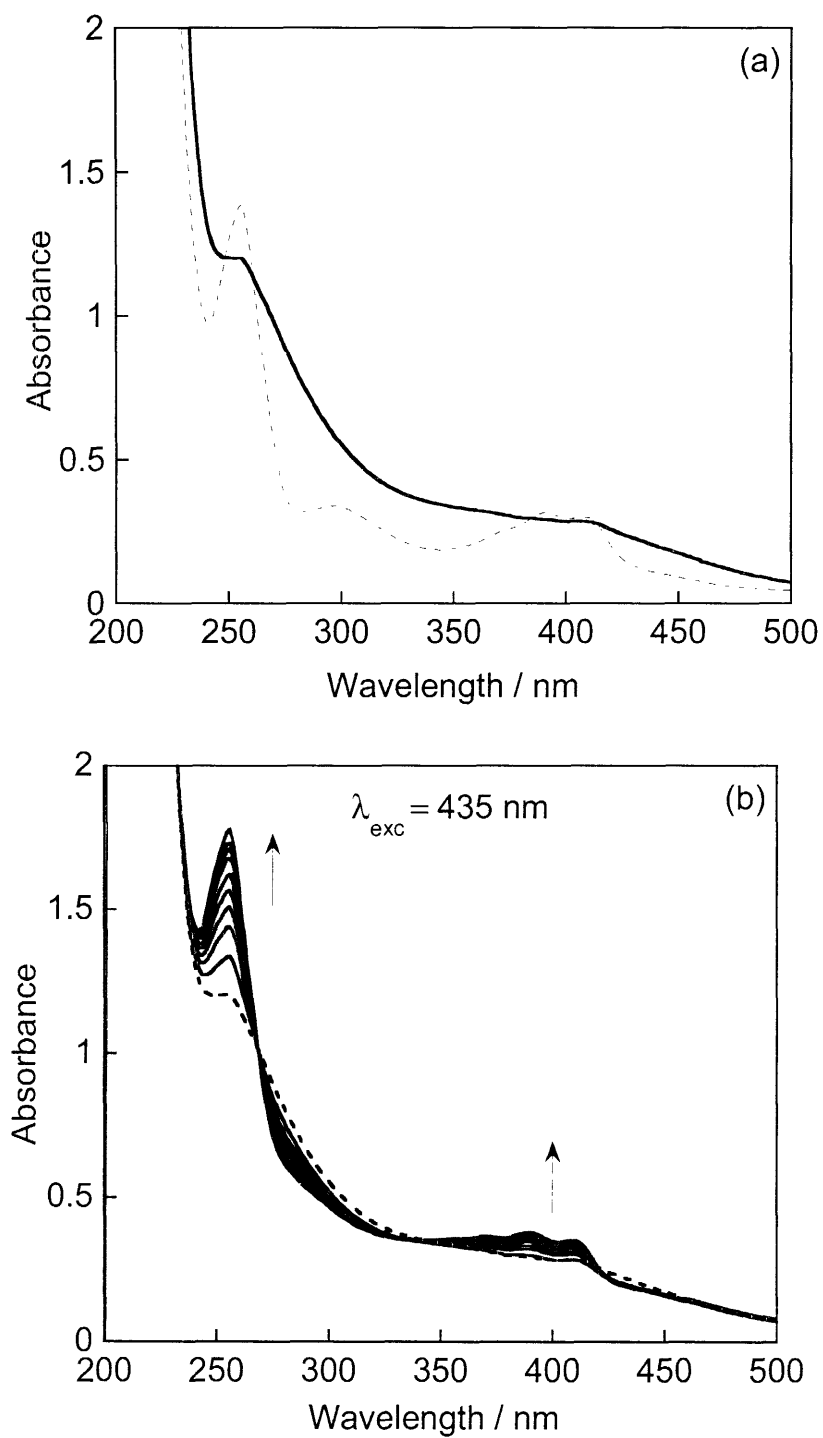


Figure 4.9. (a) Initial UV-vis spectra of a solution of $[\text{Cp}^*\text{Ru}(\text{OH}_2)_3]^{2+}$ + PSA (----), and upon heating of the solution for 30 min at 45 °C (—). (b) Subsequent photolysis λ_{exc} of the heated solution is monitored by UV-vis absorption, and an increase in absorbance of PSA-based transitions is observed.

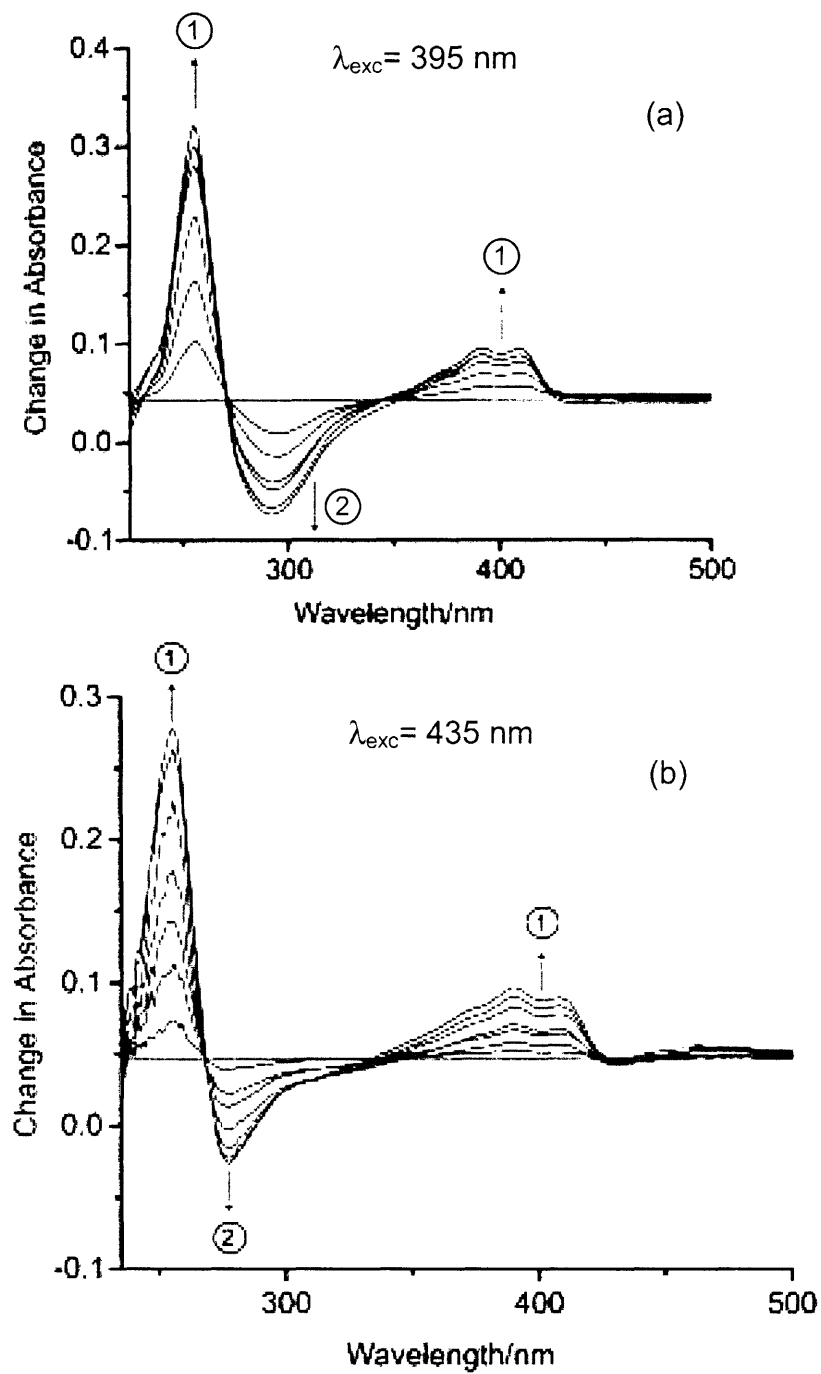


Figure 4.10. (a) Difference absorption spectra for the photolysis of $[\text{Cp}^*\text{Ru}(\text{OH}_2)_3]^{2+} + \text{PSA}$ with $\lambda_{\text{exc}} = 395 \text{ nm}$, and (b) $\lambda_{\text{exc}} = 435 \text{ nm}$.

4.2.6 Electronic Structure Calculations

Density functional calculations were performed on a simplified model of **6**-PF₆ (Cp* = Cp; Et = Me) in order to support the electronic structure description of Section 4.2.1, the tentative assignments of the electronic absorption spectrum presented in Section 4.2.2 and the observed photochemistry. As depicted in Figure 4.11, the HOMO consists of M ($d_{xy}/d_{x^2-y^2}$) π -bonding interaction with Cp and electron density localized on the nitrogen atom of the dye. This is consistent with the ground state picture of coumarin, where the lone pair resides on the nitrogen. The LUMO corresponds to the resonance structure with π -bonding on the pyrone ring and electron density localized on the negatively charged oxygen. The HOMO–LUMO pair complements the photoreactivity of **6**. Photolysis at the ICT transition results in the decay of the excited state to the lower-lying d–d state, as illustrated in Figure 4.2. The LUMO + 1 and LUMO + 2 orbitals also possess predominantly antibonding interaction between the metal d orbitals and π -orbitals of both the Cp and arene of the dye. The degenerate HOMO – 1 and HOMO – 2 orbitals also show significant π -interaction between the metal d-orbitals and the Cp head group, rendering the Ru^{II} center less electrophilic for re-complexation to the aromatic ring of the coumarin dye.

Relevant orbitals from the computational studies of a simplified **7**-PF₆ (Cp* = Cp; –N(CH₂)₃SO₃[–] = –NCH₃) are displayed in Figure 4.12. The localization of the electron density on the nitrogen in the HOMO and the oxygen in the LUMO also indicates the excitation into the ICT of the PSA dye upon photolysis. The HOMO consists of a strongly anti-bonding interaction between the two Ru $d_{x^2-y^2}/d_{xy}$ orbitals and the nitrogen p-orbital of PSA. The LUMO also exhibits strong anti-bonding interaction between the Ru d_{z^2} orbital and delocalized π -bonding on the central PSA ring. About 0.755 eV higher in energy is the LUMO + 1 that also has anti-bonding interaction between the metal $d_{xz/yz}$ and π -orbitals of the central aromatic ring. These electronic structure calculations confirm the photophysics described in Figure 4.2, where the low-lying MLCT states are qualitatively described by the LUMO orbitals.

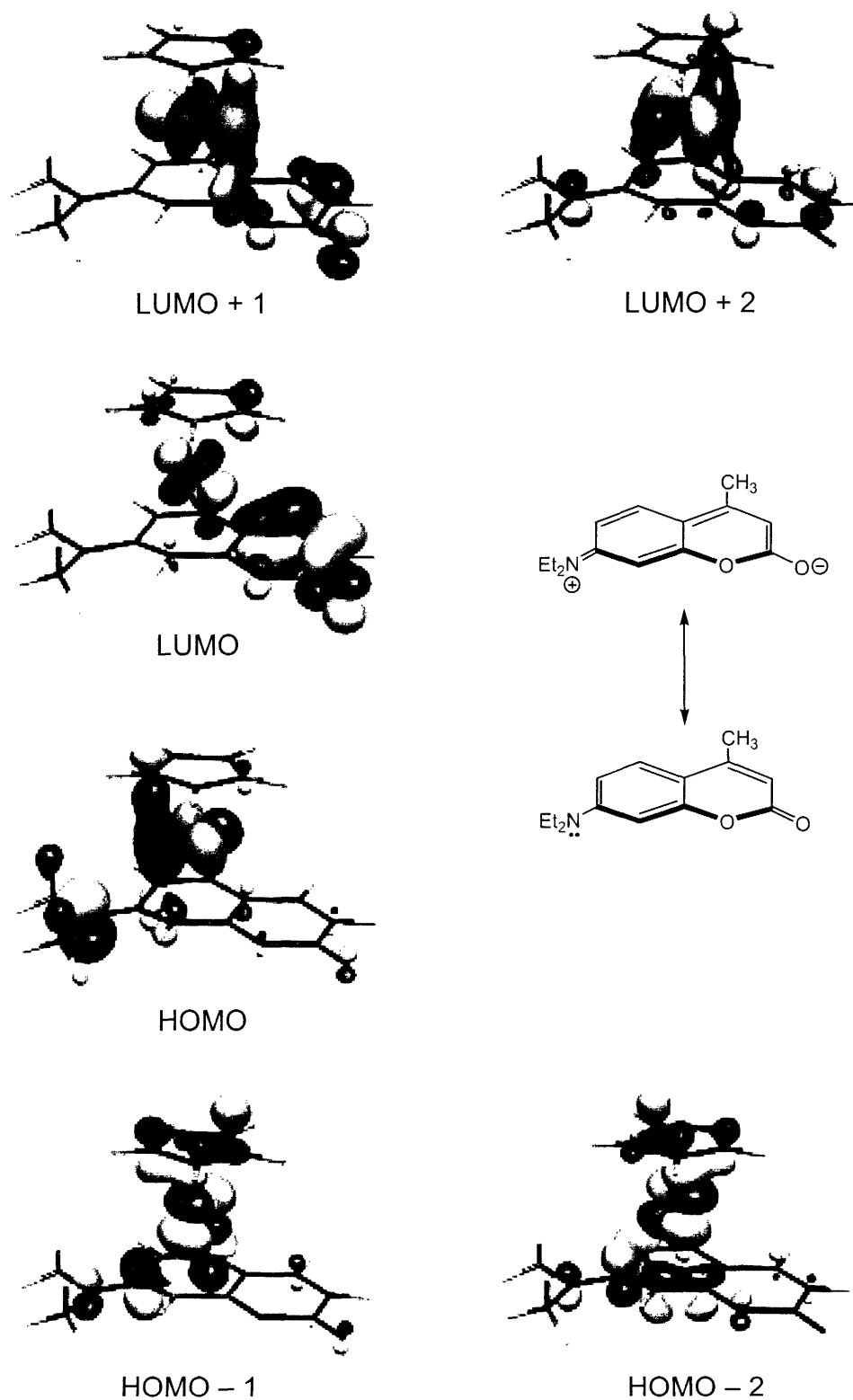
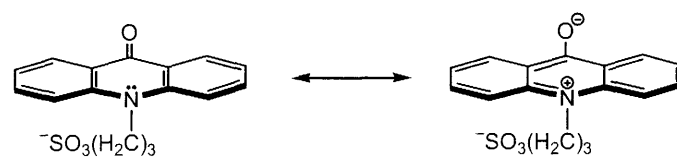
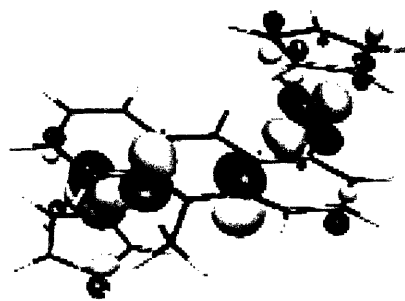


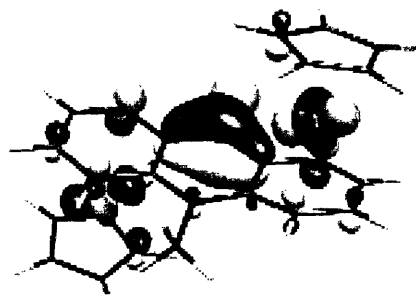
Figure 4.11. Representative orbitals for density functional calculations of 6-PF₆. Schematic of the ICT for C460 dye is shown.



LUMO + 1



LUMO



HOMO

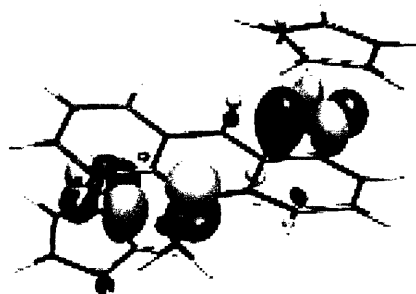


Figure 4.12. Representative orbitals from electronic structure calculations for 7-PF₆.

4.2.7 Time Resolved Spectroscopy

The photochemical experiments imply that Ru^{II} is not likely to be the reactive species in the reversible caged dye system and that Ru^{III} is the active species in the de-caging event. In order to understand these results, ultrafast time-resolved spectroscopy was used to determine the lifetime (τ_0) of the excited states of **7**. An aqueous solution of **7** had a $\tau_0 = 15$ ns, which is comparable to the lifetime measured for free PSA alone in aqueous solution. Since there appears to be no power dependence on the pump beam and two Cp* Ru^+ groups bind to PSA, complex **7** requires two photons to de-cage the dye. Two pulse experiments conducted on the picosecond laser system resulted in a similar lifetime to that from the single pulse measurement ($\tau_0 = 16$ ns). Comparison of the lifetime decay in single pulse vs. two pulse experiments is shown in Figure 4.11a. The time delay between the two laser pump pulses (2 ns) may be too short on the dissociation timescale.

Time-resolved spectroscopic studies of an acidic aqueous solution of [Cp* Ru^{III} (PSA)]⁺ yielded a $\tau_0 = 5.6$ ns. Initial investigations of the kinetics of the reversible Ru^{III} system using both nanosecond and picosecond transient absorption (TA) spectroscopies have been unsuccessful to date. No change in absorbance was observed in the nanosecond experiments. A signal within the 200 - 400 ps range was observed in the picosecond TA studies, but we cannot distinguish between a bleach and photoinduced absorbance. Future picosecond TA experiments will require a good reference standard with an observable transient absorption at 400 nm, and a flow cell so that the sample will not photobleach.

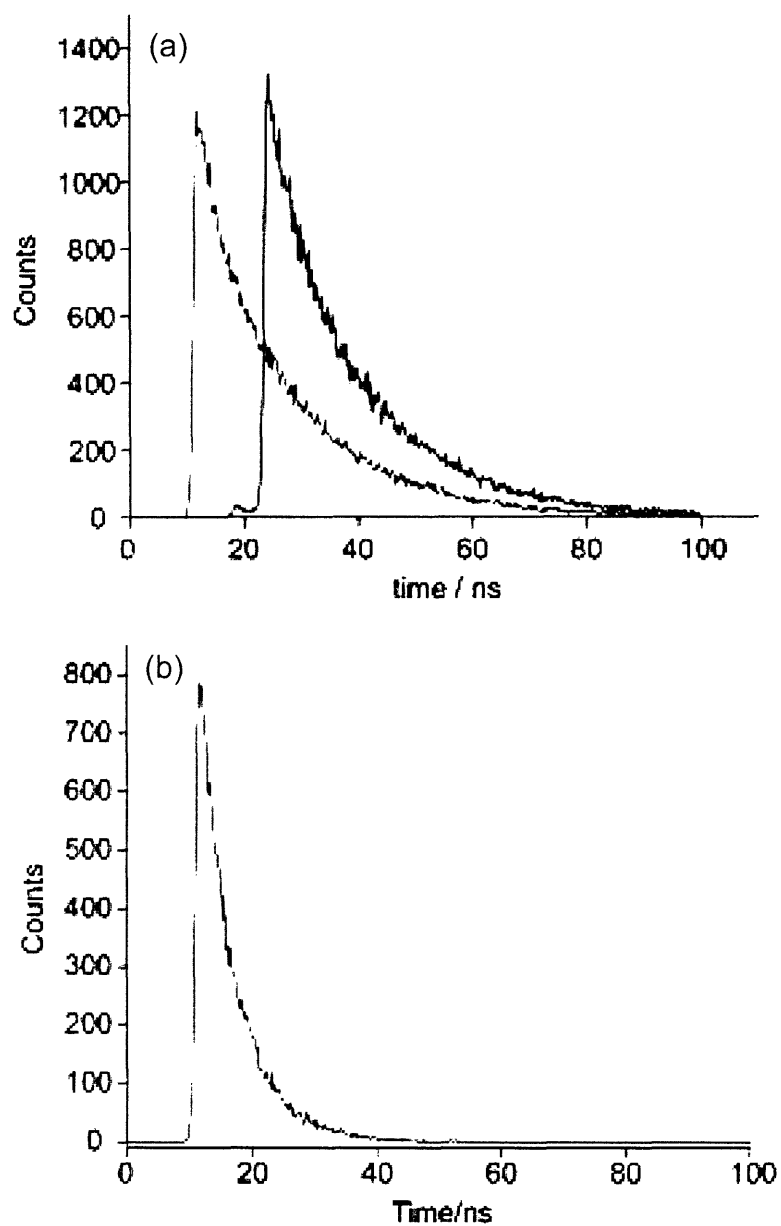


Figure 4.13. (a) Time resolved data for single pulse (left; $\tau_0 = 15.7$ ns) and two pulse (right; $\tau_0 = 16.2$ ns) experiments of 7. (b) Single pulse time resolved measurement of $[\text{Cp}^*\text{Ru}(\text{OH}_2)_3]^{2+}$ + PSA with $\tau_0 = 5.6$ ns.

4.3 Conclusions

The syntheses of two laser dye complexes of the $[\text{Cp}^*\text{Ru}^{\text{II}}]^+$ fragment have successfully been isolated and crystallographically characterized. The arene rings of the C460 and PSA dyes exhibit η^6 -coordination to Ru^{II} . Both compounds **6** and **7** serve as models in the investigation of the de-caging photochemistry of the $[\text{Cp}^*\text{Ru}]^{\text{n}+}$ dye complexes. When **6** and **7** are photolyzed in a coordinating solvent, the de-caging of the dye is observed. Isosbestic points in the absorbance and difference absorption spectra indicate clean conversion to the photoproducts. However, attempts to re-complex the dye thermally for photoreactions of **7** were unsuccessful, thus prompting the photochemical investigation of solutions of $[\text{Cp}^*\text{Ru}^{\text{III}}(\text{OH}_2)_3]^{2+}$ and PSA. The cycle of heating (complexation) / photolysis (de-caging) was repeated for the same samples, and the results indicated that the thermal recombination of the $[\text{Cp}^*\text{Ru}^{\text{III}}]^{2+}$ fragment and dye was possible. The reversibility of the Ru^{III} system is attributed to the quenching of the metal Lewis acidity by the aromatic laser dyes, thus forming more stable dye complexes *in situ* relative to tris-aquo compounds. Future work will require an intensive time-resolved spectroscopic study of $\text{Cp}^*\text{Ru}^{\text{II}}$ and $\text{Cp}^*\text{Ru}^{\text{III}}$ PSA reactions in order to further elucidate the photophysical mechanism by which these systems operate. In addition, the difficulties in isolating Ru^{III} complexes and preventing polymerization in acidic solution can be alleviated by perturbing the steric and electronic influence of the metal head group (L_{head}). Chirik and co-workers have synthesized a family of silylated and alkylated indenyl ligands and studied the steric and electronic effects on Zr and Fe sandwich complexes relative to Cp_2Zr and Cp_2Fe .³¹ The effects on ferrocene potentials by Cp replacement with either a silylated indenyl (formally electron withdrawing) or alkylated indenyl (electron donating) are largely dominated by steric bulk of the head groups. Isolation of $[(\text{L}_{\text{head}})\text{Ru}^{\text{III}}(\text{PSA})]^+$ complexes can be attempted by preparing tri-substituted indenyl Ru^{III} compounds that have similar inductive effects as Cp^* , where the bulky ligand prevents association with other species in solution and the electronic effects of the head group allows for the isolation of a stable $[\text{L}_{\text{head}}\text{Ru}^{\text{III}}(\text{dye})]^{\text{n}+}$ complex.

4.4 Experimental

4.4.1 General Synthetic Procedures

All synthetic manipulations were conducted under air and moisture-free conditions using standard Schlenk-line techniques or a nitrogen-filled glove box. Reagent grade solvents were dried by following standard procedures, and degassed OmniSolv water was used to prepare aqueous solutions. NMR solvents (Cambridge Isotope Laboratories) were either dried using appropriate agents and degassed by freeze-pump-thaw cycles, or used as received in glass ampoules. The Ru precursors were obtained from Strem Chemicals, and all other starting materials were from Sigma Aldrich. All materials were used as received.

4.4.2 Physical Methods

All NMR spectra were collected at the MIT Department of Chemistry Instrumentation Facility (DCIF) on a Varian Mercury 300 or Varian Unity 300 Spectrometer at 25 ± 2 °C. Chemical shifts are reported using the standard δ notation in ppm. ^1H spectra were referenced to residual solvent peaks. Electrochemistry was performed on a standard three-electrode configuration using a CV-50W potentiostat (Bioanalytical Systems). The working electrode was Pt, the auxiliary electrode was a Pt wire, and the reference was an Ag/AgCl electrode that was externally referenced to saturated KCl ($E^\circ = 0.197$ vs NHE).

4.4.3 Photochemical Procedures

Photochemistry was performed on samples contained within cells equipped with a solvent reservoir and a 1 cm clear fused-quartz cuvette (Starna Cells). These cells allowed isolation of solvent from the sample with Teflon valves, and were adapted to be evacuated on a high-vacuum line. The excitation source was an Oriel 1000-W Hg/Xe high-pressure lamp. The two inch collimated irradiation beam passed through a distilled water filter to remove the infrared wavelengths and longpass wavelength filters prior to focusing and collimation of the

light onto the sample. Photoreaction progress was monitored by absorption spectra recorded on a Spectral Instruments CCD Array UV-vis instrument or on an OLIS-modified CARY-17 Spectrophotometer. The cut-off filters were replaced with 10 nm bandpass Hg line interference filters to select specific light energies for quantum yield measurements. The light flux used for quantum yield determination at a given wavelength was taken as the average of measurements taken using the standard ferrioxalate actinometer before and after sample irradiation.³² Photoreaction progress for quantum yield experiments was monitored on a scanning wavelength Aviv 17DS Spectrophotometer.

4.4.4 Spectroscopic Methods

Steady-state emission spectra were recorded on a custom-built, high-resolution spectrometer at MIT. A 200 W Hg-Xe arc lamp (Ushio) mounted in an Oriel 60100 lamp housing (f/4) is focused on the entrance slit of a Spex 1680 double monochromator (0.22 m, f/4). The excitation light is collimated by a f/4 fused silica lens, then focused onto the sample with a f/2 fused silica lens. The emitted light is collected at 90° to the excitation beam with a f/2 fused silica lens, then focused by a second lens (f/8) through a Corion colored glass long-pass cut-off filter onto an entrance slit of a Spex 1870B scanning monochromator (f/8). The dispersed emission is detected by a blue-sensitive R943-02 PMT (Hamamatsu), cooled to -40 °C in a Products for Research TE241RF housing powered by a Bertan Associates model 215 high voltage power supply. The signal from the PMT is then passed to a Stanford Research Systems SR400 two-channel photon counter phase-matched to a reference signal generated by a light chopper placed between the excitation monochromator and the sample that is controlled by a Stanford Research Systems SR540, and runs at a frequency of 13 Hz or 338 Hz (short-lived emission). The output from the photon counter is fed through a GPIB interface to a computer, where emission spectra are corrected as a function of wavelength sensitivity for the PMT and instrument response using a point-by-point multiplication of the raw data with a correction data file generated using a NBS standard lamp. The emission spectrometer was scanned across the

Chapter 4

width of the emission spectra at a rate of approximately 1 nm per second. Data acquisition is performed using LabView 5.0 software. All spectra and measurements were obtained at room temperature (25 ± 2 °C).

Nanosecond transient absorption (TA) spectra were collected for samples excited with the output from a Coherent Infinity XPO tunable laser source with a 7 ns bandwidth. The Infinity Nd:YAG laser system consists of an internal diode pumped, Q-switched, oscillator, which provides the seed pulse for a dual rod, single lamp, amplified stage. The pump beam was doubled to 400 nm. Absorption spectra were then recorded by passing white light through the excited sample, which was then collected by an intensified CCD camera.

Data collection for timescales < 7 ns required use of a sub-picosecond laser system, where the excitation pulses are generated from the second harmonic of a 1 kHz Ti:Sapphire regenerative amplifier system (Alpha 1000S, BM Industries). The amplifier is seeded by 130 fs pulses from a 76 MHz passively mode-locked Ti:Sapphire oscillator (Mira 900-F, Coherent) pumped with second harmonic radiation from a solid state diode-pumped YAG laser at 532 nm (Verdi, Coherent). The regenerative amplifier is pumped with 400 ns pulses at 1 kHz from a Nd:YLF laser (BMI 621-D). Chirped pulses from the oscillator are injected into the regenerative amplifier cavity where they are amplified over several passes. Pulses are then compressed in a grating compressor to 100 – 200 fs pulses at ca. 800 nm. In this case, both pump and probe beams derive from the doubled 800 nm source output of the Nd:YLF. Time resolution was obtained by delaying the probe beams with an optical delay stage. Time-resolved fluorescence spectroscopy also required use of the same sub-picosecond laser instrument coupled to a Hamamatsu Streak Camera capable of 50 ps resolution and a Triax 320 monochromator. Single pulse experiments used 400 nm pump beams and two pulse experiments used 305 and 400 nm pump beams. Time-resolved data was fit with Origin 6.0.

4.4.5 Crystallographic Procedures

Crystals were removed from the supernatant liquid and transferred onto a microscope slide coated with Paratone N oil. X-ray diffraction data were collected on a Siemens 3-circle platform diffractometer equipped with a CCD detector. Measurements were carried out at $-90\text{ }^{\circ}\text{C}$ using Mo $K\alpha$ ($\lambda = 0.71073\text{ \AA}$) radiation, which was wavelength selected with a single crystal graphite monochromator. Four sets of data were collected using ω scans and a -0.3° scan width. The data frames were integrated to hkl /intensity and final unit cells were calculated by using the SAINT program v4.050 (Siemens Industrial Automation, Inc.) in conjunction with standard difference Fourier techniques. The structures were solved and refined by direct methods (SHELXTL v6.10, Sheldrick, G. M.; Siemens Industrial Automation, Inc., 2000).

4.4.6 Computational Details

Calculations were performed within the Gaussian 98 program suite.³³ DFT calculations were carried out using the three parameter hybrid functional of Becke along with the correlation functional of Lee, Yang, and Parr (B3LYP).^{34–36} The default “extrafine” grid was used throughout. All models were geometrically optimized to self-consistency. Relativistic effective core potentials were used for Ru along with the standard Hay–Wadt³⁷ double- ξ basis set, augmented by the optimized Ru 5p-function of Couty and Hall.³⁸ The 6-31G(d,p) basis of Pople and co-workers^{39,40} was applied to all other atoms. No attempts have been made to correct for effects of solvation. All calculations were spin-restricted, and geometry optimizations proceeded without imposed symmetry. Canonical Kohn-Sham orbitals were imaged with the program Molekel;^{41,42} default isodensity values were applied.

4.4.7 Preparation of Propylsulfonated Acridone (PSA)

The sulfonated acridone dye was synthesized by stirring 9(10H)-acridone (1 g, 5.12 mmol) and NaH (0.25 g, 10.24 mmol) in 25 ml DMF for 2 hrs at room temperature. Excess propane sultone (1.5 g, 12.28 mmol) was then added and the orange-yellow reaction mixture was

heated at 60 °C for 5 hrs. After rotary evaporation, the oily residue was recrystallized from 95% ethanol as a pale yellow microcrystalline solid (1.45 g, 86% yield). ^1H NMR (300 MHz, D_2O) δ / ppm: 7.74 (dd, 2H, 8.1 Hz, 1.8 Hz, Ar-H), 7.45 (td, 2H, 3.3 Hz, 1.8 Hz, Ar-H), 7.20 (d, 2H, 8.7 Hz, Ar-H), 6.95 (t, 2H, 7.8 Hz, Ar-H), 3.89 (br t, 2H, N- CH_2), 2.80 (t, 2H, 6 Hz, $-\text{CH}_2\text{CH}_2\text{CH}_2-$), 1.80 (br t, 2H, $-\text{CH}_2\text{CH}_2\text{CH}_2-$).

4.4.8 Preparation of $[\text{Cp}^*\text{Ru}(\text{NCMe})_3]\text{PF}_6$ (5)

Initial attempts to synthesize the $[\text{Cp}^*\text{Ru}(\text{NCMe})_3]\text{PF}_6$ synthon involved refluxing the commercially available $[\text{Cp}^*\text{RuCl}]_4$ starting material (Strem Chemicals) in acetonitrile for 2 hrs., followed by salt metathesis with AgPF_6 or AgOTf . The product was recrystallized multiple times with ether to yield an impure brown-yellow solid. The $[\text{Cp}^*\text{RuCl}]_4$ starting material was dark red-black indicating water initiated polymerization. Attempts to synthesize the $[\text{Cp}^*\text{RuCl}]_4$ precursor from the reduction of $[\text{Cp}^*\text{RuCl}_2]_n$ (0.5 g) with $\text{LiB}(\text{Et})_3\text{H}$ (1.63 ml) in 5 ml THF yielded impure dark red-brown solid.

The starting material $[\text{Cp}^*\text{RuCl}_2]_2$ was prepared by reacting Cp^*H (1.5 g, 11.09 mmol) with $\text{RuCl}_3 \cdot n \text{H}_2\text{O}$ (1 g, 4.82 mmol) in 60 ml refluxing methanol.⁴³ The reaction went through a mixed valent blue-green intermediate, and upon completion, the mixture was chilled to -80 °C before being filtered. The obtained solid was dried *in vacuo* and washed twice with cold pentane to remove Cp^*_2Ru . Characterization of the paramagnetic compound (31% yield) by ^1H NMR in CD_2Cl_2 indicated the presence of a broad singlet resonance at $\delta = 6.8$ ppm.

Following a modified literature preparation, $[\text{Cp}^*\text{Ru}(\text{NCMe})_3]\text{PF}_6$ was prepared by zinc (0.1 g) reduction of $[\text{Cp}^*\text{RuCl}_2]_2$ (0.25 g) in 25ml acetonitrile, followed by salt metathesis with TIPF_6 (0.43 g). The solvent was removed *in vacuo*, and the yellow-brown solid was extracted with CH_2Cl_2 and filtered through a Celite column. The solvent was stripped and the product was recrystallized from methylene chloride and diethyl ether to afford the product as a mustard yellow solid. To further purify the compound, it was suspended in hexanes and the solution was

sonicated. It was subsequently washed with rigorously dried THF and hexane to yield a bright yellow microcrystalline solid. ^1H NMR (300 MHz, CD_2Cl_2) δ / ppm: 2.3 (br s, 9H, CH_3CN), 1.6 (s, 15H, C_5Me_5).

4.4.9 Preparation of $[\text{Cp}^*\text{Ru}(\text{C}_6\text{H}_6)]\text{PF}_6$

Three drops of benzene was added to a dichloromethane (2 ml) solution of **5** (0.02 g). The reaction was stirred at room temperature for 3 hours, and the pale yellow solution was filtered and recrystallized with diethyl ether to yield a white solid. The product was characterized by ^1H NMR spectroscopy and the resonances correspond to literature values. ^1H NMR (300 MHz, $(\text{CD}_3)_2\text{CO}$) δ / ppm: 6.06 (s, 6H, C_6H_6), 2.08 (s, 15H, C_5Me_5).

4.4.10 Preparation of $[\text{Cp}^*\text{Ru}(\text{C460})]\text{PF}_6$ (**6**)

Arene complexation was carried out using modified literature procedures.^{23,44} The synthon $[\text{Cp}^*\text{Ru}(\text{NCMe})_3]\text{PF}_6$ (40 mg) was dissolved in methylene chloride in a foil-wrapped scintillation vial to prevent dissociation in room light. A coumarin dye, 7-diethylamino-4-methylcoumarin (C460; Lambda Physik) was dissolved in 5 ml CH_2Cl_2 and was added dropwise to **5** at room temperature. The orange-brown reaction mixture was stirred at room temperature for 2 hrs, filtered and stripped of solvent. The crude product was redissolved in CH_2Cl_2 and equilibrated onto a Celite pipet column. After elution with pentane, the remaining compound was washed down with methylene chloride. The methylene chloride fraction was concentrated, and upon slow diffusion of diethyl ether, yellow crystals were obtained. ^1H NMR (300 MHz, CD_2Cl_2) δ / ppm: 6.45 (q, 1H, 1.5 Hz, ArH), 6.07 (d, 1H, 6.3 Hz, ArH), 5.57 (d, 1H, 1.8 Hz, ArH), 5.42 (dd, 1H, 6.6 Hz, 1.8 Hz, ArH), 3.35 (q, 4H, 7.2 Hz, N- CH_2), 2.35 (d, 3H, 1.5 Hz, CH_3), 1.78 (s, 15H, C_5Me_5), 1.26 (t, 6H, 7.2 Hz, N- CH_2CH_3).

4.4.11 Synthesis of $[(\text{Cp}^*\text{Ru})_2(\text{PSA})]\text{PF}_6$ (7)

PSA (0.1 g, 0.3 mmol) was added to a methylene chloride solution of $[\text{Cp}^*\text{Ru}(\text{NCMe})_3]\text{PF}_6$ (0.15 g, 0.3 mmol) at room temperature and in the dark to prevent dye dissociation. PSA is relatively insoluble in methylene chloride, but the reaction time was extended until the solution turned yellow-brown in color. The unreacted dye was filtered off and the solvent was stripped to yield yellow-brown solid. A water solution of the crude product was then eluted down a diatomaceous earth column. After equilibration for an hour, the caged-dye complex was obtained by eluting with methylene chloride and ether. The PSA complex was recrystallized from 95% ethanol to obtain yellow crystals. ^1H NMR (300 MHz, CD_2Cl_2) δ / ppm: 6.55 (d, 2H, 6.52 Hz), 6.47 (d, 2H, 6.19 Hz), 6.15 (t, 2H, 6.19 Hz, 5.87 Hz), 5.97 (t, 2H, 5.87 Hz), 2.98 (t, 2H, 6.84 Hz, 5.54 Hz), 2.8 (bs, 2H), 2.65 (bs, 2H), 1.54 (s, 30H, C_5Me_5).

4.4.12 Preparation of $[\text{Cp}^*\text{Ru}(\text{OH}_2)_3](\text{PF}_6)_2$ Solutions

The $[\text{Cp}^*\text{RuCl}_2]_2$ starting material was synthesized following the procedure stated above in Section 4.4.8. The dimer (0.1 g, 0.163 mmol) and TlPF_6 (0.113 g, 0.323 mmol) were dissolved in ~50 ml of $\text{H}_2\text{O}/\text{H}_2\text{SO}_4$ (pH = 2) and the orange solution was stirred at room temperature for 2 days until the precipitation of TlCl was observed. The solution was filtered and used as prepared.¹⁶

4.5 References

1. Adrian, R. J. *Annu. Rev. Fluid Mech.* **1991**, *23*, 261.
2. Gendrich, C. P.; Koochesfahani, M. M.; Nocera, D. G. *Exp. Fluids* **1997**, *23*, 361.
3. Stier, B.; Koochesfahani, M. M. *Exp. Fluids* **1999**, *26*, 297-304.
4. Koochesfahani, M. M.; Cohn, R.; MacKinnon, C. *Meas. Sci. Technol.* **2000**, *11*, 1289.
5. Santiago, J. G.; Wereley, S. T.; Meinhart, C. D.; Beebe, D. J.; Adrian, R. J. *Exp. Fluids* **2001**, *25*, 316.
6. Meinhart, C. D.; Wereley, S. T.; Santiago J. G. *Exp. Fluids* **1999**, *27*, 414.
7. Guilkey, J. E.; Gee, K. R.; McMurtry, P.A.; Klewicki, J. C. *Exp. Fluids* **1996**, *21*, 237.
8. Murov, S. L. *Handbook of Photophysics*; Marcel-Dekker: New York, 1993.
9. Lempert, W. R.; Magee, K.; Ronney, P.; Gee, K. R.; Haugland, R. P. *Exp. Fluids* **1995**, *18*, 249.
10. Koefod, R. S.; Mann, K. R. *Inorg. Chem.* **1991**, *30*, 541-548.
11. Koefod, R. S.; Mann, K. R. *Inorg. Chem.* **1991**, *30*, 2221-2228.
12. Mann, K. R. et al *Pure Appl. Chem.* **1995**, *67*, 95-101.
13. McNair, A. M.; Mann, K. R. *Inorg. Chem.* **1986**, *25*, 2519-2527.
14. Schrenk, J. L.; Mann, K. R. *Inorg. Chem.* **1986**, *25*, 1906-1908.
15. Schrenk, J. L.; McNair, A. M.; McCormick, F. B.; Mann, K. R. *Inorg. Chem.* **1986**, *25*, 3501-3504.
16. Koelle, U.; Kläui, W. *Z. Naturforsch.* **1991**, *46b*, 75-83.
17. Stebler-Rothlisberger, M.; Hummel, W.; Pittet, P.-A.; Burgi, H.-B.; Ludi, A.; Merbach, A. E. *Inorg. Chem.* **1988**, *27*, 1358-1363.
18. Koelle, U. *Coord. Chem. Rev.* **1994**, *135-136*, 623-650.
19. Koelle, U. *Chem. Rev.* **1998**, *98*, 1313-1334.
20. Oshima, N.; Suzuki, H.; Moro-Oka, Y. *Chem. Lett.* **1984**, 1161.

Chapter 4

21. Koelle, U.; Kossakowski, J. *J. Chem. Soc., Chem. Commun.*, **1988**, 8, 549-551.
22. Steinmetz, B.; Schenk, W. A. *Organometallics* **1999**, 18, 943.
23. Koeford, R. S.; Mann, K. R. *Inorg. Chem.* **1989**, 28, 2285-2290.
24. Allen, C. F. H.; Murphy, C. F.; Yoerger, W. E. *Anal. Chem.* **1965**, 37, 156.
25. Kondo, K.; Aoi, H.; Takemoto, K. *Synth. Commun.* **1980**, 10, 267.
26. Koelle, U.; Wang, M. H. *Organometallics* **1990**, 9, 195.
27. Drexhage, K. H. *Topics in Appl. Phys.* **1973**, 1, 144.
28. Song, P.; Gordon, W. H., III *J. Phys. Chem.* **1970**, 74, 4234.
29. Luginbuhl, W.; Zbinden, P.; Pittet, P. A.; Armbruster, T.; Burgi, H.-B.; Merbach, A. E.; Ludi, A. *Inorg. Chem.* **1991**, 30, 2350.
30. Bernhard, P.; Lehmann, H.; Ludi, A. *J. Chem. Soc., Chem. Commun.* **1981**, 1216.
31. Bradley, C. A.; Flores-Torres, S.; Lobkovsky, E.; Abruña, H. D.; Chirik, P. J. *Organometallics* **2004**, 23, 5332.
32. Murov, S. L.; Carmichael, I.; Hug, G. L. *Handbook of Photochemistry*, 2nd ed.; Marcel Dekker: New York, 1993.
33. Frisch, M. J., et al. *Gaussian 98*, revision A.9; Gaussian, Inc.: Pittsburgh, PA, 1998.
34. Becke, A. D. *J. Chem. Phys.* **1993**, 98, 5648.
35. Lee, C.; Yang, W.; Parr, R. G. *Phys. Rev. B.* **1988**, 37, 785.
36. Miehlich, B.; Savin, A.; Stoll, H.; Preuss, H. *Chem. Phys. Lett.* **1989**, 157, 200.
37. Hay, P. J.; Wadt, W. R. *J. Chem. Phys.* **1985**, 82, 270-283, 284-298, 299-310.
38. Couty, M.; Hall, M. B. *J. Comput. Chem.* **1996**, 17, 1359.
39. Hariharan, P. C.; Pople, J. A. *Theor. Chim. Acta* **1973**, 28, 213.
40. Francl, M. M.; Pietro, W. J.; Hehre, W. J.; Binkley, J. S.; Gordon, M. S.; DeFrees, D. J.; Pople, J. A. *J. Chem. Phys.* **1982**, 77, 3654.
41. Flükiger, P.; Lüthi, H. P.; Portmann, S.; Weber, J. *MOLEKEL 4.3*; Swiss Center for Scientific Computing: Manno, Switzerland, 2000-2002.

Chapter 4

42. Portmann, S.; Lüthi, H. P. MOLEKEL: An Interactive Molecular Graphics Tool. *Chimia* **2000**, *54*, 766.
43. Tilley, T. D.; Grubbs, R. H.; Bercaw, J. E. *Organometallics* **1984**, *3*, 274.
44. Gill, T. P.; Mann, K. R. *Organometallics* **1982**, *1*, 485-488.

Appendix

Appendix

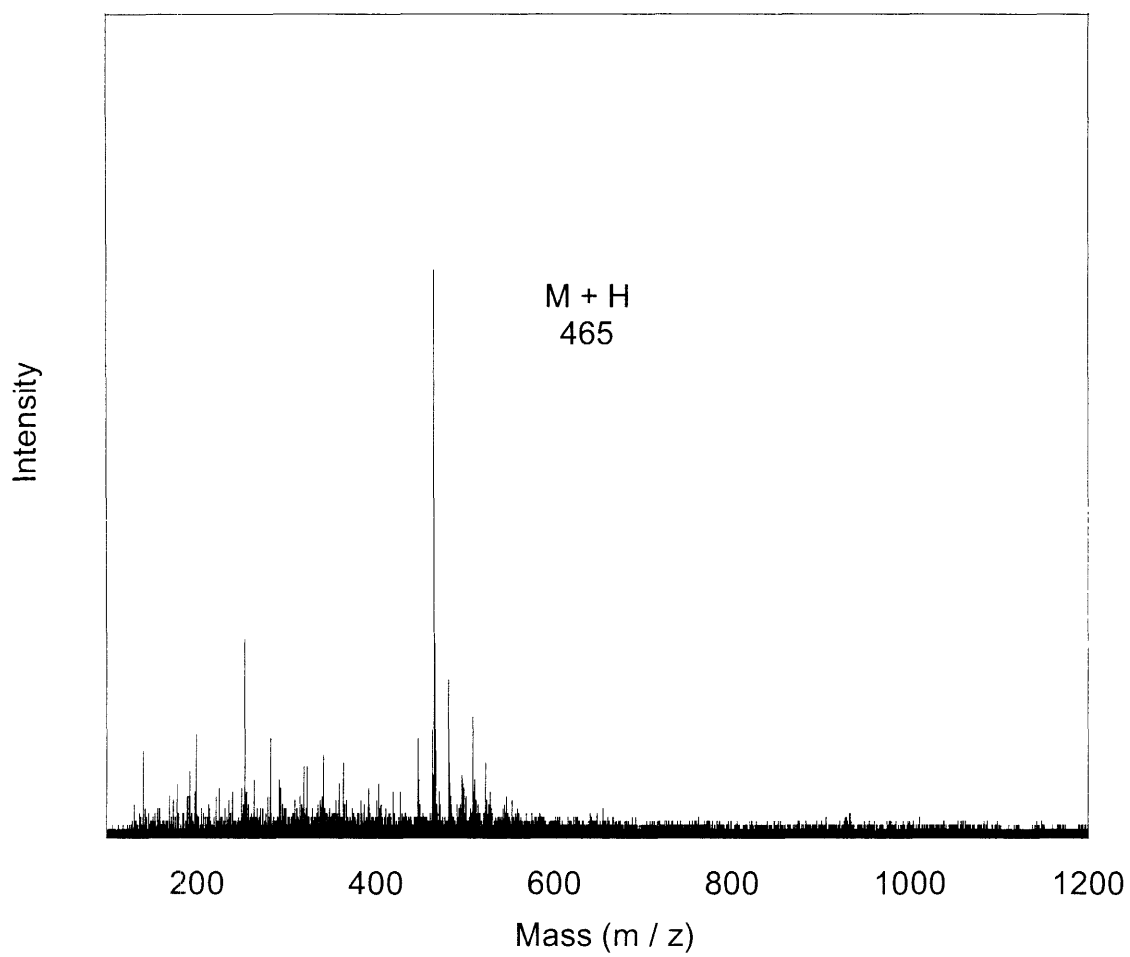


Figure A.1. Negative ion ES-MS of VB in 9:1 MeOH / H₂O

Appendix

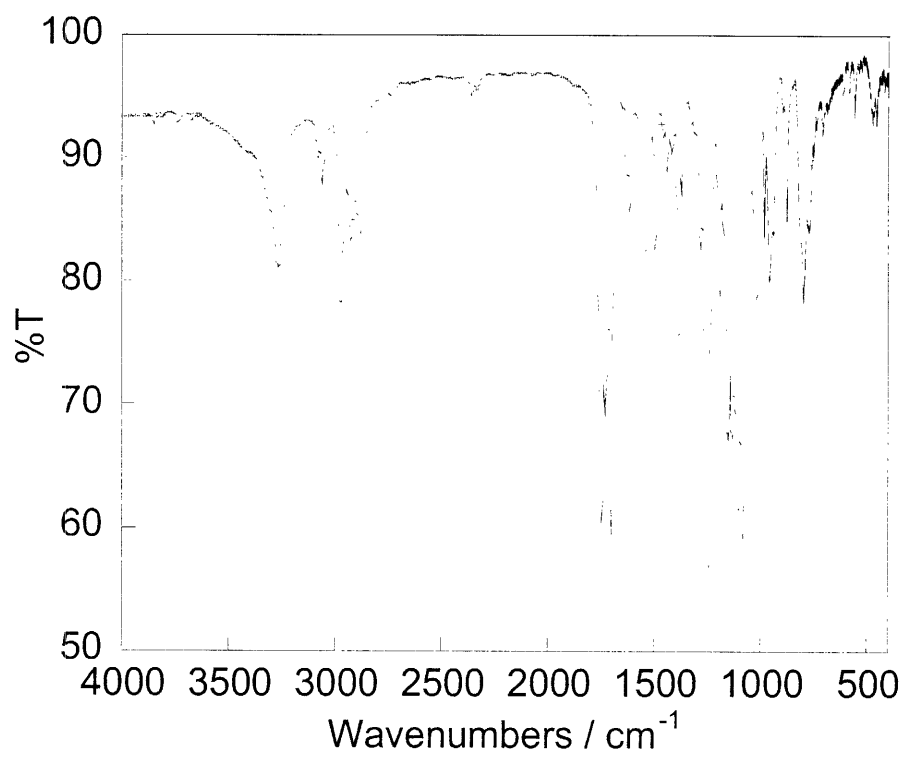


Figure A.2. FTIR spectrum of urethane coumarin linkage.

Appendix

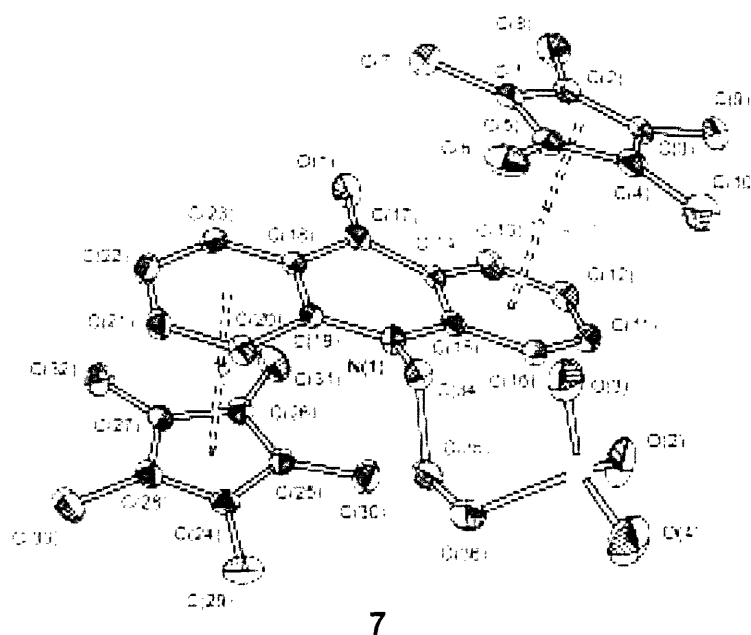
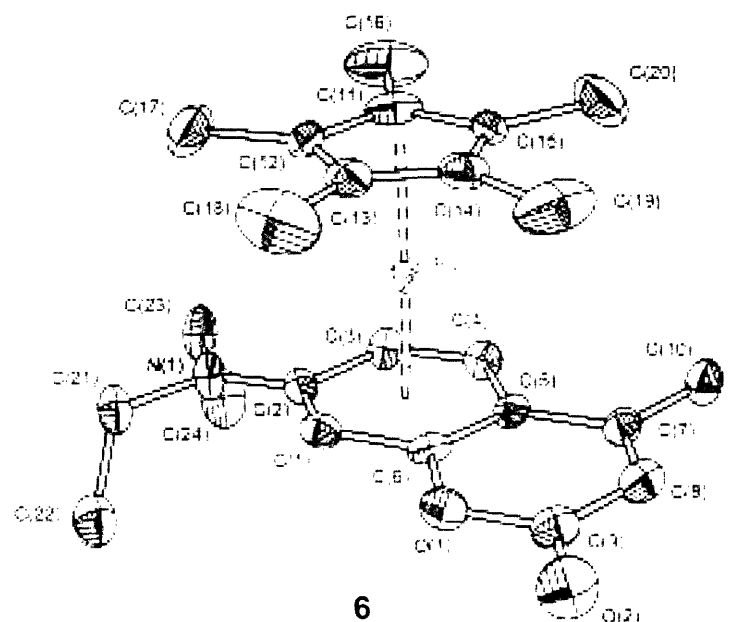


Figure A.3. Full labeling for thermal ellipsoid plots (50% ellipsoids) for $[\text{Cp}^*\text{Ru}(\text{C460})]^+$ (**6**- PF_6) and $[(\text{Cp}^*\text{Ru})_2(\text{PSA})]^+$ (**7**- PF_6) for tables of x-ray diffraction structural information.

Appendix

Table A.1. Crystal data and structure refinement parameters for [Cp*Ru(C460)]⁺ (**6-PF₆**), and [(Cp*Ru)₂(PSA)]⁺ (**7-PF₆**).

	6-PF₆	7-PF₆
Empirical formula	C ₂₄ H ₃₂ F ₆ N O ₂ P Ru	C ₄₀ H ₅₆ F ₆ N O ₆ P Ru ₂ S
Formula weight	612.55	1026.03
Crystal system	Monoclinic	Triclinic
Space group	<i>P2₁/n</i>	<i>P</i> $\bar{1}$
Unit cell dimensions	<i>a</i> = 9.0565(18) Å <i>b</i> = 19.892(4) Å <i>c</i> = 14.231(3) Å <i>β</i> = 93.9°	<i>a</i> = 11.1969(6) Å <i>b</i> = 12.0503(6) Å <i>c</i> = 16.7333(9) Å <i>α</i> = 72.1990(10)° <i>β</i> = 81.1420(10)° <i>γ</i> = 85.2830(10)°
Volume	2557.6(9) Å ³	2122.54(19) Å ³
Z	4	2
Density (calculated)	1.591 Mg/m ³	1.605 Mg/m ³
Absorption coefficient	0.741 mm ⁻¹	0.871 mm ⁻¹
F(000)	1248	1048
Crystal size (mm)	0.16 x 0.05 x 0.05	0.14 × 0.09 × 0.09
θ min for data collection	2.48°	2.39°
θ max for data collection	23.27°	23.28°
Index ranges	-10 ≤ <i>h</i> ≤ 7 -22 ≤ <i>k</i> ≤ 20 -15 ≤ <i>l</i> ≤ 15	-12 ≤ <i>h</i> ≤ 12 -13 ≤ <i>k</i> ≤ 13 -8 ≤ <i>l</i> ≤ 18
Reflections collected	10233	8614
Independent reflections	3668 [<i>R</i> _{int} = 0.0450]	5982 [<i>R</i> _{int} = 0.0161]
Absorption correction	Empirical SADABS	Empirical SADABS
Data / restraints / parameters	3668 / 0 / 324	5982 / 0 / 530
Goodness-of-fit on F ²	1.121	1.027
Final R indices [<i>I</i> > 2σ(<i>I</i>)]	<i>R</i> 1 = 0.0555 <i>wR</i> 2 = 0.1150	<i>R</i> 1 = 0.0306 <i>wR</i> 2 = 0.0706
R indices (all data)	<i>R</i> 1 = 0.0767 <i>wR</i> 2 = 0.1227	<i>R</i> 1 = 0.0370 <i>wR</i> 2 = 0.0735
Largest diff. peak	0.686 eÅ ⁻³	0.785 eÅ ⁻³
Largest diff. hole	-0.502 eÅ ⁻³	-0.561 eÅ ⁻³

Appendix

Table A.2. Atomic coordinates ($\times 10^4$) and equivalent isotropic displacement parameters ($\text{\AA}^2 \times 10^3$) for $[\text{Cp}^*\text{Ru}(\text{C460})]^+$ (**6-PF₆**). U(eq) is defined as one third of the trace of the orthogonalized U_{ij} tensor.

	x	y	z	U(eq)
Ru(1)	6815(1)	566(1)	2376(1)	33(1)
N(1)	8277(6)	1740(2)	947(4)	49(1)
O(1)	3677(4)	568(2)	1128(3)	48(1)
O(2)	1521(5)	67(3)	1185(4)	76(2)
C(1)	5936(7)	1150(3)	1131(4)	41(2)
C(2)	7499(7)	1171(3)	1044(4)	38(2)
C(3)	8236(7)	536(3)	1147(4)	43(2)
C(4)	7489(7)	-73(3)	1215(4)	41(2)
C(5)	5944(7)	-97(3)	1205(4)	36(1)
C(6)	5188(6)	517(3)	1153(4)	36(1)
C(7)	5035(7)	-711(3)	1307(4)	42(2)
C(8)	3587(7)	-639(4)	1300(4)	49(2)
C(9)	2810(8)	-13(4)	1217(5)	50(2)
C(10)	5841(7)	-1366(3)	1421(5)	53(2)
C(11)	8258(8)	559(5)	3644(5)	62(2)
C(12)	7462(10)	1185(4)	3580(5)	60(2)
C(13)	5973(10)	1027(4)	3604(4)	56(2)
C(14)	5777(8)	346(4)	3679(4)	52(2)
C(15)	7160(9)	44(3)	3707(4)	53(2)
C(16)	9906(10)	469(7)	3690(7)	124(4)
C(17)	8128(14)	1874(4)	3542(6)	114(4)
C(18)	4708(13)	1533(6)	3596(7)	124(5)
C(19)	4320(10)	-34(6)	3726(6)	110(4)
C(20)	7478(15)	-708(4)	3845(7)	116(4)
C(21)	7555(9)	2402(3)	896(5)	58(2)
C(22)	6890(9)	2570(4)	-58(6)	71(2)
C(23)	9886(8)	1725(4)	881(6)	66(2)
C(24)	10360(9)	1533(4)	-69(6)	84(3)
P(1)	8294(3)	1833(1)	6634(2)	72(1)
F(1)	6783(6)	1732(3)	6064(5)	134(2)
F(2)	8241(7)	1097(3)	7045(4)	113(2)
F(3)	9879(7)	1922(4)	7172(5)	136(2)
F(4)	8411(7)	2554(3)	6208(5)	132(2)
F(5)	9124(7)	1532(3)	5780(4)	113(2)
F(6)	7530(10)	2103(4)	7485(5)	169(3)

Appendix

Table A.3. Bond lengths (Å) and angles (°) for [Cp*Ru(C460)]⁺ (6-PF₆).

	(Å)		(°)
N(1)-C(2)	1.345(7)	C(2)-N(1)-C(23)	121.3(5)
N(1)-C(23)	1.467(9)	C(2)-N(1)-C(21)	121.6(5)
N(1)-C(21)	1.470(8)	C(23)-N(1)-C(21)	117.1(5)
O(1)-C(6)	1.370(7)	C(6)-O(1)-C(9)	119.9(5)
O(1)-C(9)	1.408(8)	C(2)-C(1)-C(6)	120.0(5)
O(2)-C(9)	1.175(8)	N(1)-C(2)-C(1)	124.2(6)
C(1)-C(2)	1.429(8)	N(1)-C(2)-C(3)	120.6(6)
C(1)-C(6)	1.431(8)	C(1)-C(2)-C(3)	115.0(5)
C(2)-C(3)	1.432(8)	C(4)-C(3)-C(2)	123.2(6)
C(3)-C(4)	1.393(8)	C(3)-C(4)-C(5)	121.3(6)
C(4)-C(5)	1.399(8)	C(6)-C(5)-C(4)	117.2(6)
C(5)-C(6)	1.399(8)	C(6)-C(5)-C(7)	116.8(5)
C(5)-C(7)	1.487(8)	C(4)-C(5)-C(7)	126.0(5)
C(7)-C(8)	1.319(9)	O(1)-C(6)-C(5)	123.4(6)
C(7)-C(10)	1.496(8)	O(1)-C(6)-C(1)	114.0(5)
C(8)-C(9)	1.430(9)	C(5)-C(6)-C(1)	122.5(5)
C(11)-C(15)	1.434(10)	C(8)-C(7)-C(5)	117.8(6)
C(11)-C(12)	1.439(10)	C(8)-C(7)-C(10)	125.1(6)
C(11)-C(16)	1.500(11)	C(5)-C(7)-C(10)	117.2(6)
C(12)-C(13)	1.388(10)	C(7)-C(8)-C(9)	125.4(7)
C(12)-C(17)	1.501(10)	O(2)-C(9)-O(1)	116.3(6)
C(13)-C(14)	1.371(10)	O(2)-C(9)-C(8)	127.1(7)
C(13)-C(18)	1.524(11)	O(1)-C(9)-C(8)	116.6(6)
C(14)-C(15)	1.388(10)	C(15)-C(11)-C(12)	106.0(6)
C(14)-C(19)	1.527(10)	C(15)-C(11)-C(16)	127.2(9)
C(15)-C(20)	1.534(10)	C(12)-C(11)-C(16)	126.8(9)
C(21)-C(22)	1.485(10)	C(13)-C(12)-C(11)	106.7(6)
C(23)-C(24)	1.496(10)	C(13)-C(12)-C(17)	127.0(9)
P(1)-F(6)	1.533(6)	C(11)-C(12)-C(17)	126.3(9)
P(1)-F(1)	1.555(6)	C(14)-C(13)-C(12)	110.9(7)
P(1)-F(4)	1.563(6)	C(14)-C(13)-C(18)	123.5(9)
P(1)-F(2)	1.579(5)	C(12)-C(13)-C(18)	125.6(8)
P(1)-F(3)	1.588(6)	C(13)-C(14)-C(15)	108.0(7)
P(1)-F(5)	1.589(5)	C(13)-C(14)-C(19)	127.6(8)
		C(15)-C(14)-C(19)	124.4(8)
		C(14)-C(15)-C(11)	108.5(6)

Appendix

C(14)-C(15)-C(20)	126.0(8)
C(11)-C(15)-C(20)	125.4(8)
N(1)-C(21)-C(22)	113.5(6)
N(1)-C(23)-C(24)	114.3(7)
F(6)-P(1)-F(1)	91.6(5)
F(6)-P(1)-F(4)	91.8(4)
F(1)-P(1)-F(4)	89.8(4)
F(6)-P(1)-F(2)	90.3(4)
F(1)-P(1)-F(2)	91.5(3)
F(4)-P(1)-F(2)	177.5(4)
F(6)-P(1)-F(3)	91.3(4)
F(1)-P(1)-F(3)	177.1(4)
F(4)-P(1)-F(3)	90.1(4)
F(2)-P(1)-F(3)	88.6(4)
F(6)-P(1)-F(5)	177.7(5)
F(1)-P(1)-F(5)	89.9(4)
F(4)-P(1)-F(5)	90.0(3)
F(2)-P(1)-F(5)	87.8(3)
F(3)-P(1)-F(5)	87.2(4)

Appendix

Table A.4. Anisotropic displacement parameters ($\text{\AA}^2 \times 10^3$) for $[\text{Cp}^*\text{Ru}(\text{C460})]_2^+$ (**6-PF₆**). The anisotropic displacement factor exponent takes the form: $-2\pi^2[h^2a^2 U_{11} + \dots + 2hkab U_{12}]$.

	U_{11}	U_{22}	U_{33}	U_{23}	U_{13}	U_{12}
Ru(1)	35(1)	32(1)	33(1)	-3(1)	1(1)	1(1)
N(1)	48(3)	30(3)	70(4)	3(3)	18(3)	0(3)
O(1)	37(2)	58(3)	51(3)	3(2)	2(2)	10(2)
O(2)	33(3)	88(4)	107(5)	7(3)	12(3)	3(3)
C(1)	43(4)	48(4)	32(4)	0(3)	4(3)	11(3)
C(2)	42(4)	35(4)	37(4)	0(3)	6(3)	0(3)
C(3)	40(3)	40(4)	51(4)	-5(3)	14(3)	-1(3)
C(4)	41(4)	43(4)	42(4)	-5(3)	10(3)	7(3)
C(5)	42(4)	36(3)	29(3)	-12(3)	2(3)	6(3)
C(6)	26(3)	57(4)	26(3)	-6(3)	0(2)	0(3)
C(7)	53(4)	40(4)	32(3)	-7(3)	5(3)	-2(3)
C(8)	45(4)	61(5)	42(4)	-6(3)	7(3)	-8(4)
C(9)	42(4)	61(5)	46(4)	-4(3)	2(3)	-2(4)
C(10)	46(4)	44(4)	68(5)	-3(4)	2(4)	-7(3)
C(11)	48(4)	97(6)	40(4)	-5(4)	-12(3)	1(5)
C(12)	103(7)	42(4)	32(4)	-3(3)	-10(4)	-25(4)
C(13)	91(6)	50(5)	27(4)	-10(3)	2(4)	18(4)
C(14)	59(5)	68(5)	29(4)	2(3)	3(3)	-3(4)
C(15)	94(6)	32(4)	31(4)	3(3)	-12(4)	0(4)
C(16)	62(6)	223(14)	85(7)	6(8)	-19(5)	8(7)
C(17)	206(12)	71(6)	63(6)	-4(5)	-10(7)	-66(7)
C(18)	165(11)	135(9)	73(6)	-18(6)	20(7)	93(9)
C(19)	87(7)	193(12)	51(5)	-4(6)	16(5)	-66(7)
C(20)	219(14)	58(6)	68(6)	14(5)	-14(7)	25(7)
C(21)	72(5)	34(4)	70(5)	0(4)	10(4)	3(4)
C(22)	83(6)	55(5)	75(6)	-1(4)	13(5)	6(4)
C(23)	56(5)	41(4)	103(6)	0(4)	25(5)	-13(4)
C(24)	74(6)	75(6)	109(7)	3(5)	44(5)	5(5)
P(1)	71(2)	69(1)	80(2)	-1(1)	26(1)	-19(1)
F(1)	88(4)	87(4)	220(7)	-19(4)	-24(4)	-9(3)
F(2)	134(5)	86(4)	124(5)	21(3)	51(4)	-12(4)
F(3)	106(5)	171(6)	131(5)	-14(5)	-3(4)	-46(4)
F(4)	135(5)	62(3)	203(7)	25(4)	44(5)	-16(3)
F(5)	133(5)	128(5)	84(4)	6(3)	39(4)	31(4)
F(6)	215(7)	137(6)	171(7)	-50(5)	129(6)	-37(6)

Appendix

Table A.5. Hydrogen coordinates ($\times 10^4$) and isotropic displacement parameters ($\text{\AA}^2 \times 10^3$) for $[\text{Cp}^*\text{Ru}(\text{C460})]^+$ (**6-PF₆**).

	x	y	z	U(eq)
H(1)	5394	1556	1174	49
H(3)	9287	529	1169	51
H(4)	8039	-479	1270	50
H(8)	3012	-1034	1354	59
H(10A)	5149	-1718	1586	79
H(10B)	6633	-1324	1923	79
H(10C)	6270	-1483	829	79
H(16A)	10143	32	3421	186
H(16B)	10302	489	4348	186
H(16C)	10350	827	3330	186
H(17A)	7412	2182	3224	171
H(17B)	9023	1856	3193	171
H(17C)	8385	2034	4184	171
H(18A)	4382	1582	4235	186
H(18B)	3880	1374	3175	186
H(18C)	5049	1969	3374	186
H(19A)	4384	-465	3397	165
H(19B)	3511	233	3424	165
H(19C)	4130	-115	4386	165
H(20A)	7575	-811	4520	174
H(20B)	8400	-823	3561	174
H(20C)	6661	-970	3543	174
H(21A)	8295	2750	1092	70
H(21B)	6771	2412	1347	70
H(22A)	7658	2560	-510	106
H(22B)	6452	3020	-50	106
H(22C)	6119	2241	-245	106
H(23A)	10321	1401	1352	79
H(23B)	10291	2175	1047	79
H(24A)	9981	1085	-236	126
H(24B)	11444	1530	-55	126
H(24C)	9968	1860	-538	126

Appendix

Table A.6. Atomic coordinates ($\times 10^4$) and equivalent isotropic displacement parameters ($\text{\AA}^2 \times 10^3$) for $[(\text{Cp}^*\text{Ru})_2(\text{PSA})]^+$ (**7-PF₆**). U(eq) is defined as one third of the trace of the orthogonalized U_{ij} tensor.

	x	y	z	U(eq)
C(2S)	5029(6)	8104(6)	5795(4)	105(2)
Ru(1)	250(1)	9998(1)	2635(1)	23(1)
Ru(2)	4504(1)	6864(1)	2098(1)	23(1)
S(1)	-96(1)	6516(1)	5859(1)	36(1)
N(1)	1919(2)	7508(2)	3199(2)	24(1)
O(1)	2610(2)	9654(2)	759(2)	40(1)
O(2)	196(3)	7729(2)	5628(2)	51(1)
O(3)	-975(2)	6313(3)	5367(2)	49(1)
O(4)	-445(3)	5994(3)	6763(2)	61(1)
C(1)	-940(3)	9570(3)	1857(2)	28(1)
C(2)	-1017(3)	10798(3)	1726(2)	30(1)
C(3)	-1457(3)	10999(3)	2519(2)	30(1)
C(4)	-1648(3)	9884(3)	3145(2)	31(1)
C(5)	-1330(3)	9002(3)	2733(2)	28(1)
C(6)	-1443(4)	7713(3)	3126(3)	41(1)
C(7)	-561(4)	8987(4)	1180(3)	41(1)
C(8)	-745(4)	11717(4)	891(2)	44(1)
C(9)	-1738(4)	12161(3)	2667(3)	43(1)
C(10)	-2125(4)	9694(4)	4063(3)	47(1)
C(11)	1231(3)	10417(3)	3551(2)	31(1)
C(12)	1615(3)	11176(3)	2746(3)	33(1)
C(13)	2048(3)	10715(3)	2075(2)	31(1)
C(14)	2138(3)	9484(3)	2220(2)	24(1)
C(15)	1808(3)	8707(3)	3048(2)	24(1)
C(16)	1300(3)	9202(3)	3708(2)	27(1)
C(17)	2514(3)	9030(3)	1487(2)	28(1)
C(18)	2781(3)	7762(3)	1712(2)	25(1)
C(19)	2499(3)	7040(3)	2565(2)	23(1)
C(20)	2885(3)	5841(3)	2769(2)	27(1)
C(21)	3450(3)	5368(3)	2127(2)	31(1)
C(22)	3681(3)	6075(3)	1277(2)	33(1)
C(23)	3356(3)	7263(3)	1074(2)	31(1)
C(24)	5758(3)	6594(3)	3022(2)	28(1)
C(25)	5490(3)	7811(3)	2688(2)	28(1)
C(26)	5900(3)	8148(3)	1793(2)	28(1)

Appendix

C(27)	6417(3)	7132(3)	1584(2)	29(1)
C(28)	6326(3)	6172(3)	2344(2)	30(1)
C(29)	5547(4)	5889(4)	3940(2)	43(1)
C(30)	4970(4)	8613(4)	3196(3)	43(1)
C(31)	5835(4)	9360(3)	1194(3)	45(1)
C(32)	7016(4)	7086(4)	725(3)	44(1)
C(33)	6853(4)	4968(3)	2410(3)	44(1)
C(34)	1293(3)	6732(3)	3990(2)	25(1)
C(35)	2002(3)	6427(3)	4740(2)	31(1)
C(36)	1266(3)	5761(3)	5569(2)	36(1)
P(1)	5029(1)	2601(1)	1384(1)	34(1)
F(1)	4767(4)	1438(2)	2120(2)	93(1)
F(2)	4696(3)	1975(2)	746(2)	72(1)
F(3)	6362(3)	2177(4)	1214(3)	111(2)
F(4)	5355(2)	3215(2)	2033(2)	65(1)
F(5)	3651(2)	2997(3)	1579(2)	83(1)
F(6)	5192(5)	3767(3)	661(2)	123(2)
O(1S)	6569(3)	6784(4)	5461(3)	94(1)
O(2S)	122(5)	5897(3)	1844(3)	101(2)
C(1S)	6208(5)	7535(6)	5958(3)	84(2)
C(4S)	1058(7)	4679(6)	989(5)	102(2)
C(3S)	318(7)	5611(7)	1131(4)	109(3)

Appendix

Table A.7. Bond lengths (Å) and angles (°) for [(Cp*Ru)₂(PSA)]⁺ (7-PF₆).

	(Å)		(°)
C(2S)-C(1S)	1.461(8)	O(2)-S(1)-O(4)	113.79(18)
S(1)-O(2)	1.444(3)	O(2)-S(1)-O(3)	112.60(19)
S(1)-O(4)	1.454(3)	O(4)-S(1)-O(3)	111.7(2)
S(1)-O(3)	1.455(3)	O(2)-S(1)-C(36)	105.93(18)
S(1)-C(36)	1.790(4)	O(4)-S(1)-C(36)	106.73(18)
N(1)-C(15)	1.388(4)	O(3)-S(1)-C(36)	105.36(18)
N(1)-C(19)	1.398(4)	C(15)-N(1)-C(19)	120.2(3)
N(1)-C(34)	1.478(4)	C(15)-N(1)-C(34)	119.6(3)
O(1)-C(17)	1.214(4)	C(19)-N(1)-C(34)	119.8(3)
C(1)-C(2)	1.425(5)	C(2)-C(1)-C(5)	108.3(3)
C(1)-C(5)	1.432(5)	C(2)-C(1)-C(7)	125.4(3)
C(1)-C(7)	1.499(5)	C(5)-C(1)-C(7)	126.3(3)
C(2)-C(3)	1.428(5)	C(1)-C(2)-C(3)	108.1(3)
C(2)-C(8)	1.500(5)	C(1)-C(2)-C(8)	125.7(3)
C(3)-C(4)	1.437(5)	C(3)-C(2)-C(8)	126.0(3)
C(3)-C(9)	1.496(5)	C(2)-C(3)-C(4)	107.8(3)
C(4)-C(5)	1.429(5)	C(2)-C(3)-C(9)	126.3(3)
C(4)-C(10)	1.501(5)	C(4)-C(3)-C(9)	125.8(3)
C(5)-C(6)	1.497(5)	C(5)-C(4)-C(3)	108.0(3)
C(11)-C(12)	1.403(5)	C(5)-C(4)-C(10)	126.5(4)
C(11)-C(16)	1.404(5)	C(3)-C(4)-C(10)	125.5(4)
C(12)-C(13)	1.404(5)	C(4)-C(5)-C(1)	107.8(3)
C(13)-C(14)	1.426(5)	C(4)-C(5)-C(6)	126.8(3)
C(14)-C(15)	1.428(5)	C(1)-C(5)-C(6)	125.3(3)
C(14)-C(17)	1.482(5)	C(12)-C(11)-C(16)	121.5(3)
C(15)-C(16)	1.433(5)	C(11)-C(12)-C(13)	119.5(3)
C(17)-C(18)	1.474(5)	C(12)-C(13)-C(14)	120.2(3)
C(18)-C(23)	1.426(5)	C(13)-C(14)-C(15)	120.5(3)
C(18)-C(19)	1.430(5)	C(13)-C(14)-C(17)	118.7(3)
C(19)-C(20)	1.426(5)	C(15)-C(14)-C(17)	120.7(3)
C(20)-C(21)	1.409(5)	N(1)-C(15)-C(14)	120.9(3)
C(21)-C(22)	1.414(5)	N(1)-C(15)-C(16)	121.0(3)
C(22)-C(23)	1.397(5)	C(14)-C(15)-C(16)	118.0(3)
C(24)-C(25)	1.425(5)	C(11)-C(16)-C(15)	120.1(3)
C(24)-C(28)	1.425(5)	O(1)-C(17)-C(18)	122.6(3)
C(24)-C(29)	1.502(5)	O(1)-C(17)-C(14)	122.7(3)

Appendix

C(25)-C(26)	1.437(5)	C(28)-C(24)-C(29)	125.6(3)
C(25)-C(30)	1.501(5)	C(24)-C(25)-C(26)	107.9(3)
C(26)-C(27)	1.429(5)	C(24)-C(25)-C(30)	125.7(4)
C(26)-C(31)	1.501(5)	C(26)-C(25)-C(30)	126.2(3)
C(27)-C(28)	1.430(5)	C(27)-C(26)-C(25)	107.7(3)
C(27)-C(32)	1.503(5)	C(27)-C(26)-C(31)	126.3(3)
C(28)-C(33)	1.499(5)	C(25)-C(26)-C(31)	126.0(3)
C(34)-C(35)	1.523(5)	C(26)-C(27)-C(28)	108.0(3)
C(35)-C(36)	1.524(5)	C(26)-C(27)-C(32)	126.2(3)
P(1)-F(3)	1.550(3)	C(28)-C(27)-C(32)	125.7(3)
P(1)-F(6)	1.551(3)	C(24)-C(28)-C(27)	108.1(3)
P(1)-F(1)	1.571(3)	C(24)-C(28)-C(33)	126.8(4)
P(1)-F(2)	1.584(3)	C(27)-C(28)-C(33)	124.9(3)
P(1)-F(4)	1.587(3)	N(1)-C(34)-C(35)	114.3(3)
P(1)-F(5)	1.592(3)	C(34)-C(35)-C(36)	112.8(3)
O(1S)-C(1S)	1.404(7)	C(35)-C(36)-S(1)	114.2(3)
O(2S)-C(3S)	1.323(7)	F(3)-P(1)-F(6)	93.7(3)
C(4S)-C(3S)	1.398(8)	F(3)-P(1)-F(1)	90.2(2)
		F(6)-P(1)-F(1)	176.1(3)
	(°)	F(3)-P(1)-F(2)	88.61(17)
C(18)-C(17)-C(14)	114.7(3)	F(6)-P(1)-F(2)	90.8(2)
C(23)-C(18)-C(19)	120.0(3)	F(1)-P(1)-F(2)	88.54(17)
C(23)-C(18)-C(17)	119.4(3)	F(3)-P(1)-F(4)	91.54(17)
C(19)-C(18)-C(17)	120.6(3)	F(6)-P(1)-F(4)	90.0(2)
N(1)-C(19)-C(20)	120.5(3)	F(1)-P(1)-F(4)	90.73(17)
N(1)-C(19)-C(18)	121.0(3)	F(2)-P(1)-F(4)	179.25(19)
C(20)-C(19)-C(18)	118.5(3)	F(3)-P(1)-F(5)	178.2(2)
C(21)-C(20)-C(19)	120.3(3)	F(6)-P(1)-F(5)	88.1(2)
C(20)-C(21)-C(22)	120.9(3)	F(1)-P(1)-F(5)	88.0(2)
C(23)-C(22)-C(21)	119.4(3)	F(2)-P(1)-F(5)	91.09(16)
C(22)-C(23)-C(18)	120.7(3)	F(4)-P(1)-F(5)	88.74(15)
C(25)-C(24)-C(28)	108.2(3)	O(1S)-C(1S)-C(2S)	111.5(6)
C(25)-C(24)-C(29)	126.0(3)	O(2S)-C(3S)-C(4S)	125.9(5)

Appendix

Table A.8. Anisotropic displacement parameters ($\text{\AA}^2 \times 10^3$) for $[(\text{Cp}^*\text{Ru})_2(\text{PSA})]^+(\text{7-PF}_6)$. The anisotropic displacement factor exponent takes the form: $-2\pi^2[h^2a^2U_{11} + \dots + 2hkabU_{12}]$.

	U_{11}	U_{22}	U_{33}	U_{23}	U_{13}	U_{12}
C(2S)	88(5)	119(6)	75(4)	1(4)	8(4)	33(4)
Ru(1)	21(1)	21(1)	26(1)	-8(1)	-1(1)	1(1)
Ru(2)	21(1)	24(1)	25(1)	-11(1)	-4(1)	3(1)
S(1)	46(1)	37(1)	24(1)	-11(1)	3(1)	1(1)
N(1)	24(2)	24(2)	24(2)	-9(1)	0(1)	1(1)
O(1)	45(2)	37(2)	25(2)	0(1)	5(1)	7(1)
O(2)	72(2)	38(2)	43(2)	-21(1)	11(2)	0(2)
O(3)	39(2)	65(2)	48(2)	-28(2)	-1(1)	4(1)
O(4)	77(2)	63(2)	29(2)	-7(2)	10(2)	3(2)
C(1)	21(2)	33(2)	34(2)	-12(2)	-10(2)	4(2)
C(2)	25(2)	36(2)	29(2)	-10(2)	-9(2)	6(2)
C(3)	20(2)	36(2)	35(2)	-12(2)	-7(2)	10(2)
C(4)	18(2)	43(2)	30(2)	-9(2)	-3(2)	2(2)
C(5)	20(2)	32(2)	34(2)	-10(2)	-8(2)	-2(2)
C(6)	34(2)	38(2)	52(3)	-5(2)	-17(2)	-8(2)
C(7)	43(2)	46(2)	40(2)	-22(2)	-10(2)	3(2)
C(8)	48(3)	42(2)	34(2)	-2(2)	-7(2)	7(2)
C(9)	41(2)	43(2)	49(3)	-23(2)	-11(2)	17(2)
C(10)	33(2)	67(3)	35(2)	-10(2)	5(2)	-3(2)
C(11)	29(2)	30(2)	40(2)	-19(2)	-9(2)	0(2)
C(12)	29(2)	24(2)	50(3)	-14(2)	-9(2)	-3(2)
C(13)	21(2)	26(2)	40(2)	-5(2)	0(2)	-3(2)
C(14)	17(2)	26(2)	30(2)	-8(2)	-4(2)	4(1)
C(15)	17(2)	26(2)	28(2)	-8(2)	-4(1)	2(1)
C(16)	25(2)	32(2)	28(2)	-15(2)	-5(2)	3(2)
C(17)	21(2)	31(2)	28(2)	-6(2)	-2(2)	3(2)
C(18)	19(2)	30(2)	26(2)	-11(2)	-5(2)	2(1)
C(19)	17(2)	28(2)	26(2)	-12(2)	-5(1)	2(1)
C(20)	24(2)	23(2)	34(2)	-9(2)	-3(2)	-1(2)
C(21)	27(2)	27(2)	46(2)	-20(2)	-9(2)	3(2)
C(22)	27(2)	41(2)	40(2)	-26(2)	-5(2)	2(2)
C(23)	26(2)	44(2)	25(2)	-14(2)	-7(2)	3(2)
C(24)	24(2)	34(2)	29(2)	-9(2)	-9(2)	-1(2)
C(25)	22(2)	33(2)	37(2)	-19(2)	-6(2)	-1(2)
C(26)	21(2)	31(2)	34(2)	-11(2)	-3(2)	-2(2)

Appendix

C(27)	20(2)	37(2)	34(2)	-14(2)	-6(2)	2(2)
C(28)	19(2)	31(2)	42(2)	-14(2)	-10(2)	2(2)
C(29)	39(2)	55(3)	33(2)	-5(2)	-13(2)	-6(2)
C(30)	37(2)	53(3)	52(3)	-33(2)	-8(2)	2(2)
C(31)	40(2)	30(2)	55(3)	-3(2)	-2(2)	-2(2)
C(32)	32(2)	62(3)	42(2)	-24(2)	1(2)	6(2)
C(33)	37(2)	33(2)	64(3)	-16(2)	-16(2)	8(2)
C(34)	25(2)	24(2)	23(2)	-4(2)	1(2)	-3(1)
C(35)	29(2)	33(2)	29(2)	-5(2)	-7(2)	5(2)
C(36)	41(2)	33(2)	29(2)	-3(2)	-8(2)	4(2)
P(1)	38(1)	30(1)	35(1)	-14(1)	-2(1)	1(1)
F(1)	175(4)	42(2)	52(2)	-8(1)	3(2)	-2(2)
F(2)	99(2)	67(2)	73(2)	-46(2)	-41(2)	24(2)
F(3)	39(2)	152(3)	193(4)	-132(3)	-10(2)	20(2)
F(4)	58(2)	72(2)	92(2)	-60(2)	-22(2)	7(1)
F(5)	45(2)	86(2)	141(3)	-72(2)	-14(2)	11(2)
F(6)	235(5)	46(2)	63(2)	1(2)	27(3)	-17(2)
O(1S)	51(2)	138(4)	124(4)	-86(3)	-10(2)	0(2)
O(2S)	159(5)	58(2)	79(3)	-14(2)	-24(3)	30(3)
C(1S)	77(4)	116(5)	42(3)	-16(3)	9(3)	21(4)
C(4S)	116(6)	104(5)	116(6)	-65(5)	-49(5)	18(4)
C(3S)	110(5)	142(6)	47(4)	-5(4)	-17(3)	65(5)

Appendix

Table A.9. Hydrogen coordinates ($\times 10^4$) and isotropic displacement parameters ($\text{\AA}^2 \times 10^3$) for $[(\text{Cp}^*\text{Ru})_2(\text{PSA})]^+ (\text{7-PF}_6)$.

	x	y	z	U(eq)
H(2S1)	5097	8641	5218	157
H(2S2)	4755	8540	6201	157
H(2S3)	4443	7512	5856	157
H(6A)	-1472	7520	3741	62
H(6B)	-744	7305	2897	62
H(6C)	-2186	7471	2995	62
H(7A)	-366	8160	1442	61
H(7B)	153	9360	810	61
H(7C)	-1223	9059	844	61
H(8A)	-1438	11831	577	65
H(8B)	-29	11468	562	65
H(8C)	-591	12451	988	65
H(9A)	-1197	12738	2265	64
H(9B)	-1622	12105	3247	64
H(9C)	-2579	12403	2586	64
H(10A)	-3009	9672	4141	71
H(10B)	-1887	10332	4246	71
H(10C)	-1791	8952	4401	71
H(11)	917	10733	3999	37
H(12)	1582	11995	2655	40
H(13)	2282	11225	1524	37
H(16)	1009	8707	4254	33
H(20)	2761	5359	3340	32
H(21)	3679	4562	2267	37
H(22)	4054	5746	847	40
H(23)	3520	7743	504	37
H(29A)	5330	5098	3984	65
H(29B)	4888	6258	4238	65
H(29C)	6287	5849	4195	65
H(30A)	5597	8781	3486	65
H(30B)	4298	8239	3615	65
H(30C)	4673	9342	2817	65
H(31A)	6509	9801	1235	67
H(31B)	5067	9750	1343	67
H(31C)	5885	9320	614	67
H(32A)	6729	7757	288	66

Appendix

H(32B)	6813	6363	633	66
H(32C)	7894	7109	696	66
H(33A)	7708	4936	2484	66
H(33B)	6782	4774	1892	66
H(33C)	6414	4406	2898	66
H(34A)	1117	6001	3885	30
H(34B)	509	7113	4140	30
H(35A)	2271	7155	4802	37
H(35B)	2733	5949	4625	37
H(36A)	1776	5592	6028	43
H(36B)	1055	5005	5519	43
H(1S)	7311	6614	5465	141
H(2S)	259	5311	2250	152
H(1S1)	6818	8137	5833	100
H(1S2)	6167	7085	6565	100
H(4S1)	1565	4381	1443	153
H(4S2)	1575	4946	443	153
H(4S3)	553	4057	980	153
H(3S1)	628	6316	686	130
H(3S2)	-489	5494	1005	130

Aetna W. Wun

77 Massachusetts Ave. (2-209) · Cambridge, MA 02139
aetna@mit.edu · W/617.258.8120

Education

- 2000-2005* **MASSACHUSETTS INSTITUTE OF TECHNOLOGY** Cambridge, MA
Ph.D. Candidate in Inorganic Chemistry (Spring 2005)
Thesis: "Synthesis, Design and Characterization of a Distributed Feedback Grating Based Non-Linear Optical Chemosensor"
Graduate Research Assistant · Professor Daniel G. Nocera, Advisor
Initiated research project to develop nanoscale chemical sensors using non-linear optical technology. Independently responsible for thin film and device design, fabrication, characterization and testing.
- Synthesized and characterized inorganic compounds and organic dye molecules for impregnation into SiO₂ / TiO₂ thin film matrices.
 - Fabricated and patterned distributed feedback (DFB) thin film laser devices, and obtained highly non-linear laser emission.
 - Maintained and utilized instrumentation for both steady state and electronic spectroscopy and laser fluorescence measurements, including cryostat operation.
 - Prepared research grants and proposals for external funding agencies (e.g., National Science Foundation (NSF), Air Force Office of Scientific Research (AFOSR) and Defense Advanced Research Projects Agency (DARPA)).
- 1996-2000* **UNIVERSITY OF CALIFORNIA, SAN DIEGO** La Jolla, CA
B.S. Chemistry · Minor in Economics · Provost's List
Undergraduate Research Assistant · Professor Michael J. Sailor, Advisor
Investigated physical properties and examined stability of derivatized porous silicon surfaces for chemical and biological sensor applications.
- Developed an electrochemical method for facile organic modification of porous silicon.
 - Analyzed surface coverage and determined composition of functionalized silicon surfaces.
 - Collaborated with École Polytechnique (Palaiseau, France) and Defense Evaluation Research Agency (Malvern, England) to stabilize porous silicon surfaces, determine its surface composition, and to study the effects of etching on the surface morphology.

Teaching Experience

- 2000-2001* **MASSACHUSETTS INSTITUTE OF TECHNOLOGY** Cambridge, MA
Teaching Assistant
Lecture courses: Principles of Chemical Science, Inorganic Chemistry
- 1998-2000* **UNIVERSITY OF CALIFORNIA, SAN DIEGO** La Jolla, CA
Teaching Assistant
Lecture courses: General Chemistry A-C

Awards and Affiliations

- 1996-2000* University of California Regents Scholar (full tuition)
2000 I.M. Kolthoff Award in Analytical Chemistry, Honorable Mention, American Chemical Society
1996 Silicon Graphics/Cray Undergraduate Research Fellowship
1996-1997 Hewlett-Packard Undergraduate Scholarship
1997-present American Chemical Society member

Aetna W. Wun

Publications and Presentations

- Wun, A. W.; Snee, P.; Chan, Y.; Bawendi, M. G.; Nocera, D. G. *J. Mater. Chem.* **2005**, DOI: 10.1039/b503026a
- Wun, A. W.; Nocera, D. G. Synthesis, Design and Characterization of a Non-linear Optical Chemosensor. Abstract of Papers, 229th ACS National Meeting, San Diego, CA; March 2005.
- Walker, G. W.; Sundar, V. C.; Rudzinski, C. M.; Wun, A. W.; Bawendi, M. G.; Nocera, D. G. "Quantum-dot optical temperature probes." *Appl. Phys. Lett.* 2003, 83, 3555-3557.
- Canaria, C. A.; Lees, I. N.; Wun, A. W.; Miskelly, G. M.; Sailor, M. J. "Characterization of the carbon-silicon stretch in methylated porous silicon-observation of an anomalous isotope shift in the FTIR spectrum." *Inorg. Chem. Comm.* 2002, 5, 560-564.
- Tinsley-Bown, A. M.; Canham, L. T.; Hollings, M.; Anderson, M. H.; Reeves, C. L.; Cox, T. I.; Nicklin, S.; Squirrell, D. J.; Perkins, E.; Hutchinson, A.; Sailor, M. J.; Wun, A. "Tuning the pore size and surface chemistry of porous silicon for immunoassays." *Phys. Status Solidi A* 2000, 182, 547-553.
- Gurtner, C.; Wun, A. W.; Sailor, M. J. "Surface modification of porous silicon by electrochemical reduction of organo halides." *Angew. Chem. Int. Ed.* 1999, 38, 1966.
- Poster: "Electrochemical derivatization and stabilization of porous silicon surfaces with alkylhalides" American Chemical Society National Meeting, April 2000, San Francisco.
- Invited talk: "Electrochemical modification of porous silicon with alkylhalides", *Porous Semiconductors Science and Technology International Conference*, March 2000, Spain.
- Poster: "The chemical derivatization of porous silicon with methyl lithium." *Porous Semiconductors Science and Technology International Conference*, March 1998, Spain.

Skills

NMR, SEM, AFM, UV-Vis, FTIR, HPLC, spectroscopic ellipsometry, surface profilometry, fluorescence spectroscopy, mass spectrometry, glove box and Schlenk techniques.

References

Prof. Daniel G. Nocera
MIT Dept. of Chemistry
77 Massachusetts Ave. (6-333)
Cambridge, MA 02139
nocera@mit.edu / 617.253.5537

Prof. Michael J. Sailor
UC San Diego
9500 Gilman Dr. (m/c 0358)
La Jolla, CA 92093-0358
msailor@ucsd.edu / 858.534.8188

Prof. Stephen J. Lippard
MIT Dept. of Chemistry
77 Massachusetts Ave. (18-498)
Cambridge, MA 02139
lippard@mit.edu / 617.253.1892